

# **CARBON NANOTUBES AS REINFORCEMENTS AND INTERFACE MODIFIERS IN METAL MATRIX COMPOSITES**

THÈSE N° 3140 (2004)

PRÉSENTÉE À LA FACULTÉ SCIENCES DE BASE

Institut de physique de la matière complexe

SECTION DE PHYSIQUE

ÉCOLE POLYTECHNIQUE FÉDÉRALE DE LAUSANNE

POUR L'OBTENTION DU GRADE DE DOCTEUR ÈS SCIENCES

PAR

**Jian YANG**

B.Sc. in Physics, Guangxi Normal University, Chine  
et de nationalité chinoise

acceptée sur proposition du jury:

Dr R. Schaller, directeur de thèse  
Prof. W. Benoit, rapporteur  
Prof. E. Carreño-Morelli, rapporteur  
Prof. C. Félix, rapporteur  
Prof. L. Forró, rapporteur  
Prof. J. San Juan, rapporteur

Lausanne, EPFL  
2005



*To my parents*



# Abstract

Multi-wall carbon nanotubes (MWCNTs), catalytically grown by chemical vapour deposition (CVD), have been successfully employed in the development of bulk composites, where aluminium alloys (Al-4%Cu-1%Mg-0.5%Ag, called WFA) or commercial pure magnesium have been used as matrix, while MWCNTs served as interface modifiers and/or reinforcing phase. Four different composites, WFA or Mg reinforced with 25% volume fraction of Al<sub>2</sub>O<sub>3</sub> SAFFIL fibres coated or not with MWCNTs were processed by low pressure infiltration. Two other composites, made of pure Mg reinforced with 1% and 2% weight fraction of MWCNTs, were fabricated by powder metallurgy.

Scanning Electron Microscope (SEM) revealed fine microstructures of the produced specimens: locally homogeneous distribution of carbon nanotubes (CNTs) in 1% and 2% of CNTs reinforced Mg composites, and overall uniform dispersion of SAFFIL fibres in WFA-25%SAFFIL-CNTs and Mg-25%SAFFIL-CNTs. However, CNTs are not visible in WFA-25%SAFFIL-CNTs and Mg-25%SAFFIL-CNTs in this scale. It could be assumed that together with SAFFIL fibres, they are embedded completely in the matrix. A substantial increase in Young's modulus has been attributed to the addition of CNTs as well as the effective interface bonding between CNTs and matrix.

Elastic and anelastic properties of the specimens of the six composites have been investigated by mechanical spectroscopy. Mechanical loss and shear modulus were characterized as a function of temperature. The obtained experimental results have demonstrated positive impacts of MWCNTs on the elastic and anelastic properties of these composites, by comparing to the corresponding MWCNTs-free materials, respectively, and the advantages of using CNTs as reinforcements in metal matrix composites (MMCs).

A significant increase in transient damping due to CNTs has been measured in WFA-25%SAFFIL-CNTs and Mg-25%SAFFIL-CNTs. It indicates that a SAFFIL-matrix interface softening has been achieved. This has been interpreted by theoretical modelling as due to an additional density of mobile dislocations nucleated by CNT tips in the interface between SAFFIL fibres and matrix. On the other hand, the CNTs far away from the SAFFIL-matrix interface are assumed to pin dislocation loops, leading to a decrease in their mobility. Dislocation motion controlled by solid friction has been identified as the relaxation mechanism of thermal stresses.

Damping in Mg-2%CNTs remains approximately as high as in pure Mg. Mechanical loss spectrum obtained in both Mg-1%CNTs and Mg-2%CNTs is composed of a relaxation peak superposed on an exponential background. The activation enthalpy of the peak is of 0.83 eV and the limit relaxation time of  $2.3 \times 10^{-11}$  s. The peak is explained by a dislocation dragging model.

An enhancement in the shear modulus has been measured in WFA-25%SAFFIL-CNTs, Mg-25%SAFFIL-CNTs and Mg-2%CNTs due to the addition of CNTs. Hot Isostatic Pressing (HIP), which was used in processing Mg-2%CNTs, was found to be advantageous in obtaining a CNTs - Mg composite with better interface bonding.

# Résumé

Des nanotubes de carbone à multi-parois (MWCNTs), fabriqués par déposition en phase vapeur sur un substrat (CVD), ont été utilisés avec succès dans le développement de matériaux composites à matrices métalliques (MMCs) massifs. Les matrices étaient soit un alliage d'aluminium (Al-4%Cu-1%Mg-0.5%Ag, désigné WFA), soit du magnésium de pureté industrielle. Les nanotubes MWCNTs ont été utilisés comme modificateurs d'interfaces fibres-matrices dans le cas de composites à fibres courtes Al<sub>2</sub>O<sub>3</sub> SAFFIL (25 % vol.), ou encore comme renforts dans le magnésium pur. Quatre types de composites ont été élaborés par infiltration sous pression de gaz : l'alliage WFA ou le magnésium renforcés par des fibres courtes Al<sub>2</sub>O<sub>3</sub> SAFFIL recouvertes ou non de MWCNTs. Deux autres composites, dans lesquels le magnésium est renforcé par des MWCNTs (1 ou 2 % poids), ont été obtenus par métallurgie des poudres.

La microscopie électronique à balayage a montré que les microstructures des échantillons ainsi obtenus par métallurgie des poudres sont homogènes avec une bonne dispersion des nanotubes de carbone dans la matrice magnésium. Dans le cas des fibres SAFFIL recouvertes par des nanotubes, on n'a pas pu détecter la présence des MWCNTs après infiltration. Il se pourrait que, comme les fibres SAFFIL, les nanotubes soient complètement noyés dans la matrice, de telle sorte qu'ils sont invisibles à cette échelle sur les surfaces de rupture. Il n'en reste pas moins que le module de Young est sensiblement augmenté par le recouvrement des fibres SAFFIL par les nanotubes, ce qui pourrait refléter une meilleure liaison fibre SAFFIL -matrice.

Les propriétés élastiques et anélastiques d'échantillons des six composites ont été investiguées par spectroscopie mécanique. Les pertes mécaniques et le module de glissement ont été mesurés en fonction de la température. Les résultats montrent que les

MWCNTs influencent positivement les propriétés élastiques et anélastiques des composites par rapport aux matériaux composites sans nanotubes.

Une augmentation sensible de l'amortissement a été observée dans les composites WFA-25%SAFFIL-CNTs et Mg-25%SAFFIL-CNTs due aux additions de CNTs. Cela montre que l'interface SAFFIL-matrice serait « adoucie ». Pour interpréter cet « adoucissement », un modèle théorique est proposé qui considère les pointes des CNTs comme des concentrateurs de contraintes et donc des lieux favorables à l'émission des dislocations susceptibles de relaxer les contraintes d'interface. D'autre part, les CNTs loin de l'interface seraient des points d'ancrage supplémentaires pour les boucles de dislocations, diminuant leur mobilité à haute température. Le mouvement de dislocations contrôlé par un frottement de type sec est proposé comme mécanisme de relaxation des contraintes d'interface d'origine thermique.

Dans Mg-2%CNTs, l'amortissement est approximativement aussi élevé que dans le magnésium pur. Le spectre des pertes mécaniques dans Mg-1%CNTs et Mg-2%CNTs est composé d'un pic de relaxation et d'un fond exponentiel. L'enthalpie d'activation du pic est de 0.83 eV et le temps de relaxation limite de  $2.3 \times 10^{-11}$  s. Le pic est interprété par un modèle de traînage des atomes de soluté par les dislocations.

Un accroissement du module élastique de glissement a été observé dans WFA-25%SAFFIL-CNTs, Mg-25%SAFFIL-CNTs et Mg-2%CNTs dû à l'addition des CNTs. Hot Isostatic Pressing (HIP), qui a été utilisé dans l'élaboration de Mg-2%CNTs, s'est révélé avantageux pour obtenir des composites CNTs - Mg avec un meilleur interface.



# Contents

<b>Introduction .....</b>	<b>1</b>
<b>Chapter 1 Scientific background .....</b>	<b>3</b>
<b>1.1 Conventional metal matrix composites.....</b>	<b>3</b>
1.1.1 The matrix.....	4
1.1.2 The reinforcement .....	5
1.1.3 Processing .....	6
1.1.3.1 Liquid-state processes.....	6
1.1.3.2 Solid-state processes .....	7
<b>1.2 New type of composites with CNTs.....</b>	<b>8</b>
1.2.1 Carbon nanotubes.....	9
1.2.1.1 Atomic structures of carbon nanotubes.....	10
1.2.1.2 Properties of carbon nanotubes .....	12
1.2.1.3 Potential applications of carbon nanotubes.....	13
1.2.2 Advantages and challenges of using CNTs in MMCs .....	14
1.2.3 State of the art .....	15
<b>1.3 Aim of the work .....</b>	<b>16</b>
<b>Chapter 2 Processing.....</b>	<b>17</b>
<b>2.1 Synthesis and purification of carbon nanotubes.....</b>	<b>17</b>
2.1.1 Various methods of CNT synthesis.....	17
2.1.2 Chemical vapour deposition .....	18
2.1.3 Catalyst preparation.....	20
2.1.4 Synthesis of MWCNTs by CVD.....	20
2.1.5 Purification of MWCNTs.....	23
<b>2.2 Surface modification to improve wettability of CNTs.....</b>	<b>24</b>
2.2.1 Coating of plain MWCNTs .....	26
2.2.1.1 Dry method.....	26
2.2.1.2 Wet method .....	27
2.2.2 Coating of SDS - treated MWCNTs .....	28
2.2.3 Coating of MWCNTs with Mg .....	28
<b>2.3 MMCs processed by powder metallurgy .....</b>	<b>28</b>
<b>2.4 Use of CNTs to modify existing preforms: coating of         SAFFIL(<math>\text{Al}_2\text{O}_3</math>) fibers with CNTs.....</b>	<b>32</b>

<b>2.5</b>	<b>Obtained MMCs by gas pressure infiltration.....</b>	<b>34</b>
<b>Chapter 3</b>	<b>Experimental techniques.....</b>	<b>37</b>
<b>3.1</b>	<b>Scanning Electron Microscope .....</b>	<b>37</b>
<b>3.2</b>	<b>Mechanical spectroscopy .....</b>	<b>39</b>
3.2.1	Standard anelastic solid and Debye relaxation .....	42
3.2.2	Master curve method.....	46
3.2.3	Multiple relaxations.....	47
3.2.3.1	Discrete spectra .....	47
3.2.3.2	Continuous spectra.....	48
3.2.4	Relaxation mechanisms.....	50
3.2.4.1	Dislocation string model .....	50
3.2.4.2	The effect of the variation of the pinned dislocation segment length.....	52
3.2.4.3	Dislocation motion in solid solution: pinning-depinning .....	54
3.2.4.4	Hysteretic dislocation damping background in solid solution .....	55
<b>3.3</b>	<b>Forced torsion pendulum.....</b>	<b>56</b>
<b>3.4</b>	<b>Free-free vibrating bar apparatus .....</b>	<b>59</b>
<b>Chapter 4</b>	<b>Experimental results and interpretations</b>	
	<b>Al alloys - or Mg -25%SAFFIL-CNTs composites ....</b>	<b>63</b>
<b>4.1</b>	<b>Study of WFA (Al-4%Cu-1%Mg-0.5%Ag)-25%SAFFIL-CNTs composites .....</b>	<b>63</b>
4.1.1	Experimental results.....	63
4.1.1.1	Mechanical properties.....	63
4.1.1.2	Elastic shear modulus spectra.....	64
4.1.1.3	Internal friction behaviour.....	65
I	Mechanical loss spectra during thermal cycling .....	65
II	Effect of temperature variation rate .....	66
III	Effect of frequency .....	68
IV	Dependence of mechanical loss on $\dot{T}/\omega$ .....	70
4.1.2	Interpretation of internal friction behaviour .....	71
4.1.2.1	Model of Mayencourt et al.....	71
4.1.2.2	Interpretation of internal friction behaviour in WFA-25%SAFFIL-CNTs.....	72
I	General discussion.....	72
II	Interpretation of the effect of CNTs on the mechanical loss spectrum .....	75
1.	Theoretical modelling .....	76

2. Simulation of the mechanical loss maximum.....	77
<b>4.2 Study of Mg-25%SAFFIL-CNTs composites .....</b>	<b>80</b>
4.2.1 Mechanical loss and shear modulus spectra for two Mg-based composites .....	80
4.2.2 Relaxation mechanism of thermal stresses in Mg-25%SAFFIL-CNTs.....	83
4.2.3 Comparison of shear modulus .....	86
<b>4.3 Conclusion .....</b>	<b>87</b>
<b>Chapter 5 Experimental results and interpretations: Mg-MWCNTs composites .....</b>	<b>89</b>
<b>5.1 General features of mechanical loss and shear modulus spectra .....</b>	<b>89</b>
<b>5.2 Effect of thermal cycles with different temperature variation rates .....</b>	<b>93</b>
5.2.1 Mg-2%CNTs.....	94
5.2.2 Mg-1%CNTs.....	96
5.2.3 Summary.....	98
<b>5.3 Activation enthalpy .....</b>	<b>99</b>
<b>5.4 Theoretical modelling .....</b>	<b>102</b>
<b>5.5 Conclusion .....</b>	<b>104</b>
<b>Chapter 6 General discussions .....</b>	<b>105</b>
<b>6.1 Microstructures of the developed bulk CNTs-based composites .....</b>	<b>105</b>
<b>6.2 The impacts of CNTs on the elastic and anelastic properties of the CNTs-based composites.....</b>	<b>106</b>
6.2.1 Impacts of CNTs on Young's modulus and shear modulus .....	106
6.2.2 Impacts of CNTs on damping capacity .....	107
6.2.3 Reinforcement size effect .....	108
<b>6.3 Propositions for further research.....</b>	<b>110</b>
<b>Conclusion .....</b>	<b>111</b>

<b>Bibliography</b> .....	113
<b>Acknowledgements</b> .....	121
<b>Curriculum Vitae</b> .....	123
<b>Publications</b> .....	125

# Introduction

The aim of developing composites is to combine the mechanical properties of the components to meet diverse industrial requirements. In numerous fields of applications like aerospace and automobile industry, low density and good mechanical properties such as high damping, high strength and high stiffness are demanded for the materials. Most of the applications make use of discontinuously reinforced metals, mainly ceramic-reinforced Al. The stiffness of a metal matrix composite is strongly dependent on many parameters and factors such as the volumetric fraction of ceramic fibres,  $V_f$ , the elastic Young's modulus of the fibres and the matrix,  $E_f$  and  $E_m$ , and the aspect ratio of the fibres, as well as fibre disorientation and micro-damage at the matrix-fibre interface resulting from large interfacial thermal stresses, which increase with the size of the fibres. Modifying these parameters, arranging better the fibre's orientation and improving the interface can increase the stiffness. However, this increase is limited when using the conventional ceramic reinforcements, which are in micro-scale. On the other hand, increasing a mechanical property may cause a decrease in another, for instance, larger  $V_f$  may result in higher Young's modulus but lower damping capacity of the composite. Thus a new type of high-performance reinforcements is expected to make a breakthrough in composite development. The discovery of carbon nanotubes, with light weight, smaller dimensions and unique mechanical properties could fulfil further goals of higher damping capacity and better mechanical properties, compared to the conventional composites.

Carbon nanotubes are seamless cylinders of rolled up graphene sheets. They can exist as single wall or multi wall cylinders. Up to now, a number of methods for synthesizing carbon nanotubes have been reported, which can be grouped into three types: arc-discharged, laser ablation and catalytic CVD. The two formers can deliver carbon nanotubes with better quality, whereas CVD can yield larger amount of CNTs and is easy to scale up the products to meet industry demands.

Because of their attractive mechanical properties such as a very high Young's modulus and excellent flexibility as well as their large aspect ratio, CNTs could be a brand new class of

reinforcements for developing composites. The reduction of size with respect to the conventional reinforcements would minimize the interfacial thermal stresses.

In the present work, low gas pressure infiltration and powder metallurgy were utilized to process MMCs. In Al alloy (Al-4%Cu-1%Mg-0.5%Ag (WFA)) - 25% Al<sub>2</sub>O<sub>3</sub> (SAFFIL short fibres) - CNTs and Mg - 25% Al<sub>2</sub>O<sub>3</sub> (SAFFIL short fibres) - CNTs, CNTs are expected to behave as fibre-matrix interface modifiers. In Mg-1%CNTs and Mg-2%CNTs, they are supposed to be a nano-sized reinforcing phase.

This thesis consists in six chapters. In chapter 1, a review of conventional metal matrix composites and a summary of carbon nanotubes (atomic structures, properties, and potential applications) are presented. The advantages and challenges of the CNT applications in MMCs industry are predicted. The state of the art of CNTs-based composites as well as the aim of the work is described.

Chapter 2 covers the synthesis and purification of multi wall carbon nanotubes, methods and results of coating these nanotubes, and microstructures of the nanotube composites processed by two different routes. Theoretical approach and experimental techniques are described in chapter 3.

Experimental results measured in an Al alloy and in pure Mg reinforced with 25%SAFFIL, coated with CNTs, are presented in chapter 4. A theoretical model is developed in this chapter to interpret the results. Chapter 5 contains the mechanical spectroscopy of 1% CNTs and 2% CNTs reinforced pure Mg composites and the analysis by simulation.

General discussions are given in chapter 6, which is followed by a conclusion.

# Chapter 1

## Scientific background

---

### 1.1 Conventional metal matrix composites

The scientific investigation and applied research on composite materials can date back to 1940's [1], and these advanced materials have been introduced gradually in our daily life. Composites are also recognized as high-tech materials, which not only turn up in various sports, such as tennis, golf and sailing, but also constitute an increasing proportion of modern airplane and automobile [2]. A composite material is a mixture of two or more separate phases, matrix and reinforcements, which have been intimately bound together. The advantage is the combination of those different phases, providing a potential for tailoring material properties to meet specific and challenging requirements. The balance of the properties can be altered by the choice of the matrix and the level of reinforcement. Composites offer the only pathway for producing such advanced “designer” materials.

Most composites exploited in sport, aerospace and automotive industries consist of a reinforcing phase, such as glass or carbon fibers, and a polymeric matrix [2]. Polymers are chosen for matrix materials because of their low density, low cost, and easy procedure in composite processing. However, compared with polymers, metals have other advantages, which are wanted in diverse applications, such that they combine strength and toughness, which can be maintained even at elevated temperature, do not absorb humidity, are not degraded by radiation, do not outgas in space, generally do not burn, but can conduct heat and

electricity. With all of these desirable and interesting physical properties, metals were considered as matrices in composites although it would be significantly more difficult to process metal matrix composites (MMCs) than to produce polymer matrix composites. The pioneer research on metal matrix composites was taken off in the 1960's and reached its first peak activity in the early 1980's. By now metal matrix composites have indeed entered the engineering world as "real" industrial materials.

Currently, metal matrix composites are commercially available with a variety of forms. They are utilized predominately in a wide range of applications, ranging from brake discs in trains to critical rotating parts in helicopters, from thermal substrates for advanced electronic and power modules to spikes for track shoes, and from tool materials to combustion engine components, from structural to electronic applications [2]. However, the dominant applications focus on three sectors: (i) automotive and ground transportation, (ii) aerospace and defense, (iii) thermal management for electronics. In the sector of automotive and ground transportation, metal matrix composites are used for their specific stiffness, high temperature strength and excellent wear properties. In aerospace applications, metal matrix composites satisfy the principal requirements such as low thermal expansion coefficient, low density, high stiffness, and high strength. Indeed, in addition to the concern of absolute weight saving to reduce the launch costs, the primary demand in space technology is often the dimensional stability of the components, which are submitted to the inevitable thermal cycles associated with passing in and out of the Sun's shadow in the absence of convective heat transfer. Examples include beam structures and optical gimbals, which must not deform despite significant temperature fluctuations and gradients typical of space applications.

In order to obtain the specific properties of a metal matrix composite, a number of variables should be taken into account: the choice of the matrix, the type and the level of the reinforcement, and the composite processing route.

### **1.1.1 The matrix**

At present, a variety of metallic matrices, metals and their alloys, are employed in MMC industry. Examples include Al, Ti, Mg, Fe, Cu, Ni, W, Ag, Ni, Mo, Be, NiAl, AlCu, AlCuMg, Al-4%wtCu, Al-4%Cu-1%Mg-0.5%Ag etc. With their superior mechanical



properties such as light weight, excellent strength, toughness and resistance to corrosion, which are critically important in aerospace and automotive applications, aluminum and aluminum alloys predominate as metallic matrices in the MMC industry.

### 1.1.2 The reinforcement

In the most common metal matrix composites, the reinforcements are ceramics. The primary interests are in lighter ones such as SiC, Al<sub>2</sub>O<sub>3</sub> (for instance SAFFIL), B<sub>4</sub>C, TiB<sub>2</sub>, TiC, among which SiC and Al<sub>2</sub>O<sub>3</sub> are dominant. Other ceramic such as Si, TiB and Cr<sub>3</sub>C<sub>2</sub> are also used [2]. The ceramic reinforcements can take various forms in composites: particulates, whiskers, filaments, short fibers (also called chopped fibers or staple fibers) or continuous fibers, depending on the demands, such as design properties or cost. Most of the ceramic particulate reinforcements have lower cost than fibrous reinforcements. The processing of ceramic particulate reinforced metal matrix composites is simpler and lower-cost than that of fibrous metal matrix composites. Although particulate reinforcements provide inferior improvement in mechanical properties for metal matrix composites, the benefits from ceramic particulate reinforcements, including enhanced wear and erosion resistance, increased stiffness, higher damping and reduced thermal expansion, offer very interesting advantages with respect to the un-reinforced matrix. In the meantime, these composites can still retain the advantages of the matrix (metals and alloys) in terms of cost, processing and some other properties such as the ultimate tensile strength.

Generally, commercial short fibers and whiskers are available in bulk or after pre-processing into mats or preforms. Though short fiber and whisker reinforced metals display characteristics and advantages similar to those of metals reinforced with particulates, the greater capacity of elongated reinforcements to carry load transferred from the matrix and the inherently stronger nature of whiskers enable short fiber and whisker reinforced metals to exhibit superior properties than an equivalent particulate reinforced metal. Moreover, anisotropy, which is not evident in particulate reinforced metals, is microscopically apparent in short fiber and whisker reinforced metals.

In continuous fiber composites, an evident anisotropy resulting from the elongated fibers is macroscopically observed in the mechanical properties: very high strength and stiffness along the fiber direction and properties similar to those of discontinuous fiber composites in transverse direction. High-modulus metal-compatible fibers can increase the longitudinal Young's modulus dramatically, as for instance, alumina or carbon fibers in an aluminum-based matrix, with Young's modulus exceeding 200 GPa and 300 GPa, respectively.

In addition to ceramic reinforcements, metallic reinforcements have also been utilized in some occasions, as for example tungsten reinforced copper and copper-niobium superconductors. Gas can be a second phase in metal foams, which can also be viewed as metal matrix composites. Metal foams are still at the initial stage of development.

### **1.1.3 Processing**

Processing of metal matrix composites consists in combining the reinforcements (usually between  $0.5 \mu\text{m}$  and  $200 \mu\text{m}$  in diameter) with a metallic phase, with the aim of obtaining a new material free of defects such as pores. A variety of methods have been utilized in manufactures of conventional metal matrix composites. These methods can generally be sorted into four categories: solid-state processes, liquid-state processes, deposition processes and in-situ processes. Solid-state and liquid-state processes form the two primary categories.

#### **1.1.3.1 Liquid-state processes**

Basically, liquid-state processes imply using a molten metal. Infiltration, stir casting and spray casting are the three most common liquid-state processes, which are widely used to produce metal matrix composites [2]. In the infiltration technique a low-viscosity molten metal infiltrates through the porous preform of reinforcement, made of a continuous fiber bundle or a bulk of short fibers or whiskers. Stir casting consists of adding and stirring reinforcement particles or short fibers into the liquid metal. While spray casting consists of disintegrating a stream of liquid metal into droplets and injecting reinforcement particles that

are entrapped by the molten droplets so that both deposit together to form a composite. Liquid metal processes are rapid, inexpensive; suitable to produce parts with complicated shapes and easy to scale up. However they also have disadvantages such as the poor wetting of the ceramic reinforcements by the molten metal, which may limit the infiltration in the ceramic perform. On the other hand the contact between the liquid metal and the ceramic reinforcement may be responsible of undesired interfacial reaction, such as the formation of aluminum carbide phases, which can degrade the properties of aluminum alloys with carbon reinforcements.

Thermo chemical modifications can activate the wetting of the reinforcements by the liquid metal. Coating the reinforcements and using processing temperature much higher than the melting point may be an advantageous solution. However, these modifications may also be at the origin of undesired phases, which appear at the interface after a too long contact time between the liquid metal and the reinforcement and may degrade the composite properties. An alternative method to natural infiltration technique is pressure infiltration, in which a gas or piston is employed to push the liquid metal into the open pores of the preform. Usually a pressure of the order of 1 MPa is needed to drive the liquid metal into pores of 1  $\mu\text{m}$ , assuming a typical metal surface tension of 1  $\text{Jm}^{-2}$ .

In order to avoid undesired interfacial reactions, chemically compatible combinations of matrix and reinforcement may be selected, such as for instance magnesium-free aluminum and alumina. On the other hand, the undesired interfacial reaction can be limited by minimizing the contact time between the liquid metal and the reinforcements at high temperature.

### **1.1.3.2 Solid-state processes**

The classical approach of solid-state processes consists in blending the reinforcements with a powder of the metallic alloy and consolidating the mixture by powder metallurgy processes. More precisely, the mixture is consolidated and densified by cold pressing followed by sintering, or by hot pressing, hot isostatic pressing (HIP), or extrusion consolidation. In this step, the pores can be eliminated.

During such processes, both phases remain in solid state, thus the diffusion between these two phases is much lower than in liquid state processes, leading to weaker chemical interactions between the metallic powder and the ceramic reinforcement. However, if the diffusivity is too low, densification of the mixture will be not sufficient to build efficient interface between matrix and reinforcement. In some cases (magnesium and aluminum are typical examples), the diffusivity can be improved by breaking the oxide layer, which coats each matrix particle. On the other hand, the ceramic reinforcements do not sinter at the same temperature as the metal matrix, and consequently do not contribute to densification. Densification of the composite material is then lower than for the metal alone.

It has been proven that the relative sizes of the matrix powder and the reinforcement are critical for the densification of a composite. The particle size of the matrix powder has to be similar or smaller than that of the reinforcement. Usually it is about 1 to 10  $\mu\text{m}$  in diameter. Conventional powder metallurgy methods generally work well to fabricate MMCs with particulate reinforcements, but less well in the case of fibrous reinforcements. For example, it is not easy to blend a metallic powder with short fibers. On the other hand, the elongated reinforcements can be broken during consolidation.

## **1.2 New type of composites with CNTs**

The discovery of carbon nanotubes [3] has provided promising candidates as reinforcements for composites, because of their attractive mechanical properties where the stiffness, strength and resilience exceed any current materials. In the past decade, numerous attempts and efforts have been made by researchers, exploiting the exceptional mechanical properties of CNTs toward the development of CNTs reinforced composite materials. Polymers, ceramics and metals have been tried out as matrices [4 -13]. The primary success lies in polymers reinforced with carbon nanotubes. It was found that the exceptional properties of CNTs are the consequence of their unique structure.

## 1.2.1 Carbon nanotubes

In nature, carbon exists as solids in two basic forms: transparent diamond and black graphite (Fig.1.1). Diamond exhibits a very rigid, stable and hard configuration, where each carbon atom has four nearest neighbors arranged in a tetrahedron and the carbon atoms are in  $sp^3$  hybridized orbits. Whereas, graphite, with different atomic orbital state ( $sp^2$  hybridisation), consists of plane layers, called graphene layers, which are composed of carbon atoms in hexagonal structure and each carbon atom has three nearest neighbors. Thus the bonding in the plane is very strong. Whereas it is weak between the layers because the binding forces between layers are the relatively weak Van-de-Waals forces.

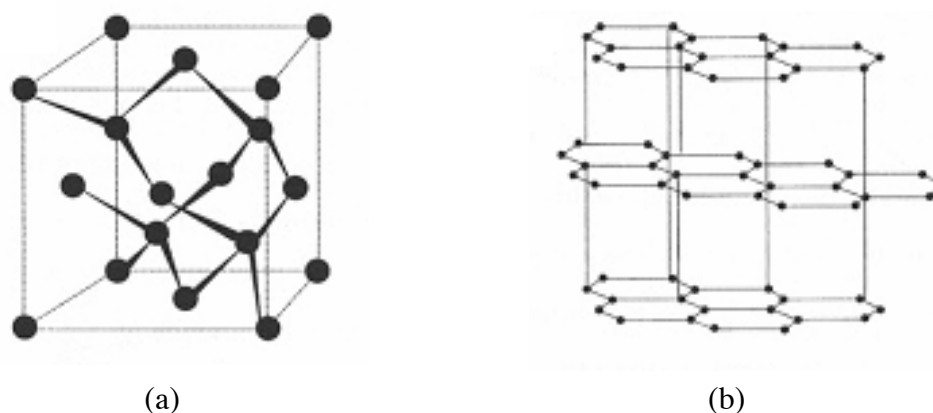


*Fig. 1.1: Structure of (a) diamond and (b) graphite.*

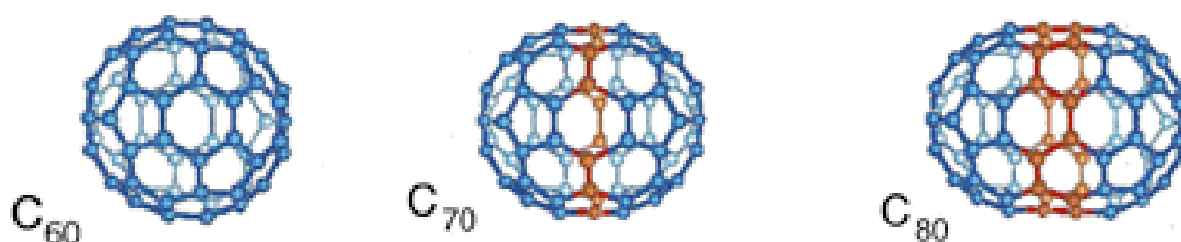


*Fig. 1.2: A new type of carbon: fullerenes.*

Fullerenes, discovered by Kroto et al. in 1985 [14], are a new type of carbon form. They are geometric cage-like structures of carbon atoms, which are composed of pentagonal and hexagonal faces in the surface of the cage. The first cage-like structure discovered

consists of 60 carbon atoms. It is a  $C_{60}$  molecule. Such a closed cage resembles a football where each side of a pentagon is the adjacent of a hexagon. Later similar cage-like forms with different number of atoms were observed (Fig.1.2).

Several years later after the discovery of fullerenes, in 1991, S.Iijima [3] discovered the carbon nanotubes. Actually, carbon nanotubes can be viewed as long and slender fullerenes where the walls of the tubes are of hexagonal structure. Carbon nanotubes can be divided into two main types that can have high structural perfection: single-wall carbon nanotubes (SWCNTs) and multi-wall carbon nanotubes (MWCNTs). Multi-wall nanotubes comprise simply an array of such single-wall nanotubes that are concentrically nested (Fig.1.3).

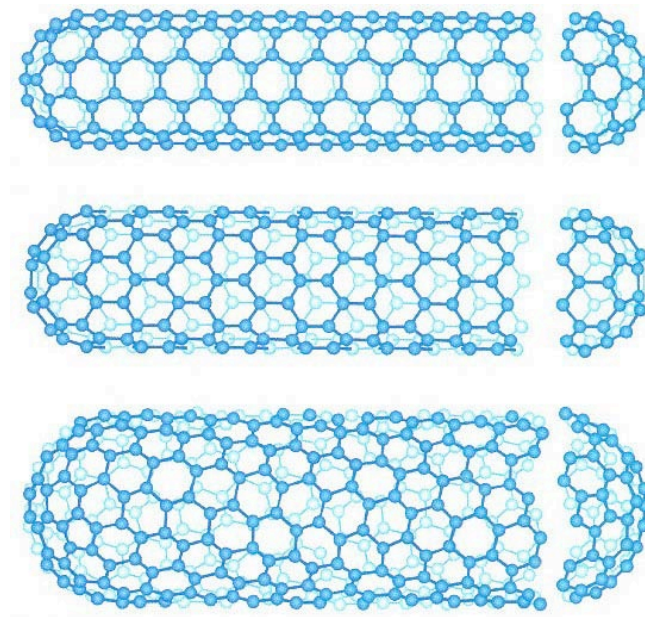


*Fig. 1.3: Schematic representation of single wall carbon nanotubes (SWCNTs).*

### 1.2.1.1 Atomic structures of carbon nanotubes

Fig. 1.4 shows a sheet of graphene plane with lattice unit vectors  $\vec{a}_1$  and  $\vec{a}_2$ . A single-wall carbon nanotube can be visualized as a rolled-up graphene plane which is cut along the dotted lines, as shown in Fig. 1.4. The atomic structure of nanotubes is described in

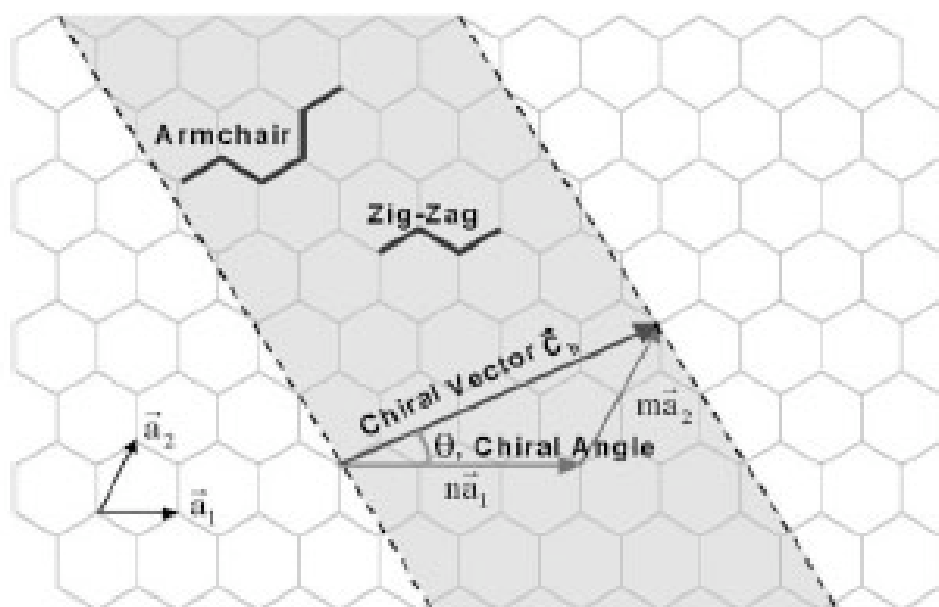


*Fig. 1.4:* Schematic diagram showing different directions for rolling a hexagonal sheet of graphite to form a carbon nanotube.

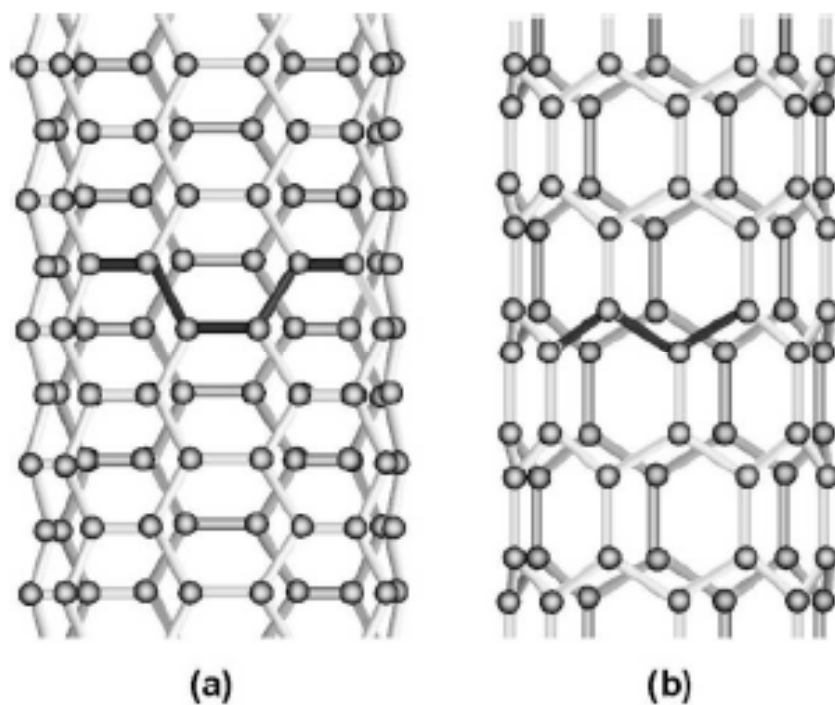


*Fig. 1.5:* Illustration of the atomic structure of (a) an armchair ( $n = m$ )  $\theta = 30^\circ$  and (b) a zig-zag ( $n = 0$  or  $m = 0$ )  $\theta = 0^\circ$  nanotube.

terms of the tube chirality, or helicity, which is defined by the chiral vectors,  $\vec{C}_h$ , and the chiral angle,  $\theta$  [15]. The chiral vector, also known as the roll-up vector, is given by

$$\vec{C}_h = n\vec{a}_1 + m\vec{a}_2$$

where the integers  $(n, m)$  are the number of steps along the ziz-zag carbon bonds of the hexagonal lattice. If the chiral angle is at  $30^\circ$ , i.e.,  $n = m$ , when the plane is rolled up till the tip of the chiral vector meets its tail, the geometry of the carbon bonds around the circumference of the nanotube has an armchair shape, while at a chiral angle of  $0^\circ$  ( $n = 0$  or  $m = 0$ ) the shape presents ziz-zag-like. Fig. 1.5 shows the difference between armchair nanotube ( $n = m$ ) and ziz-zag nanotube ( $n = 0$  or  $m = 0$ ) structures. The nanotubes with a chiral angle between  $0^\circ$  and  $30^\circ$  (any other  $n$  and  $m$ ) are called chiral. The chiral vector of the nanotube also defines the nanotube diameter since the inter-atomic spacing of the carbon atoms is known [15].

A typical diameter of single-wall carbon nanotubes falls between 1 and 2 nm. Whereas the outer diameter of multi-wall carbon nanotubes can disperse from 5 to 50 nm, with a distance of 0.347 nm between two adjacent layers.

### 1.2.1.2 Properties of carbon nanotubes

Due to their unique atomic structure, carbon nanotubes exhibit remarkable electronic, thermal, magnetic, mechanical and field emitting properties, which more or less depend on their chirality. In particular, the tube chirality has a strong impact on the electronic properties of carbon nanotubes. Although single-wall carbon nanotubes have structural similarity to a single sheet of graphite, which is considered to be semiconductor with zero band gap, it has been shown that single-wall carbon nanotubes can be either metallic or semiconducting [16]: armchair tubes are metals, zig-zag tubes and the tubes with  $n - m = 3k$ , where  $k$  is an integer, are semiconductors with tiny band gap, and all other tubes are semiconductors with wide band gap [17].



For metallic nanotubes, i.e., armchair ( $n = m$ ) SWCNTs and MWCNTs, the nearly one-dimensional electronic structure leads to electronic transport over long nanotube lengths without scattering. As a result, the nanotubes can carry high currents with essentially no heating [18, 19]. The electric-current-carrying capacity is 1000 times higher than copper wires. Thermal conductivity of CNTs is about twice as high as that of diamond. In vacuum, carbon nanotubes are thermally stable up to 2800 °C [20]. Field and light emission was observed from individual MWCNTs, from which electrons [21] and visible light [22] were emitted.

In addition to the superior properties described above, it is of special interest to mention the fascinating mechanical properties of CNTs. It has been shown theoretically and experimentally that CNTs are extremely stiff and strong, meaning that they have very high Young's modulus and tensile strength. However, they are of very low density [23, 24, 25]. Young's modulus, usually measured by AFM (Atomic Force Microscope) techniques, is greater than 1 TPa (Tera - Pascal) for an individual SWCNT (1.2 TPa for diamond) and at an average value of  $810 \pm 410$  GPa for MWCNTs grown by the arc-discharge method [26]. However, it is much lower for catalytically grown MWCNTs (about 100 - 150 GPa). This is due to the considerable influence of disorder, which is present in catalytic nanotubes (but absent in arc-grown nanotubes), on the elastic properties of the tubes [27]. Point defects, which may be present on the graphitic planes and can be removed to a great extent by high-temperature annealing, do not alter the mechanical properties of MWCNTs. On the other hand, slipping of nanotubes when they are assembled in ropes significantly affects the elastic properties, resulting in a considerable decrease in Young's modulus. It was also found that Young's modulus of MWCNTs is independent of tube diameter [27]. Simulations show that carbon nanotubes are remarkably resilient, sustaining extreme strain with no sign of brittleness or plasticity [28, 29].

### **1.2.1.3 Potential applications of carbon nanotubes**

Because of their outstanding properties, carbon nanotubes have been proposed for many potential applications. In particular, their high stiffness and ultimate strength and excellent resilience make them excellent candidates as reinforcements in composites. Nanotube field effect transistors are examples, which use the interesting electronic properties

of CNTs [30]. Such nanometer-sized electronic devices are promising for downsizing circuit dimensions. The field emission properties of CNTs, as a result of the extreme aspect (length-diameter) ratio, enable carbon nanotubes to be used as field emission electron sources for field emission devices such as flat panel displays [31, 32] and lamps [32]. These devices have advantages over conventional tungsten and molybdenum tip arrays. Nanotubes provide stable emission, long lifetimes, and low emission threshold potentials [31, 32]. While the light emitting property of MWCNTs may make them good scanning probe tips in Scanning Near-field Optical Microscope. CNT scanning probe tips for atomic probe microscopes are on the market. The cylindrical shape and tiny curvature radius enable imaging in narrow, deep crevices and improve resolution in comparison to conventional nanoprobes [33, 34, 35, 36]. Other potential applications include energy storage and energy conversion devices, sensors and hydrogen storage media etc.

### **1.2.2 Advantages and challenges of using CNTs in MMCs**

Incorporation of carbon nanotubes into metal matrix could potentially provide structural materials with dramatically increased Young's modulus and strength. This indicates that this new type of materials could meet higher requirements in mechanical properties demanded for some applications. On the other hand, by retaining the same level of mechanical properties, less material would be required; for instance, the walls of parts could be thinner. This could consequently lead to energy saving. Furthermore the reduction of their dimension, from micrometer scale of conventional reinforcements such as  $\text{Al}_2\text{O}_3$  fibers to nanometer scale of carbon nanotubes, could reduce thermal stresses at the interface between metal matrix and reinforcement. This decrease in interfacial thermal stresses may modify or improve the quality of the interface. It is known that high thermal stresses generated in composites may cause cracks at the matrix-fiber interface. These cracks can propagate into the metallic matrix, leading to further damage of the material. Therefore, using CNTs as reinforcements in MMCs could minimize the degradation in the material due to thermal stresses. Metal reinforced with CNTs composites, with potential mechanical properties, could find wide applications in aerospace, automotive industry and microtechniques, replacing conventional materials: alloys or conventional composites.

However, there are some critical challenges when using CNTs as reinforcements in MMCs. In order to take full advantages of the exceptional stiffness, strength and resilience of carbon nanotubes, it is of importance to insure a uniform dispersion of CNTs in the metal matrix, to establish a strong interface bonding between the CNTs and the surrounding matrix that provides effective stress transfer, as well as to avoid intra-tube sliding between concentric walls within MWCNTs and intra-bundles sliding within SWCNT ropes. Efforts are in progress to overcome these difficulties.

### 1.2.3 State of the art

One of the first realized major commercial applications of CNTs is their use as electrically conducting components in polymer composites [37]. Since then the focus of most of the research in nanotube - based composites has been on polymer-matrix materials [10, 12, 38- 43]. It was found by Qian et al. that with 1 %wt of carbon nanotubes, an improvement of 36 - 42 % in the elastic stiffness and of 25 % in the tensile strength was achieved in carbon nanotube/polystyrene composites [10]. It was demonstrated that the addition of 1 wt% of CNTs could provide the same increase in elastic modulus as 10 wt% of carbon fibers. The elastic modulus could be increased as high as 30 % when dispersion and interfacial bonding of CNTs in an epoxy matrix were improved [44].

Researchers also tried to take advantages of the exceptional mechanical properties, especially the extraordinary resilience, of carbon nanotubes by combining carbon nanotubes with a ceramic matrix. Ceramics are very stiff with excellent thermal stability and relatively low density. However, their brittleness impedes the use as structural materials. Ceramic reinforced with carbon nanotube composites are expected to provide high-temperature stability, outstanding toughness and creep resistance. Carbon nanotube / silicon-carbide (SiC) composites and carbon-nanotube / metal-oxide composites processed by hot pressing are examples [11]. It was reported that 10%wt carbon nanotubes increased the strength and fracture toughness by 10%, compared to the monolithic ceramics. In carbon-nanotube / metal-oxide composites produced by hot pressing, it was shown that CNTs did not provide the expected improvement in mechanical properties [45 - 49].

However, the research activity in using CNTs as reinforcements in metal matrix composites is still scarce, and metal matrix composites reinforced with CNTs have not yet been developed at a useful scale. In the limited number of reports [12, 13], the so-called metal matrix composites are in fact nanoscale composites, obtained, for example, by the electroless plating of carbon nanotube with cobalt.

### **1.3 Aim of the work**

The aim of the present research is therefore to develop the processing of bulk composite materials of aluminum or magnesium alloys reinforced with CNTs and characterize them by the measurements of their elastic and anelastic properties. In this work, catalytic MWCNTs were used although their elastic modulus is lower than that of arc-discharge MWCNTs, because the catalytic processing is easier to scale up. This study is to find out the feasibility of using carbon nanotubes as a new type of reinforcements in MMCs.

# Chapter 2

## Processing

---

### 2.1 Synthesis and purification of carbon nanotubes

#### 2.1.1 Various methods of CNT synthesis

Carbon nanotubes can be synthesized using several methods: electric arc-discharge, laser ablation and chemical vapour deposition (CVD). In the first period of nanotube research, nanotubes were mostly produced by electric arc-discharge and laser ablation. Chemical vapour deposition was subsequently developed to synthesize CNTs. In the method of electric arc-discharge, a graphite rod serves as an anode and another graphite rod as a cathode [3, 50, 51]. As the two graphite rods are brought close together in a He atmosphere, a discharge occurs resulting in the formation of a plasma. When a current (in the range of 70 to 100A) passes from the anode to the cathode in a He atmosphere, a rod-shaped deposit with a hard outer shell is obtained at the cathode. It is found that the shell contains dense bundles of MWNTs. The inner and outer diameter of these MWCNTs disperses in a rather large range. However, the favourite diameter measures 10 nm and the typical length is on the order of 1  $\mu\text{m}$ . The nanotubes tend to be very straight. SWCNTs (with diameters on the order of 1nm) can be produced by this method as well when replacing the graphite rod anode with a hollow graphite tube. The tube contains mixed powders of graphite and transition metal (i.e., Fe, Co, Ni) and /or rare earth metal (Y, Lu, Gd) catalysts, and other metals (i.e., Li, B, Si, Sn, Te, Pb...) [52, 53]. This method was originally discovered by Iijima and co-workers [54] and by

Bethune and co-workers [52]. Another method, laser ablation, was introduced to synthesize SWCNTs later on [55]. This process involves the laser ablation in a He atmosphere of a graphite target, which is impregnated with a transition metal catalyst. This method can be used to produce long bundles of single-wall carbon nanotubes. However, CVD, which is based on the decomposition of hydrocarbons such as acetylene or methane on catalytic particles (Fe, Cu, Co), is currently the most common method for the synthesis of carbon nanotubes, due to its capacity in producing variety of carbon nanotubes and industrial up-scaling.

## 2.1.2 Chemical vapour deposition

In the chemical vapor deposition process, chemical reactions occur, which involve transforming gaseous molecules, called precursor, into a solid material on the surface of a substrate such as silica and zeolite. CVD is a very versatile crystal growth process. The products by CVD can be in different forms: coatings, powders, fibers and monolithic parts. With this method, it is possible to produce almost any metallic or non-metallic elements, including carbon and silicon, as well as compounds such as carbides, nitrides, borides, oxides, intermetallics and many others [56, 57].

Various configurations [56], which have been developed for chemical vapour deposition, include horizontal or vertical tube reactors, showerhead reactors or reactor with plasma enhancement. Horizontal and vertical tube furnaces are widely used in semiconductor processing due to their simplicity and productivity. They consist in principle of a heated tube with a gas inlet and outlet. The gas pressure in the tube can thereby vary between some fractions of millibar and some bar. Showerhead reactors employ a perforated or porous planar surface to dispense reactant gases more or less homogeneously over a second parallel planar surface holding the substrate on which the samples are installed. The samples can be heated separately from gas dispense and chamber wall, thus the showerhead reactors are generally cold-wall: only the surface holding the substrate needs to be at the process temperature. This often helps in minimizing deposition on chamber walls. Inside the reactors with plasma enhancement (PECVD), a radio-frequency (RF) source excites electrons in an electromagnetic field set up between the top electrode and grounded substrate by applying an alternative voltage, typically 60 Hz to many MHz. Ions, reactive neutrals or plasma are formed when the

excited electrons collide with gas molecules. The advantage of PECVD is its capacity to deposit at much lower temperatures and pressures than would be required for thermal CVD. However, a disadvantage is usually a higher disorder in the created structures and a lack of uniformity over larger surface areas. Each of the designs utilizes different methods for performing the fundamental operations common to all CVD removing by products. CVD processes can generate a vast variety of structures using different catalysts, gases, temperatures or gas pressure.

The first attempt of using CVD to grow MWNTs was carried out in 1993 [58]. In this process, firstly the decomposition of acetylene ( $C_2H_2$ ), the carbon source, takes place at  $700\text{ }^\circ\text{C}$  at the surface of small iron particles, which were served as catalysts. Then the carbon is dissolved in and diffuses through the particle. When supersaturation is achieved, carbon is segregated in a  $sp^2$  state to avoid dangling bonds, consequently, a carbon nanotube forms.

In the past years, catalytic decomposition of gaseous carbon source has been considered as the principle method of CNT synthesis in large-scale, which is essential for industrial applications. Various catalysts (typically Fe, Ni, Co or their oxides) and carbon sources (typically  $C_2H_2$  or  $CH_4$ ) have been tried out. This method has been recently efficiently improved by introducing catalyst supports such as silica [59] and zeolites [60, 61] and later alumina [62] etc. It is found that the catalysts play an important role in determining the diameter of the tubes. Therefore the preparation of the catalyst particles is a key step for the growth of CNTs. Moreover, the nature of catalyst supports is critical for up-scaling the production. Recent results based on silicagel - or zeolite - supported catalysts [59, 63, 64, 65] reveal that porous materials are excellent supports in catalytic nanotube production. However, for the subsequent purification of CNTs, which is usually the important step before various studies and applications, the existing techniques to purify the carbon nanotubes are problematic [66, 67] and require a multi-step purification [60], which can damage the structure of the tubes, leading to a degradation of the properties of the nanotubes. It is necessary to improve CVD techniques and choose the catalyst supports for synthesizing CNTs in large quantity with high quality. Therefore a new approach is expected to keep the amount of contaminants as low as possible, to use rather diluted mineral acids for purification and to simplify the procedure of the purification. A new kind of catalyst support ( $CaCO_3$ ) was

introduced for MWCNT synthesis with high efficiency and purity and the procedure of purification was simplified as one step-procedure [68].

### 2.1.3 Catalyst preparation

For the catalyst process, a calculated amount of metal salt ( $\text{Co}(\text{CH}_3\text{COO})_2 \cdot 4\text{H}_2\text{O}$  and/or  $\text{Fe}(\text{NO}_3)_3 \cdot 9\text{H}_2\text{O}$  or  $\text{Fe}(\text{CH}_3\text{COO})_2$ ) was dissolved in a certain amount of distilled water and subsequently  $\text{CaCO}_3$  was suspended into the solution for the catalyst preparation. The total concentration of the catalysts (Co, Fe (II), Fe (III)) was 5 wt%. The pH-value of the suspension was kept constantly at about 7.2 during the synthesis of the catalysts by adding ammonia solution. The resulting mixture was placed in a beaker on a hot plate and the solvent was evaporated under continuous stirring. The as-prepared sample was dried at 120 °C overnight and then collected as dry powders. The obtained catalysts supported by  $\text{CaCO}_3$ : Co/ $\text{CaCO}_3$ , Fe (II)/ $\text{CaCO}_3$ , Fe (III)/ $\text{CaCO}_3$ , Fe (II), Co/ $\text{CaCO}_3$  and Fe (III), Co/ $\text{CaCO}_3$ , were used in synthesis of carbon nanotubes by CVD.

### 2.1.4 Synthesis of MWCNTs by CVD

A catalytic growth of CNTs was carried out by decomposition of hydrocarbons (acetylene ( $\text{C}_2\text{H}_2$ )) at 720 °C in a fixed-bed flow reactor. The used horizontal CVD flow reactor is a heated quartz tube (Fig.2.1). Approximate 50 mg of prepared supported catalysts was placed in a quartz vessel, which was situated within the quartz tube.

During the CVD procedure, an acetylene gas flow at a rate of 10 ml/min was introduced for 30 min under a continuous nitrogen flow at a rate of 70 l/h. The decomposition of the acetylene gas and the nanotube growth were activated by the catalysts. The gas was decomposed into  $\text{C}_2 + \text{H}_2$  and the nanotubes were spun over the catalysts, which were supported by  $\text{CaCO}_3$  particles. After rinsing the system with nitrogen, the reaction products were collected. However, in this way, the amount of the products yielded per day was limited, because the size of the quartz vessel was small (12 mm in diameter and 200 mm in length of heated area) and the processing of CNTs could not be performed continuously.



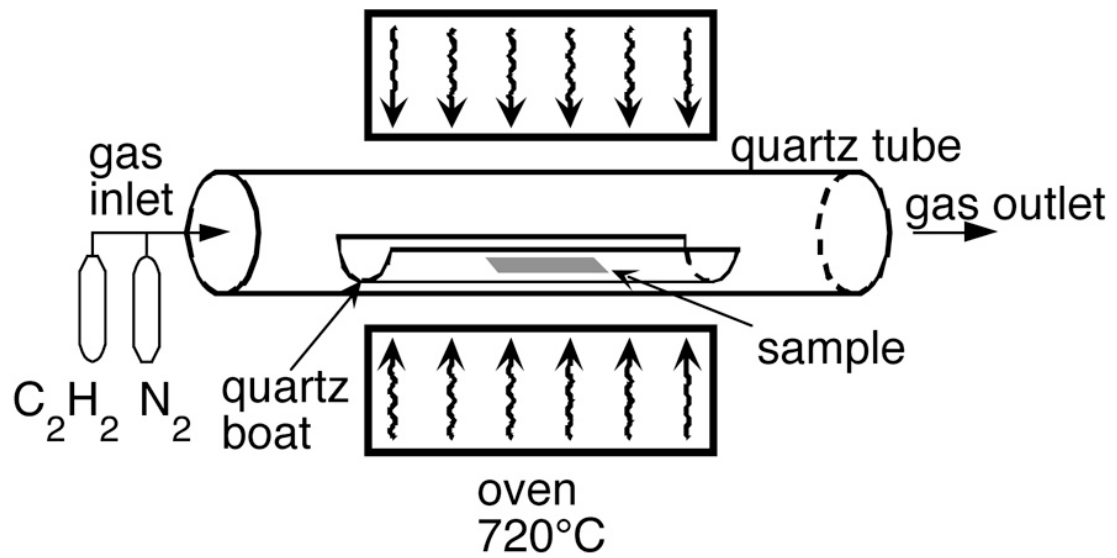


*Fig. 2.1: CVD (chemical vapour deposition) device.*



*Fig. 2.2: View of the rotary-tube oven used for large-scale synthesis of CVD nanotubes. Two reservoirs are located at the ends of the tube, one containing the catalyst (right-hand side) and the other collecting the product (left-hand side).*

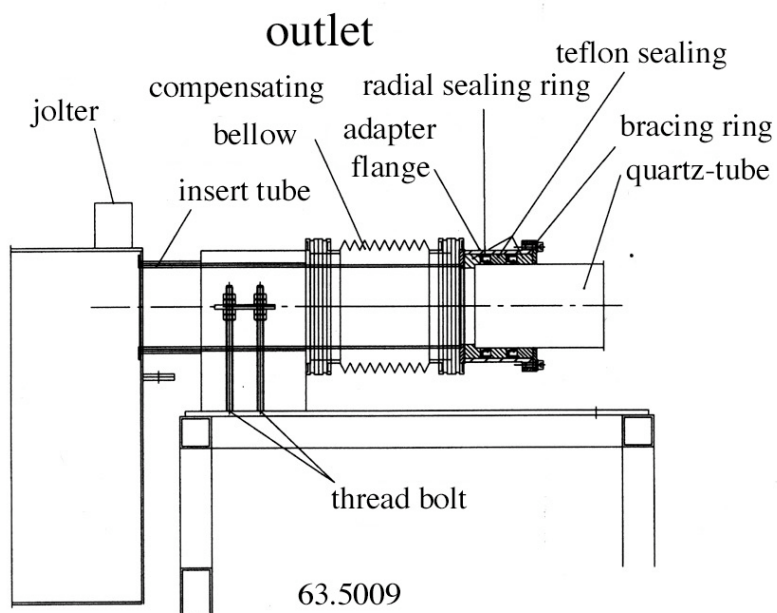
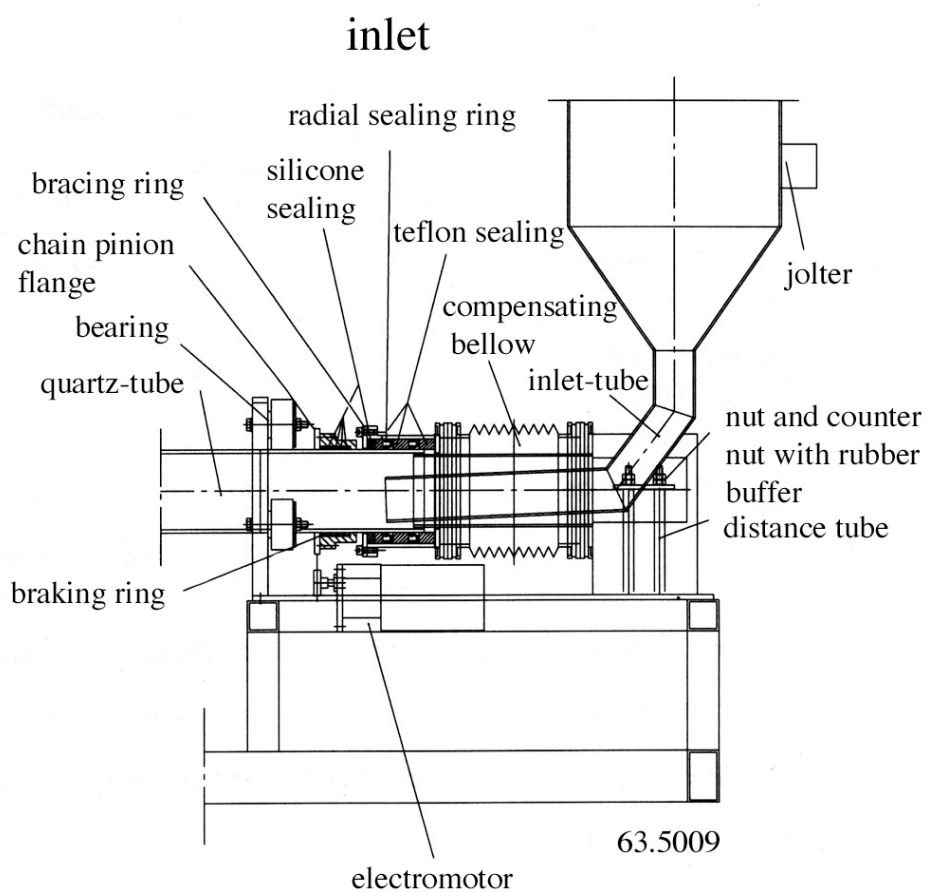


**Fig. 2.3:** Schematic diagram of the rotary-tube oven shown in Fig. 2.2.

In order to produce carbon nanotubes in larger scale in a continuous process, it is necessary to modify and improve the CVD techniques. Fig.2.2 and 2.3 show a photograph and a schematic diagram of the new CVD reactor developed in our laboratory, respectively. An 80 mm diameter rotating tube with heated area of 750 mm length was installed inside an oven. The rotating tube can be inclined and the inclination is manually adjustable to avoid blocking the catalytic particles and products when they pass through the reactor during the processing. The reactor is equipped with two containers, one containing the catalysts and the other collecting the products. The catalysts are introduced into the reactor by gentle shaking of the motor-driven feeder. The speed of the catalysts passing through the heated zone can be controlled by setting the inclination and the rotation of the reaction tube. The flow rotation is preferable for better productivity of nanotubes, because flow rotation can enhance the catalytic particles and the gas acetylene contact. It was also observed that the time factor, during which the catalysts stayed in the heated area, was critical for the growth of MWCNTs. More precisely, when the catalysts passed through the heated zone too fast, the time was too short to grow MWCNTs over all the catalytic particles. In other words, only a part of the catalysts, which passed through the tube during the reaction, were used to synthesize MWCNTs. As a result, the process would yield less MWCNTs than what could be expected. In contrary, when the time was longer, more catalysts were involved in the MWCNT growth. Then a larger amount of MWCNTs would be obtained. However, if the speed of the catalysts passing through the reactor was too low, some of the MWCNTs were burnt before they were collected in the container, because during the synthesis procedure, oxygen would be formed from the decomposition of the catalyst supporters. As a consequence, the products contained less MWCNTs. It was found that the best duration of time, during which the catalysts went through the heated zone, was 30 min for 100 mg of catalysts. Other processes such as heating, cooling and gas switching were automatically controlled. The obtained MWCNTs were found to be quite regular with an average inner (outer) diameter of 4 - 7 nm (15 - 25 nm) and with lengths up to 50  $\mu\text{m}$ .

### **2.1.5 Purification of MWCNTs**

The raw products of MWCNTs synthesized by CVD contained amorphous carbon, catalysts and their supports ( $\text{CaCO}_3$ ). Since the amorphous carbon can affect and even hinder the interaction between the nanotubes and the coverage materials, the nanotube surface has to

be cleaned before the initial stage of the composite preparing. Hence the purification is the primary step. At room temperature, the raw products of MWCNTs were sonicated in diluted nitric acid (30%  $\text{HNO}_3$ ) for 30 min, subsequently filtered and washed with distilled water to acid-free and finally dried at 120 °C overnight. Diluted nitric acid was used to dissolve catalytic particles and the supporters ( $\text{CaCO}_3$  particles). Since 1 g of  $\text{CaCO}_3$  reacts with 1.26 g of nitric acid during the purification, and the latter amount can be obtained in approximate 4  $\text{cm}^3$  30 % nitric acid, both catalytic particles and the supporters can sufficiently be dissolved by multiplying the volumes of 4  $\text{cm}^3$  30 % nitric acid. Fig.2.4 shows a TEM image of a purified MWCNT. It exhibits regular shape of walls, which are very well graphitized.

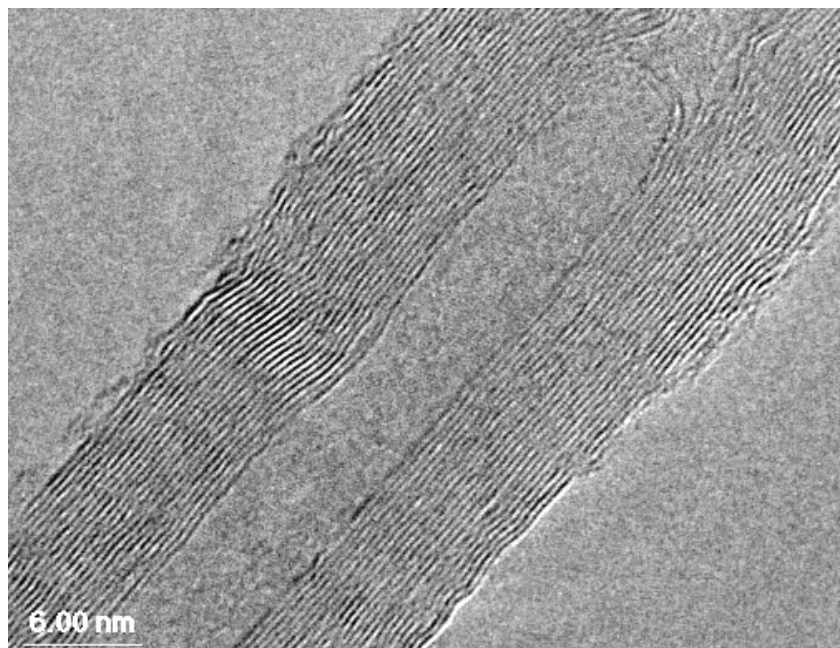


*Fig. 2.4: TEM image of a purified catalytic MWCNT.*

## 2.2 Surface modification to improve wettability of CNTs

Due to their extraordinary mechanical properties [69, 70], CNTs have been expected to be promising candidates as reinforcing materials in composites. In fact, in the past few years, a lot of efforts have been made in using CNTs (SWCNTs and MWCNTs) to reinforce different polymers [71, 72, 73, 74]. A couple of metal-based composites reinforced with CNT

have been reported as well [75, 76]. However, these nanoscale composites can not meet large-scale industrial needs. Bulk metal-based reinforced with CNTs materials are therefore in demand.

As reinforcements in composites, CNTs must be bonded to the surrounding matrix in an efficient way so that the load can be transferred from the matrix to the nanotubes sufficiently. This requires an effective interaction (or an interface) between the nanotubes and the surrounding matrix. The main encountered obstacle, which impedes building such a bonding, is the poor wettability of carbon nanotube surface by the matrix. The critical issue then focuses on how to improve the wettability of carbon nanotube surface. Several references on processing of CNT-based composites have pointed out the importance of good interfacial bonding, unfortunately without specifying in detail what determines the interaction between nanotubes and the matrix [77, 78, 779, 80]. In the last years, researchers have been investigating the routes to enhance the wettability of carbon nanotube surface. The wettability of CNTs could be improved by oxidizing or coating the surface of the nanotubes. The simplest method to oxidize the carbon nanotubes is a heat treatment of the nanotubes. It was observed that oxidizing CNTs by heat treatment could increase the interfacial bonding strength between the CNTs and the matrix [79, 80]. This indicates that the purity of the CNTs, which can be obtained by the procedure described in §2.1.5, is an important factor for interfacial interaction.

Coating of MWCNTs with alumina, silica, titania and magnesium has been performed successfully in our laboratory by K. Hernadi et al [68, 81, 82]. The processes are described below.

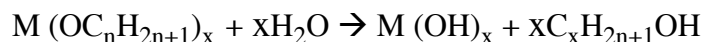
As starting materials, purified MWCNTs were used as plain (as purified) or modified by surfactant (sodium dodecyl sulphate (SDS), (SDS-treatment is also called soap-treatment)). For SDS treatment of MWCNTs, 200 mg of purified MWCNTs was sonicated in distilled water, and then 2 g of surfactant (Na dodecyl sulfate) was added. Subsequently, this suspension was filtered using a membrane with 0.1  $\mu\text{m}$  pore diameter and dried at 100 °C overnight. These two types of MWCNTs were impregnated in liquid or melted compounds. The impregnation was performed with or without solvent (isopropanol). More precisely, the former impregnation involved MWCNTs dispersed in isopropanol via sonication, while the later used MWCNTs directly suspended in liquid or melted compound under nitrogen. To

simplify these two expressions, the impregnation treated with isopropanol is hereafter named as “wet” method, whereas the direct impregnation as “dry” method. Both organometallic and inorganic compounds were applied as coating element sources such as aluminium trichloride ( $\text{AlCl}_3 \cdot 6\text{H}_2\text{O}$ ) and aluminium isopropoxide ( $\text{Al}(\text{OC}_3\text{H}_7)_3 \cdot 6\text{H}_2\text{O}$  (AIIP)) for aluminium coating, whereas magnesium ethoxide ( $\text{Mg}(\text{OC}_2\text{H}_5)_2$ ,  $\text{Mg}(\text{OEt})_2$ ,  $\text{MgCl}_2$ ), tetraethyl orthosilicate ( $\text{Si}(\text{OC}_2\text{H}_5)_4$  (TEOS),  $\text{Si}(\text{OEt})_4$ ), and tetraethyl orthotitanated ( $\text{Ti}(\text{OC}_2\text{H}_5)_4$  (TEOTi),  $\text{Ti}(\text{OEt})_4$ ) for magnesia, silica and titania coatings.

## 2.2.1 Coating of plain MWCNTs

### 2.2.1.1 Dry method

With this method, 20 mg of plain MWCNTs (as purified MWCNTs) was suspended in a surplus amount of organometallic compound under nitrogen [82]. In the case of AIIP, the plain MWCNTs and the solid AIIP were directly mixed in nitrogen atmosphere. The mixture was subsequently covered, stirred and heated up to approximately 140 °C, which is slightly higher than the melting point of AIIP (134 - 138 °C). In order to obtain a sufficient dispersion of the MWCNTs in the melted compound, stirring was necessary to overcome the rather high viscosity of the materials. In a few cases, the sample was sonicated for about 30 min in nitrogen atmosphere. The organometallic compounds were hydrolyzed by adding a few drops of distilled water. The general formula of the chemical reaction is described here below



where n is 2 or 3 and M is Al, Si or Ti. In the last step of the impregnation, the samples were dried in a heated magnetic stirrer and the carbon nanotubes coated with inorganic materials were heated at 250 °C for 8 hours. During the final heat treatment, a further decomposition of  $\text{M}(\text{OH})_x$  happened, providing the oxide or oxide-hydroxide forms. However, the carbon nanotubes were safe, because the decomposition of carbon nanotubes happens only when the temperature is higher than 650 °C. Under transmission electron microscope (TEM), the

samples revealed a homogeneous coverage by inorganic compounds: alumina, silica and titania at the surface of MWCNTs (Fig. 2.5) [82].

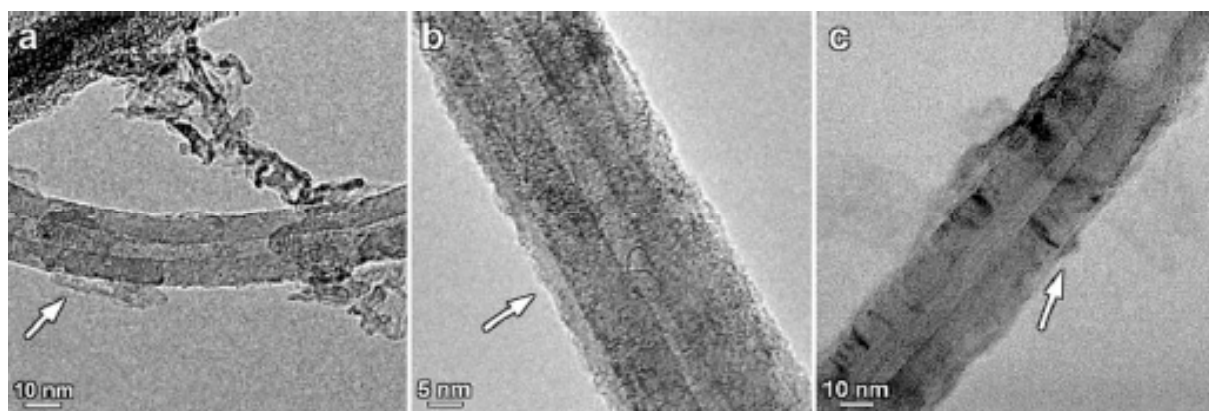


**Fig. 2.5:** TEM images of MWCNTs composites synthesized from solvent-free suspensions of different organometallic compounds: the arrow indicates the obtained coating in each image. (a) Carbon nanotubes with alumina together with a few needle-like crystals. (b) Homogeneous coverage of about 3 nm was obtained with silica. (c) MWCNTs coated with titania: the thickness of the layer is continuous but irregular compared to the other coating materials.

### 2.2.1.2 Wet method

This method has been applied for the coating of the MWCNTs with AIP or  $\text{AlCl}_3 \cdot 6\text{H}_2\text{O}$  sources. The impregnation of MWCNTs with AIP or  $\text{AlCl}_3 \cdot 6\text{H}_2\text{O}$  was carried out in isopropanol. In the case of AIP source, 20 mg of plain MWCNTs was impregnated with 50 mg of AIP in an isopropanol suspension in nitrogen atmosphere. The AIP was hydrolyzed by introducing distilled water. Then the solution was dried on a heated magnetic stirrer. With  $\text{AlCl}_3 \cdot 6\text{H}_2\text{O}$  source, 20 mg of plain MWCNTs was mixed with a surplus amount of  $\text{AlCl}_3$  suspended in isopropanol. Subsequently the same heated magnetic stirrer was employed to dry the mixture. And  $\text{AlCl}_3$  was thermally decomposed in the final heat treatment at 250 °C for 8 hours. However, the results show that with the presence of isopropanol solvent, no significant coverage is observable at the surface of MWCNTs [82].

## 2.2.2 Coating of SDS - treated MWCNTs

Alumina, silica and titania coatings of SDS-treated MWCNTs have been tried out in wet method as well [81, 82]. 20 mg of SDS-treated purified MWCNTs was dispersed in isopropanol by sonication. Then a surplus amount of organometallic compounds was introduced under nitrogen atmosphere and the suspension was stirred for 4 hours. In the case of coating of MWCNTs with alumina using AIP or  $\text{AlCl}_3 \cdot 6\text{H}_2\text{O}$  sources, for the modification of MWCNTs, a variation of the surfactant (SDS) proportion was also attempted: 120 mg of surfactants for SDS treatment of 120 mg of purified MWCNTs [81]. It has been observed that the impregnation of MWCNTs with AIP, TEOS or TEOTi sources was poor in wet method. The coverage of the coating elements at the surface of SDS-treated MWCNTs was thin and irregular. In contrary, a thick homogeneous layer of amorphous alumina was obtained using  $\text{AlCl}_3 \cdot 6\text{H}_2\text{O}$  sources. Dry method was also employed for impregnation of SDS-treated MWCNTs [81, 82]. However, no significant coverage turned out.

## 2.2.3 Coating of MWCNTs with Mg

In order to improve the wettability of the system “MWCNTs-Mg”, coating of MWCNTs with Mg has been performed using the same methods described in §2.2.1. In this process, organometallic and inorganic sources were applied for impregnation of SDS-treated MWCNTs. The results showed that a 2 nm thick homogeneous coverage of Mg was obtained at the surface of MWCNTs [68].

## 2.3 MMCs processed by powder metallurgy

Magnesium matrix reinforced with different percentages of MWCNTs were successfully processed by powder metallurgy, commonly designated by its initial letter as PM or P/M. Mg-1wt%MWCNTs was processed by hot pressing, whereas Mg-2wt%MWCNTs was synthesized by hot pressing then hot isostatic pressing (HIP) under high pressure. Sintering, an assembling of loose or compacted particles metallurgically bond into a coherent body at elevated temperature, is almost invariably carried out under a protective atmosphere,



because of the large surface areas involved, and at temperatures between 60 and 90% of the melting-point of the particular metal or alloys [83]. In order to obtain high density parts, it is better to increase the sintering temperature, which sometimes can be even higher than 90% of the melting temperature. The welding together of the particles occurs by atomic diffusion and generates the strength required for application. In this work, the atomic diffusion is also expected to enable the MWCNTs to be efficiently embedded in the magnesium matrix, providing a good interface through which the load can be transferred from the matrix to MWCNTs. Hot isostatic pressing is a process, which involves using a high-pressure gas isostatically to press a part or workpiece at an elevated temperature performed in a special controlled pressure vessel. When consolidating metal powders, the HIP process plastically deforms the powder, which closes up porosity and achieves 100% theoretical density in the part. HIP is a process to remove porosity.

In the processing of Mg-2wt%MWCNTs, 0.4 g of purified MWCNTs was oxidized by heat-treatment in a furnace at 500 °C for 5 min then cooled down to room temperature in air. These heat-treated MWCNTs and 19.6 g of commercial Mg powders (99.8 % purity, average particle size 38 μm) were placed in a container (5.5 cm in diameter and 4.5 cm in height), subsequently the MWCNTs and Mg powders were mechanically mixed by dry blending for 4 h in a Turbula T2C mixer (Fig.2.6). In order to separate the MWCNTs from the agglomerate state (the purified MWCNTs were agglomerated due to the intermolecular van-der-Waals interactions between the nanotubes) and to mix MWCNTs with Mg powders sufficiently, 10 ceramic (Al<sub>2</sub>O<sub>3</sub>) balls were added into the container. After blending of the mixture, no agglomerates of MWCNTs were visible and this indicates that both materials were well mixed together. The blends were placed in a double-action graphite tooling consisting of a die and two cylindrical pistons (Fig.2.6). The graphite tooling containing the mixture was mounted in a Sintris 10STV hot press (Fig.2.6) and hot pressed under following processes: in vacuum, the sample was heated up from room temperature to 500 °C at a heating rate of 50 °C /min then from 500 °C to 600 °C at a heating rate of 10 °C /min under a pressure of 50 MPa. After sintering at 600 °C for 30 min, the sample was cooled down to room temperature and a disk-shaped compact (Ø 53 mm x 5mm) was obtained. Finally, the compact underwent hot isostatic pressing at 600 °C for 60 min under an argon pressure of

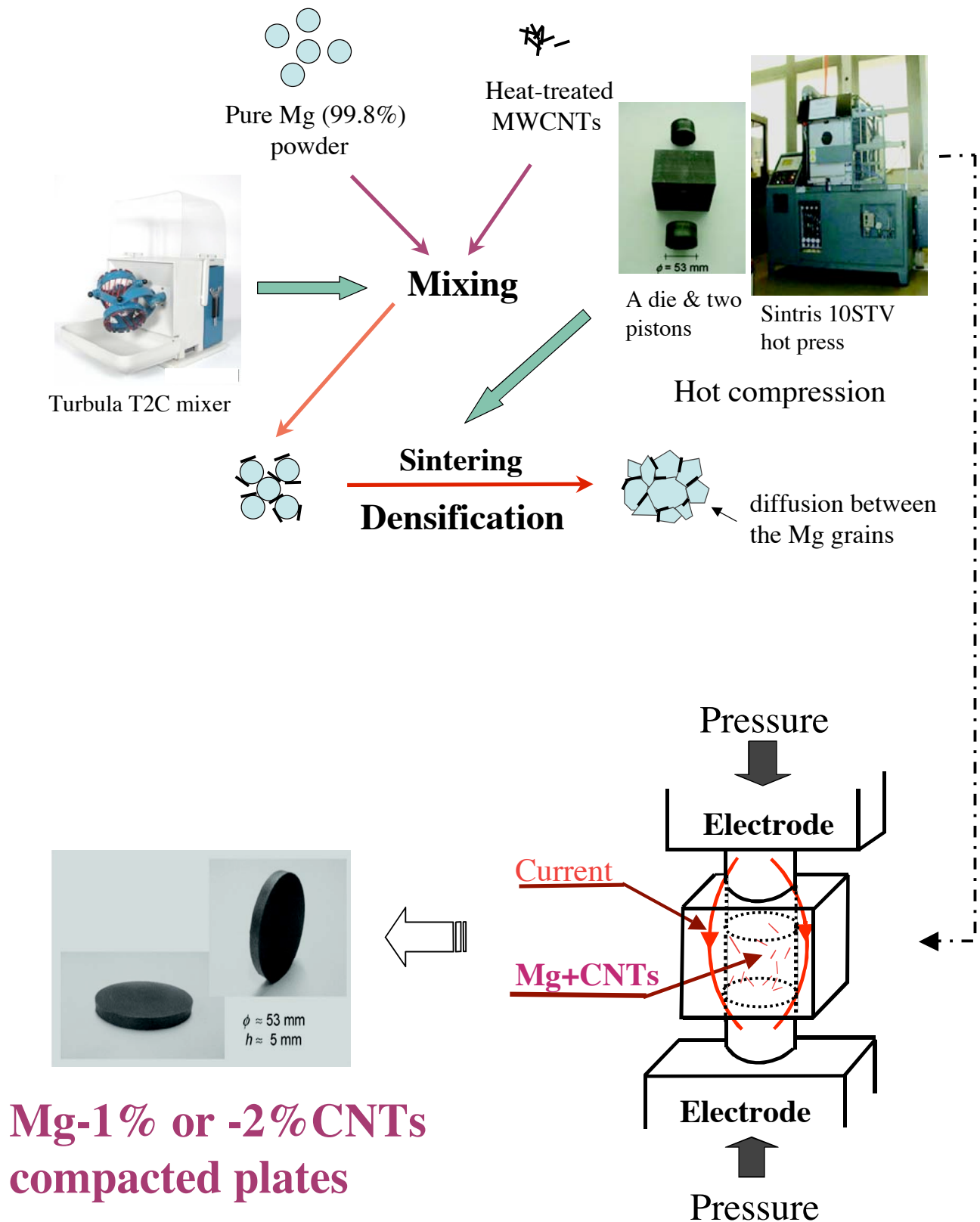


**Fig. 2.6:** The procedure of processing Mg - CNTs by powder metallurgy (Haute école valaisanne - Materials & Design Group, University of Applied Sciences of Western Switzerland).

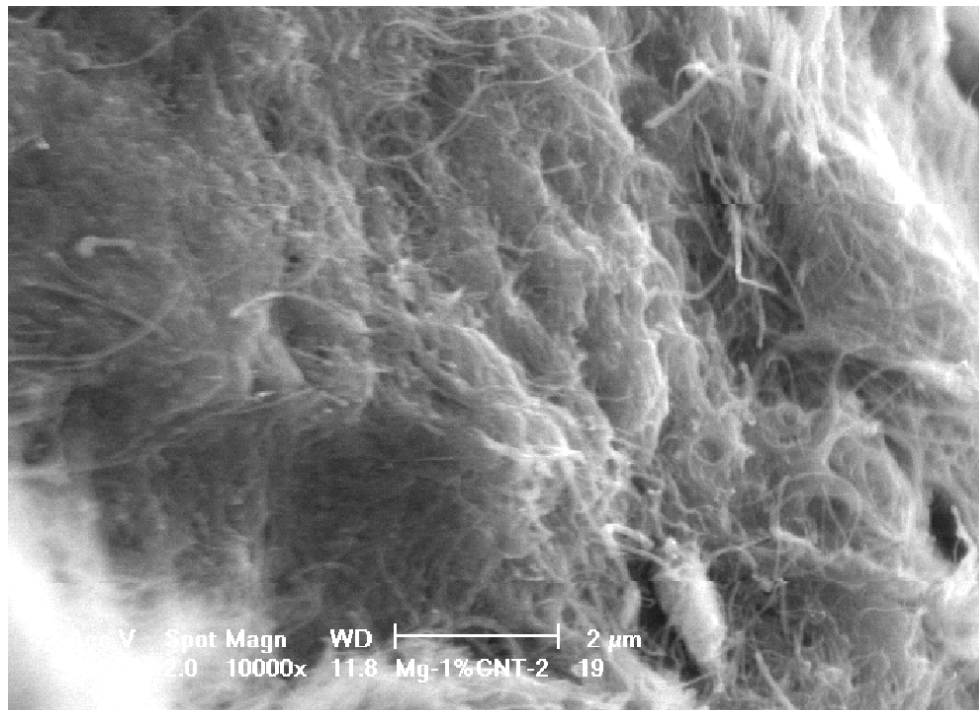


*Fig. 2.7: SEM image of fracture surface of Mg-1wt% MWCNTs.*

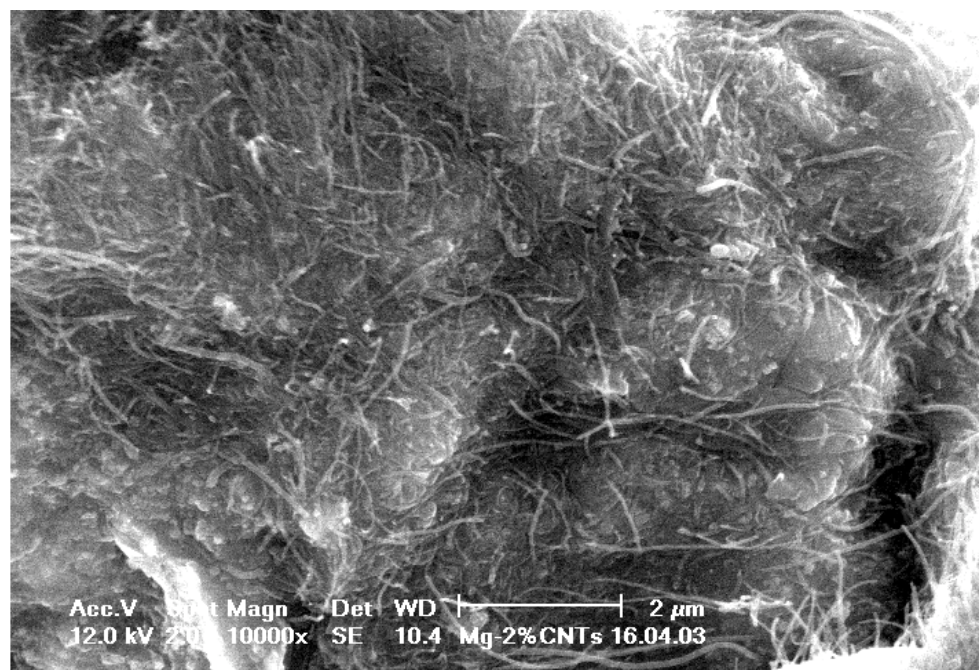


*Fig. 2.8: SEM image of fracture surface of Mg-2wt%MWCNTs. Homogeneous dispersion of MWCNTs in Mg matrix.*

1800 bar. The surface of compact was polished with a diamond pad before the density of the sintered part was measured by the Archimedes method.

A Mg-1%MWCNTs was processed by the similar method as that to obtain Mg-2%MWCNTs. However, instead of using dry method, a mixture of 0.2 g of heat-treated MWCNTs and 19.8 g of Mg powders was manually wet mixed in an alcohol and acid then it was dried. The used sintering temperature and the pressure were 550 °C and 25 MPa, respectively. This obtained Mg-1%CNTs composite did not experience hot isostatic pressing. In this case, two steel plates were used and the mixtures were placed between them.

Fig. 2.7 and 2.8 show the microstructure of specimens with 1 or 2 wt% of CNTs after fracture. In Fig. 2.7 and 2.8, one can note that the CNTs are embedded in the magnesium matrix better in the case of 2 wt% of CNTs, which underwent HIP, than in the case of 1wt% of CNTs. Sintering parameters (pressure, temperature) have to be optimized in order to increase the specimen density and consequently the mechanical properties.

## **2.4 Use of CNTs to modify existing preforms: coating of SAFFIL (Al<sub>2</sub>O<sub>3</sub>) fibers with CNTs**

In order to have a regular distribution of the CNTs for their infiltration by a molten metal, a 25 vol % alumina SAFFIL short fiber preform was used. It has been possible to let the CNTs grow on the short alumina fibers by placing the preform in the CVD reactor. To be precise, a certain amount of catalysts (Fe (III), Co (II)) was mixed with alumina fibers, which served as supports. The way to mix them is described as following. The powders of Fe (III) and Co (II) were mixed in distilled water. These mixtures were then introduced into the preform of 25 vol % SAFFIL fibers placed in a chemical tube (Fig. 2.9), drop by drop. The chemical tube with the preform was placed in oil. The oil has been heated up to 130 -150 °C for about 10 hours till the remaining mixture dried. After the evaporation, the chemical tube with the preform was seated in a furnace and the preform was dried at 120 °C for 1 hour. This preform of SAFFIL fibers with catalysts was placed in a quartz vessel, which was inserted in

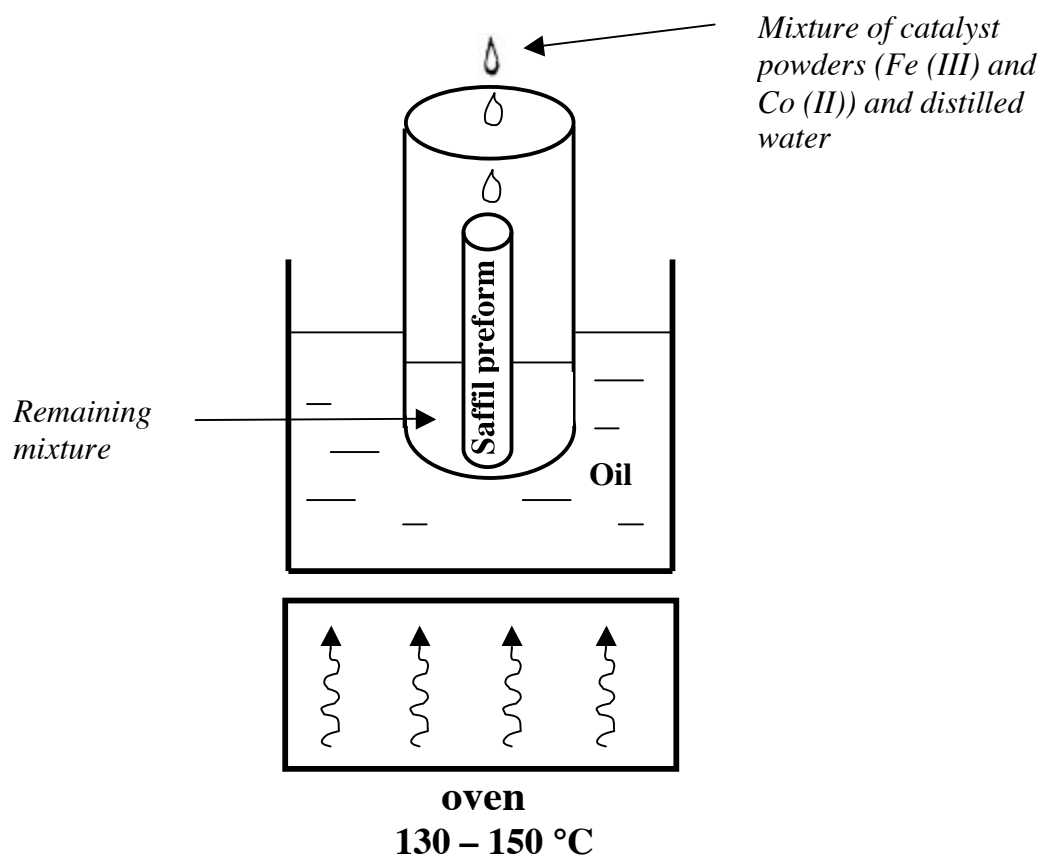


*Fig. 2.9: Method to introduce catalysts (Fe (III) and Co (II)) into a preform of 25 % vol SAFFIL fibers.*

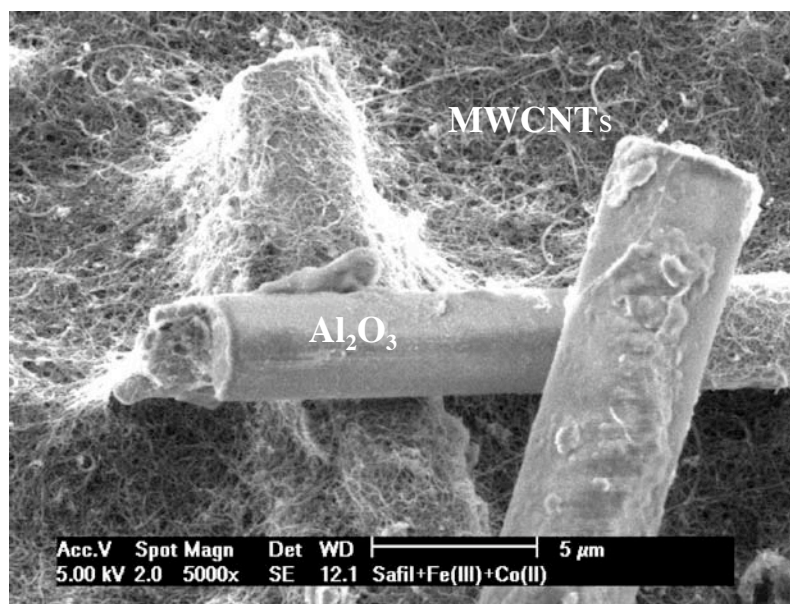


*Fig. 2.10: SEM image of SAFFIL fibers coated with MWCNTs.*

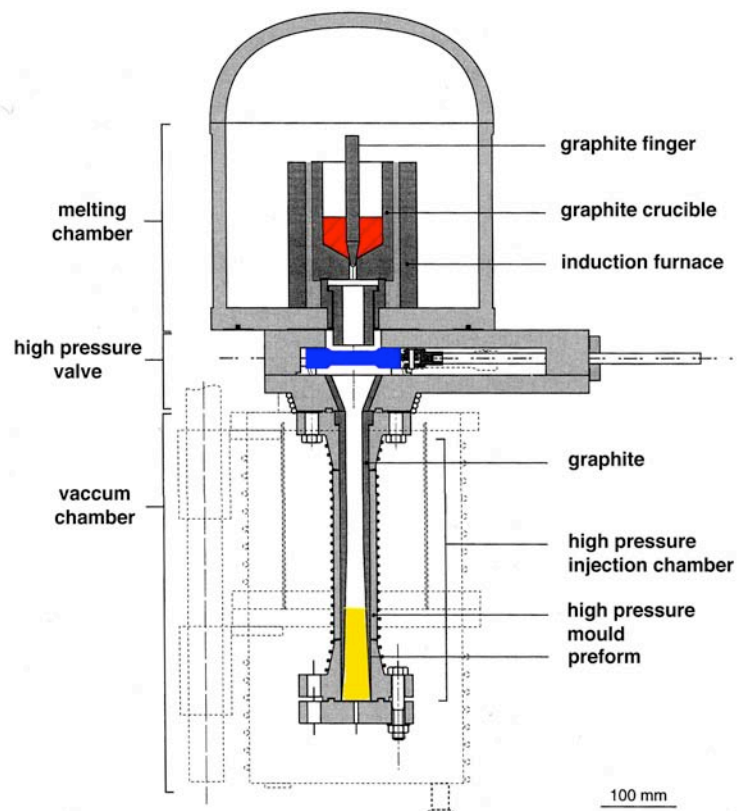
a quartz tube in the CVD reactor apparatus (as described in § 2.1.4). Keeping a flow of nitrogen (70 ml/min), a gas flow of acetylene (10 ml/min  $C_2H_2$ ) was introduced. The acetylene was decomposed and MWCNTs grew at the surfaces of the short alumina SAFFIL fibers at 720 °C. The entire procedure took 40 min per run. No purification of these products was performed. Fig.2.10 shows the scanning electron microscopy micrograph of these products. One can note that, between alumina SAFFIL fibers, the preform is full of carbon nanotubes.

## 2.5 MMCs processed by gas pressure infiltration

In this work, MWCNTs - based composites were also synthesized in a gas pressure infiltration device (Fig. 2.11) [84], which allows one to infiltrate ceramic preforms with molten metals or their alloys. The preforms were made of 25 vol % alumina short SAFFIL fibers or 25 vol % alumina short SAFFIL fibers coated with MWCNTs by CVD, whereas the metal or alloys used were pure magnesium or aluminium alloys (Al-4%Cu-1%Mg-0.5%Ag (WFA)). Both preforms and the metals or their alloys were preheated at 720 °C in vacuum ( $10^{-2}$  mbar) (Fig. 2.12). A pressure of 2 MPa was applied during infiltration. Then the composites were rapidly cooled down by air circulation. WFA-25vol%SAFFIL-CNTs, WFA-25vol%SAFFIL, Mg-25vol%SAFFIL-CNTs, Mg-25vol%SAFFIL composites were obtained in this method. Fig.2.13 and 2.14 show the microstructures of the composites. SAFFIL fibers are well embedded in the Mg or Al alloy matrix. However, the technique did not allow us to observe CNTs. Plate shaped specimens of dimensions  $1 \times 4 \times 50$  mm (effective length is 40 mm) were obtained by electro-spark machining for internal friction measurements.



(a)



(b)

**Fig. 2.11:** View and Schematic diagram of the gas pressure infiltration device consisting in principle of melting chamber, high pressure valve and vacuum chamber. The high pressure valve allows one to isolate the melting chamber from the injection chamber which is located inside the vacuum chamber.

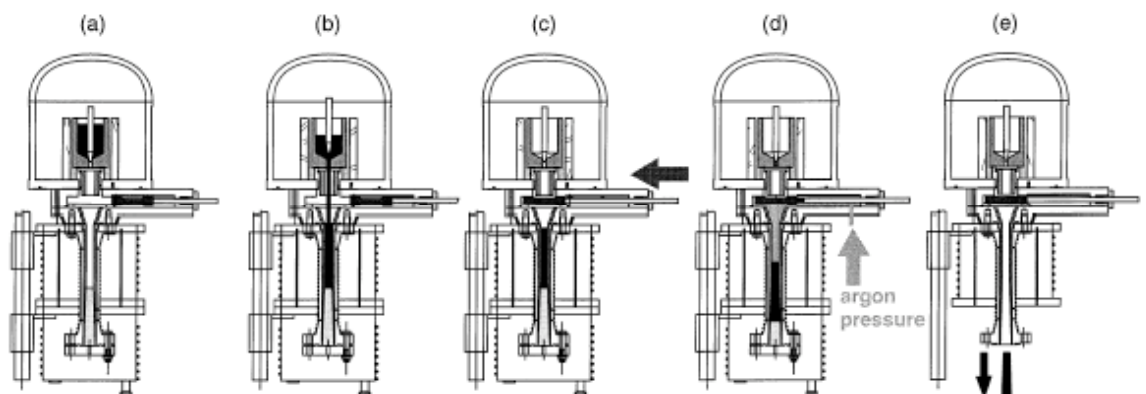


**Fig. 2.12:** Operation in the gas pressure infiltration device: (a) melting, (b) casting, (c) gate valve closing, (e) de - moulding.

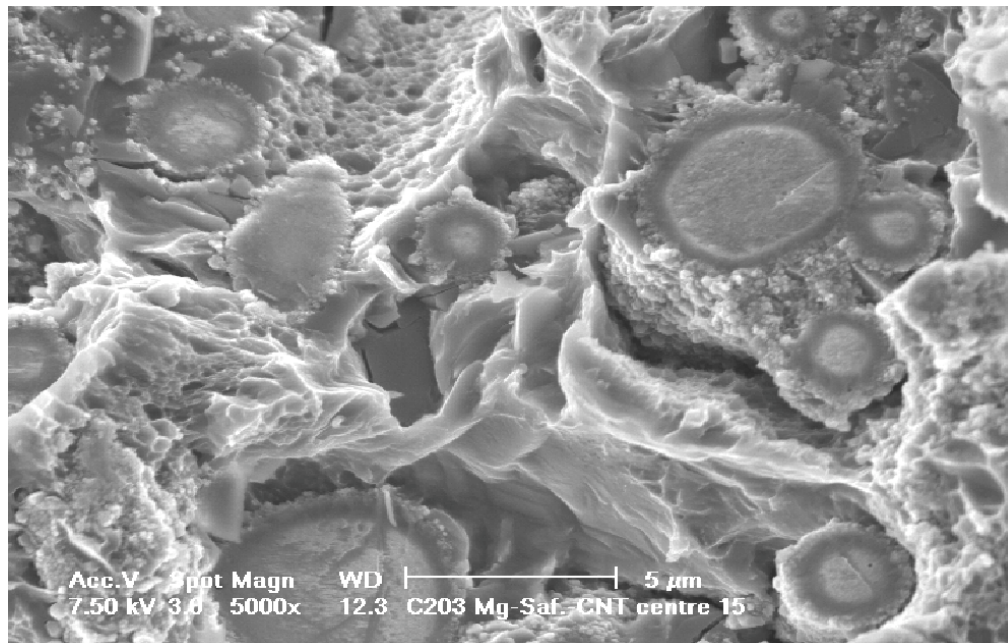


*Fig. 2.13: SEM image of fracture surface of Mg-25%SAFFIL-CNTs.*

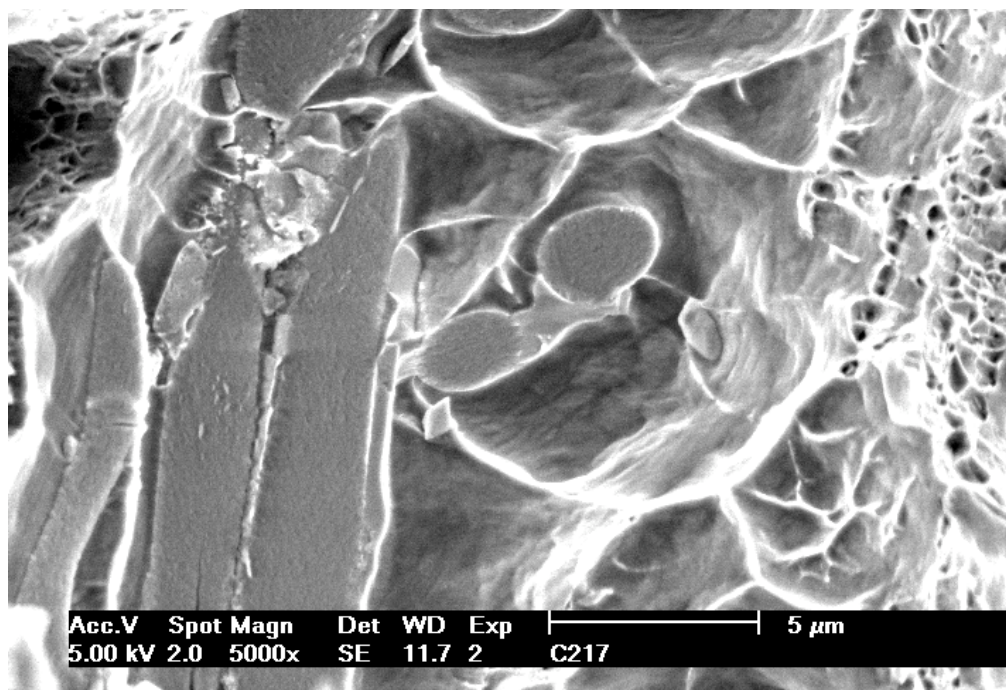


*Fig. 2.14: SEM image of fracture surface of (Al-4%Cu-1%Mg-0.5%Ag)-25%SAFFIL-CNTs.*



# Chapter 3

## Experimental techniques

---

### 3.1 Scanning Electron Microscope

The scanning electron microscope (SEM) is an instrument for studying the surface of materials using an electron beam. The large depth of focus, the excellent contrast and the straightforward preparation of solid specimens are the reasons for considerable success and widespread use of scanning electron microscopy in surface imaging over the last decades. This instrument differs from all other conventional microscopes, using light or electrons, in forming its image progressively, instead of all at once.

The principle of SEM and diagram of the electron probe formation in SEM are illustrated in Fig.3.1. Electrons from an electron gun are accelerated by a voltage of 1-50 kV between the electron gun and anode. A very fine electron beam, serving as an electron probe, with energies up to 30 keV, is obtained by a condenser lens system and finally focused on the surface of the specimen. This electron beam scans the surface of the specimen in a pattern of parallel lines using a scan generator. Under the electron impact, a series of elementary atomic interaction processes, elastic and inelastic scattering, take place, although the final signal used for image formation is, with only a few exceptions, not the result of single scattering processes but of the complete electron diffusion caused by the gradual loss of the electron energy and by lateral spreading due to multiple elastic large-angle scattering [85]. The main processes are the emission of secondary electrons (SE), the re-emission or reflection of high

energy backscattered electrons from the primary beam, the emission of X-rays or Auger electrons. The secondary electrons are originated from specimen atoms by collision with high energy electrons, which are the primary electrons entering the specimen or by backscattered electrons on their way out of it. X-ray emission occurs when an electron from upper shell fills the vacancy in the ionized shell. The energy of the x-ray may be transferred to another electron, which leaves the specimen as an Auger electron. However, the most important imaging modes of scanning electron microscopy are the secondary electrons (with energies of a few tens of eV) and backscattered electrons. The intensity of emission of both secondary electrons and backscattered electrons is very sensitive to the angle at which the electron beam strikes the surface, i.e. to topographical features on the specimen. The emitted electron current

### Scanning Electron Microscope

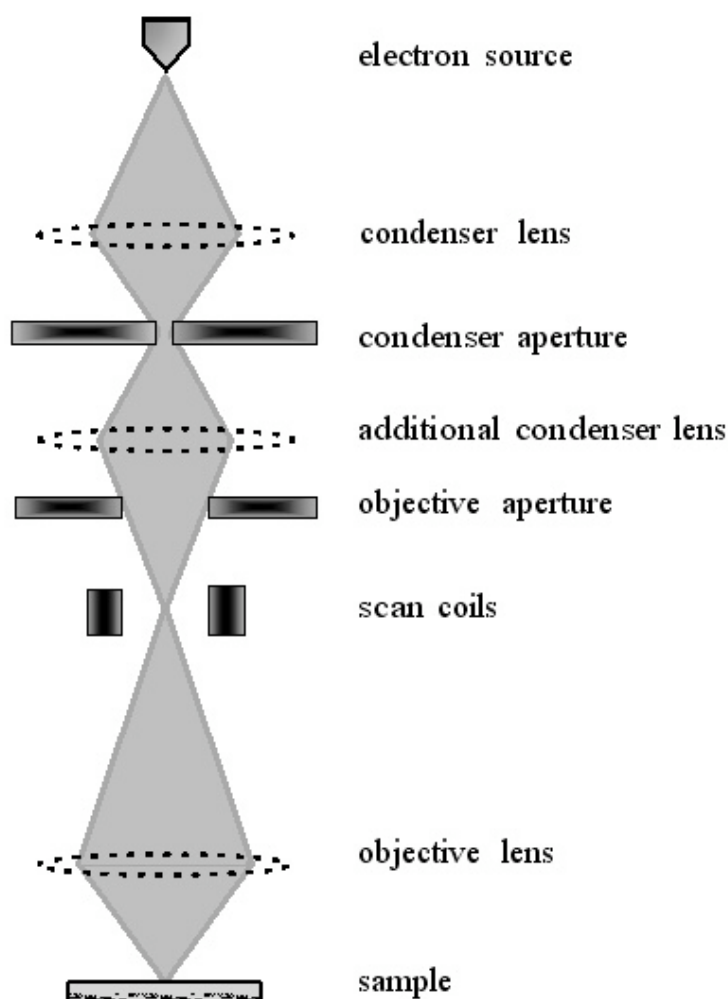


*Fig. 3.1: Electron path in scanning electron microscope.*

is collected and amplified before it is sent to a computer. Variations in the resulting signal strength as the electron probe scans across the specimen surface are used to vary the intensity of a corresponding spot of a raster image synchronous with the probe. A standard scanning electron microscope can reach a resolution of less than 10 nm.

In this work, a Philips XL 30 microscope equipped with a field emission gun (FEG) was used. SEM images of the specimens were obtained using secondary electron image mode. The used acceleration voltages were between 2 and 15 kV, and the typical working distance was 11 mm.

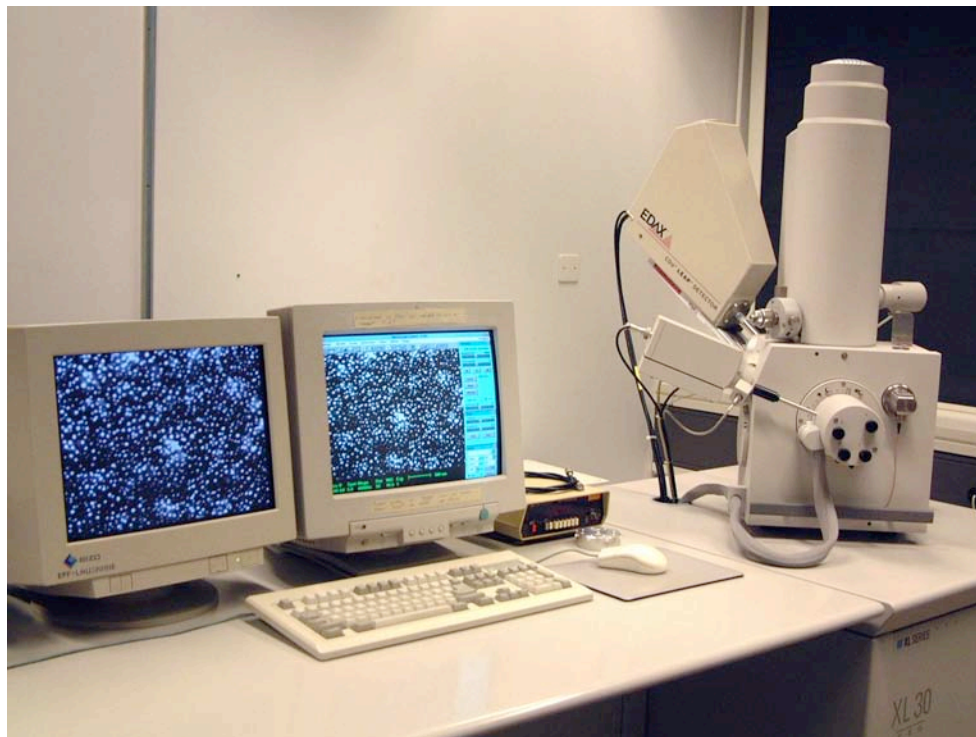


*Fig. 3.2: Philips XL 30 microscope.*

## 3.2 Mechanical spectroscopy

Internal friction ( $IF$ ), also called mechanical loss, is an important parameter to characterize the mechanical properties of a material. It measures the capacity of the material to convert its mechanical energy into heat, due to the anelasticity of the material

$$IF = \frac{1}{2\pi} \cdot \frac{\Delta W}{W} \quad (3.1)$$

where  $\Delta W$  is the energy, which is dissipated in the form of heat in the material per unit volume during a cycle of vibration, and  $W$  the maximum stored elastic energy, respectively.

Anelasticity is a kind of deformation behavior, which can be observed in a real solid. When a sample is subjected to an applied stress lower than its yield stress level, the total deformation of the sample can be divided into two components, elastic and anelastic. Both elastic strain and anelastic strain exhibit a linear relation with the applied stress. However, the elastic deformation (strain) responses instantaneously, whereas the anelastic response strain achieves its equilibrium value only after a period of time, named relaxation time  $\tau$ . When the applied stress is unloaded, the strain vanishes completely and instantaneously in the case of elastic strain but with the relaxation time  $\tau$  in the case of the anelastic strain.

From a microscopic point of view, the anelastic deformation can be interpreted by the reversible movement of structural defects such as point defects, dislocations and grain boundaries around their equilibrium position. Then the relaxation time is correlated to the passage of which an internal variable, which describes the motion of the structural defects, for example, the displacement of a dislocation, relaxes towards its equilibrium. Anelastic relaxation is an evolution of the material towards equilibrium with a modification of the internal variable towards a new equilibrium value. During this evolution, a dissipation of energy results from the motion of the defects.

This dissipated energy can be measured, in practice, by dynamic methods. When a cyclic stress

$$\sigma = \sigma_0 e^{i\omega t} \quad (3.2)$$

where  $\sigma_0$  and  $\omega$  are the amplitude and the circular frequency of the applied stress, respectively, is applied to a sample, the linearity of the relationship between the stress and the strain ensures that the response strain is also periodic with the same frequency

$$\varepsilon = J^* \sigma = \varepsilon_1 - i\varepsilon_2 \quad (3.3)$$

where

$$J^* = J_1 - iJ_2 \quad (3.4)$$

is the complex dynamic elastic compliance. Its reciprocal

$$G^* = \frac{1}{J^*} = G_1 - iG_2 \quad (3.5)$$

is the complex dynamic elastic modulus. Then

$$\varepsilon = \varepsilon_0 e^{i(\omega t - \phi)} \quad (3.6)$$

where  $\varepsilon_0$  is the amplitude of the strain and  $\phi$  the phase lag between  $\sigma$  and  $\varepsilon$ , called mechanical loss angle, due to the anelasticity of the material. Therefore the mechanical loss can be obtained

$$\tan \phi = \frac{J_2}{J_1} = \frac{G_2}{G_1} \quad (3.7)$$

The dissipated energy  $\Delta W$  during one cycle of vibration per unit volume and the maximum stored elastic energy  $W$  per unit volume are, respectively

$$\Delta W = \oint \sigma(t) d\varepsilon(t) = \pi J_2 \sigma_0^2 \quad (3.8)$$

and

$$W = \int_0^{\varepsilon_0} \sigma(t) d\varepsilon_1(t) = \frac{1}{2} J_1 \sigma_0^2 \quad (3.9)$$

By considering these two terms in equation (3.1), one can obtain

$$IF = \tan \phi \quad (3.10)$$

### 3.2.1 Standard anelastic solid and Debye relaxation

Phenomenologically, the standard anelastic solid can be approached by a rheological model. Fig. 3.3 shows that such a model may consist in a spring (1) and a *Voigt unit* (involving a spring (2) and a dashpot (3) in parallel) in series. This section describes how all the characteristics of an anelastic material can approximately be presented by this three parameter model.

When applying a stress abruptly, the spring (1) with compliance  $J_U$  deforms instantaneously, whereas the *Voigt unit* remains undeformed due to the dashpot. With time, the piston moves in the dashpot (with viscosity  $\eta$ ) viscously until the stress on the dashpot is completely transferred to the spring (2). Fig. 3.4 presents the applied stress  $\sigma$  and the response strain  $\varepsilon$ . The compliance of the whole system evolves from the initial equilibrium value  $J_U$  (unrelaxed compliance) to the final equilibrium value  $J_R$  (relaxed compliance). Apparently, the elastic and anelastic behavior are represented by the spring (1) and the *Voigt unit*, respectively. Moreover, one can easily see that the compliance of the spring (2) is given by  $\delta J = J_R - J_U$ . The viscosity  $\eta$  of the dashpot is associated to the relaxation time  $\tau$  and can be expressed by  $\eta = \tau / \delta J$ . The anelastic equation of the standard anelastic solid can be written as [86, 87]:

$$\varepsilon + \tau \dot{\varepsilon} = J_R \sigma + \tau J_U \dot{\sigma} \quad (3.11)$$

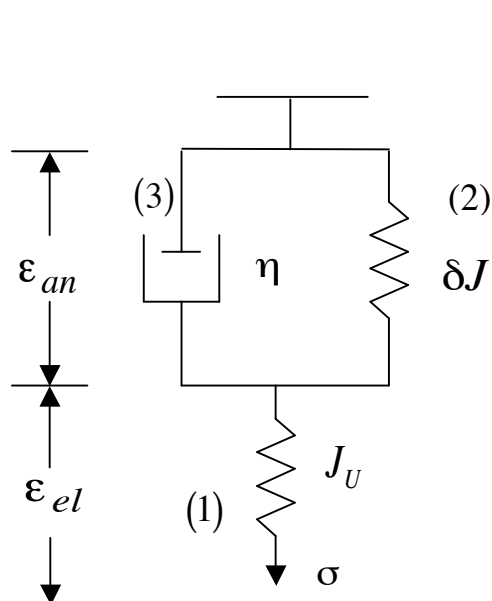


**Fig. 3.3:** Three - parameter model of standard anelastic solid.

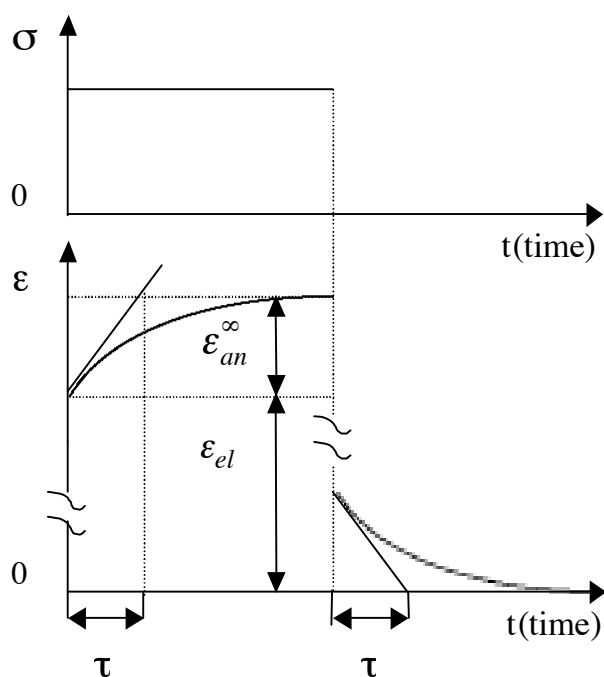


**Fig. 3.4:** The stress  $\sigma$  applied to the three-parameter model of a standard anelastic solid and the response strain  $\epsilon$ .

In the case of using a cyclic applied stress, the solution can be obtained by substituting equations (3.2) and (3.6) into equation (3.11)

$$\epsilon = \left( J_U + \frac{\delta J}{1 + \omega^2 \tau^2} \right) \sigma - i \delta J \frac{\omega \tau}{1 + \omega^2 \tau^2} \sigma \quad (3.12)$$

or

$$\epsilon = J_1 \sigma - i J_2 \sigma \quad (3.13)$$

where

$$J_1 = J_U + \frac{\delta J}{1 + \omega^2 \tau^2} \quad (3.14)$$

$$J_2 = \delta J \frac{\omega \tau}{1 + \omega^2 \tau^2} \quad (3.15)$$

Assuming  $\delta J \ll J_U$ , the mechanical loss can be computed

$$IF = \tan \phi = \frac{J_2}{J_1} = \Delta \frac{\omega \tau}{1 + \omega^2 \tau^2} \quad (3.16)$$

where  $\Delta = \delta J / J_U$  is called relaxation strength.

The variation of dynamic compliance (also called modulus defect) can be obtained

$$\frac{\delta J(\omega)}{J_U} = \frac{J_1 - J_U}{J_U} = \Delta \frac{1}{1 + \omega^2 \tau^2} \quad (3.17)$$

The equation (3.16) shows a maximum of mechanical loss at  $\omega \tau = 1$ , corresponding to a symmetrical peak about  $\log(\omega \tau) = 0$  (Fig. 3.5). Such a peak is usually called Debye peak, with the height  $\Delta/2$  and width  $\Delta(\log \omega \tau) = 1.144$  (at half maximum). In response to this peak, the function of variation of dynamic compliance (equation (3.17)) exhibits a “drop” in the vicinity of  $\log(\omega \tau) = 0$  (Fig. 3.5).

A Debye peak reflects a relaxation mechanism, which is associated with the reversible motion of structural defects such as point defects, dislocations or grain boundaries. In practice, an observed peak may be more complicated: asymmetrical and broader than Debye peak. Such a peak may involve a more complex or multi relaxation mechanism (see §3.2.3).



One can study the relaxation mechanism of a material by analyzing the features of a peak in a spectrum.

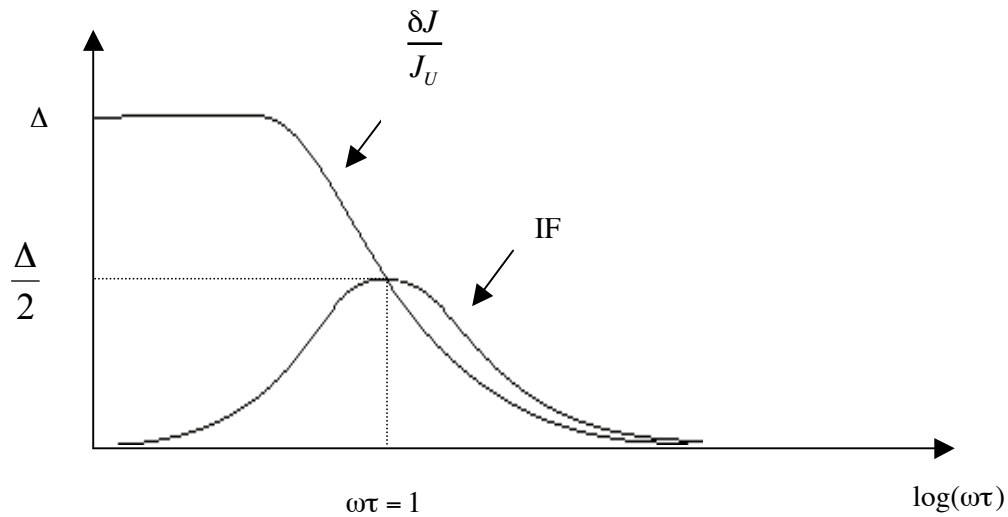


*Fig. 3.5: Debye peak and associated variation of the modulus.*

When the process of relaxation is thermally activated, the relaxation time depends on temperature (Arrhenius law)

$$\tau = \tau_0 e^{\frac{H}{kT}} \quad (3.18)$$

where  $\tau_0$  is the limit relaxation time,  $H$  the activation enthalpy of the phenomenon and  $k$  the Boltzmann constant.

Thus the maximum of a Debye peak can be obtained for:

$$\omega\tau = \omega\tau_0 e^{\frac{H}{kT_p}} = 1 \quad (3.19)$$

where  $T_p$  is the peak temperature.

Equation (3.19) can be written as

$$\ln(\omega\tau_0) + \frac{H}{kT_p} = 0 \quad (3.20)$$

or

$$\ln \omega = \ln(\tau_0^{-1}) - \frac{H}{kT_p} \quad (3.21)$$

from which the activation enthalpy  $H$  can be experimentally derived easily. Experimentally, one usually measures the peak temperature at different excitation frequency and then plot  $\ln \omega$  versus  $1/T_p$  (Arrhenius graph). The value of enthalpy  $H$  can be obtained from the slope of the obtained line while the value of  $\tau_0$  is given by the intercept at  $\ln \omega$  axis. However, when the spectrum is composed of a bad-resolved peak on an exponential background, decomposition of the peak from the background will be difficult. In this case, the activation parameters can be estimated by master curve methods.

### 3.2.2 Master curve method

The so-called master curve is formed by a superimposition of isothermal mechanical loss spectra measured as a function of frequency ( $f$ ) for different temperatures. If these spectra may be brought into coincidence by a shift along the  $\log(f)$  axis, the mechanical loss is assumed to be a function of only the product  $\omega\tau$  [88, 89]:

$$\tan(\phi) = \tan(\phi[\log(\omega\tau)]) = \tan(\phi[\log(f) + \log(2\pi\tau_0) + \frac{H}{kT \ln(10)}]) \quad (3.22)$$

Bringing into coincidence the isothermal spectra means that  $\tan(\phi)$  remains constant by a shift. Thus the variation of  $\tan(\phi)$  must be zero or

$$\delta\left[\log(f) + \frac{H}{kT \ln(10)} + \log(2\pi\tau_0)\right] = 0 \quad (3.23)$$

Then

$$\delta(\log(f)) = -\frac{H}{k \ln(10)} \cdot \delta\left(\frac{1}{T}\right) \quad (3.24)$$

Plotting the line  $\delta(\log(f))$  versus  $\delta(1/T)$ , the activation enthalpy  $H$  can be calculated from the slope of the line.

### 3.2.3 Multiple relaxations

#### 3.2.3.1 Discrete spectra

A discrete spectrum of relaxation processes is a superposition of  $n$  Debye peaks with discrete values of the characteristic parameters of each peak. More precisely, when there are  $n$  internal variables that are relaxed simultaneously, with a single relaxation time for each of them, the dynamic response functions become

$$J_1 = J_U + \sum_{i=1}^n \frac{\delta J^{(i)}}{1 + [\omega\tau^{(i)}]^2} \quad (3.25)$$

$$J_2 = \sum_{i=1}^n \delta J^{(i)} \frac{\omega\tau^{(i)}}{1 + [\omega\tau^{(i)}]^2} \quad (3.26)$$

Then the internal friction and the modulus defect can be expressed by

$$\tan \phi = \frac{J_2}{J_1} = \sum_{i=1}^n \Delta^{(i)} \frac{\omega \tau^{(i)}}{1 + [\omega \tau^{(i)}]^2} \quad (3.27)$$

$$\frac{\Delta J}{J_U} = \frac{J_1(\omega) - J_U}{J_U} = \sum_{i=1}^n \Delta^{(i)} \frac{1}{1 + [\omega \tau^{(i)}]^2} \quad (3.28)$$

This means that the whole relaxation spectrum is composed by the superposition of  $n$  independent lines. Each of them is characterised by its own relaxation time  $\tau^{(i)}$ .

### 3.2.3.2 Continuous spectra

An experimental relaxation peak, much broader than a Debye peak and sometimes with an asymmetrical shape, is often observed, even though this peak is controlled by only one mechanism. In this case, the relaxation of one internal variable is considered as a continuous distribution (instead of a unique value) of relaxation times  $\tau$ . This situation corresponds, for instance, to the motion of dislocations in a multi-well energy diagram dependent on the length of the dislocations and the local internal stresses [90]. From the Arrhenius relation, one can see that the continuous distribution in  $\tau$  may originate from a continuous distribution in activation enthalpy  $H$  and/or in the pre-exponential factor  $\tau_0$ . Nowick and Berry [86] considered the case in which the variable  $z = \ln(\tau/\tau_m)$  obeys a Gaussian distribution with variable  $\beta$ , a measure of the width of the Gaussian distribution.  $\tau_m$  is the mean relaxation time. With the normalised relaxation function

$$\Lambda(z) = \frac{1}{\beta \cdot \pi^{1/2}} \exp\left[-(z/\beta)^2\right] \quad (3.29)$$

the dynamic response functions  $J(\omega)$  become

$$J_1(x) = J_U + \frac{\delta J}{\beta \cdot \pi^{1/2}} \cdot \int_{-\infty}^{+\infty} \frac{\exp\left[-(z/\beta)^2\right]}{1 + \exp\left[2 \cdot (x + z)\right]} dz = J_U + \delta J \cdot f_1(x, \beta) \quad (3.30)$$

$$J_2(x) = \frac{\delta J}{2 \cdot \beta \cdot \pi^{1/2}} \int_{-\infty}^{+\infty} \exp\left[-(z/\beta)^2\right] \cdot \cosh^{-1}(x+z) \cdot dz = \delta J \cdot f_2(x, \beta) \quad (3.31)$$

where

$$x = \ln(\omega \tau_m) \quad (3.32)$$

Then the internal friction and the elastic modulus defect can be written as

$$\tan \phi(x) = \frac{J_2(x)}{J_U} = \frac{\delta J}{J_U} \cdot f_2(x, \beta) \quad (3.33)$$

$$\frac{\Delta J}{J_U} = \frac{J_1(x) - J_U}{J_U} = \frac{\delta J}{J_U} \cdot f_1(x, \beta) \quad (3.34)$$

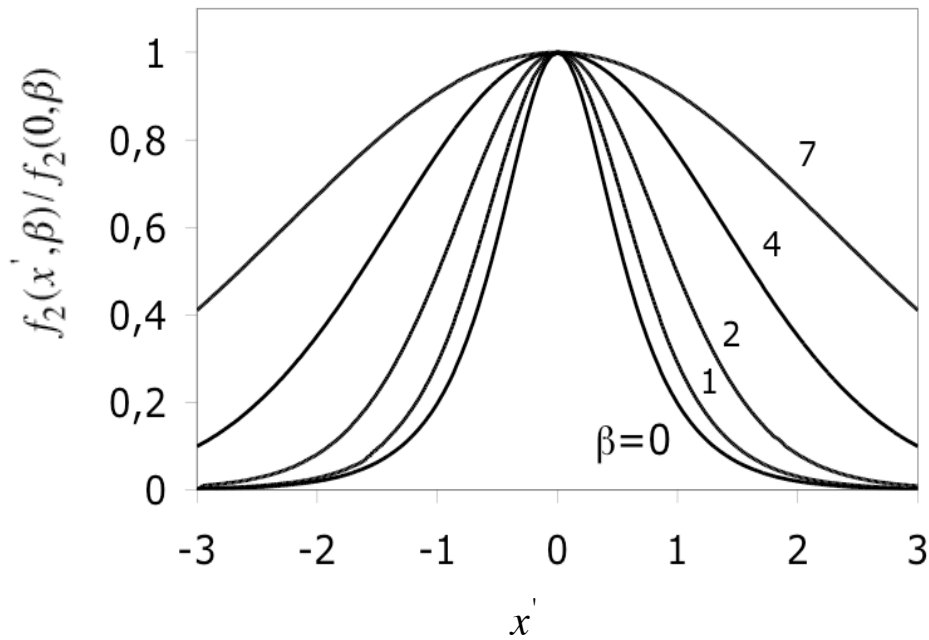


**Fig. 3.6:** Normalized distribution functions  $f_2(x', \beta) / f_2(0, \beta)$  versus the variable  $x' = \log(\omega \tau_m)$  for different values of the  $\beta$  parameter.

The function  $f_2(x', \beta)$  versus the variable  $x' = \log(\omega\tau_m)$  is plotted in Fig.3.6. The case of  $\beta = 0$  corresponds to the linear standard anelastic solid. This means the peak is a Debye peak.

### 3.2.4 Relaxation mechanisms

#### 3.2.4.1 Granato model [91]

Fig. 3.7 shows a dislocation segment with length  $l$  which bows between two pinning points in a manner analogous to a stretched string. When the applied stress  $\sigma$  is alternative, this dislocation segment may vibrate around its equilibrium position with mean displacement  $u$ .

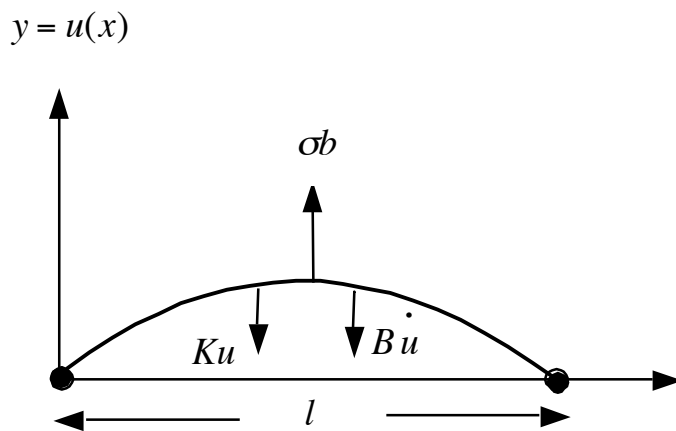


**Fig. 3.7:** Dislocation string model

In this model, the restoring force  $Ku$ , opposite to  $\sigma$ , is due to the line tension  $\gamma$  of the dislocation segment. The viscous friction or dragging term  $B\dot{u}$ , acting in the same direction as  $Ku$ , is generated from a couple of different sources such as point defect dragging, kink pair formation and impurities or other inclusions on the dislocation loop. The motion equation of this dislocation segment and the total strain are given by [92]

$$B\dot{u} + Ku = b\sigma \quad \text{with} \quad K = \frac{12\gamma}{l^2}, \quad B = \frac{kT}{lD} \quad (3.35)$$

$$\varepsilon = J_U \sigma + \Lambda b u \quad (3.36)$$

where  $b$  is the Burgers vector of the dislocation,  $\Lambda$  the density of the mobile dislocation,  $k$  the Boltzmann constant,  $D$  the diffusion coefficient. From equations (3.11) and (3.16), the internal friction can be deduced

$$\tan \phi = \frac{\Lambda b^2}{J_U} \cdot \frac{\omega B}{K^2 + \omega^2 B^2} = \Delta \frac{\omega \tau}{1 + \omega^2 \tau^2} \quad (3.37)$$

$$\frac{\delta J}{J_U} = \Delta \frac{1}{1 + \omega^2 \tau^2} \quad (3.38)$$

with

$$\Delta = \frac{\Lambda b^2}{K J_U} \quad (3.39)$$

and

$$\tau = \frac{B}{K} = \frac{B l^2}{12 \gamma} \quad (3.40)$$

Considering the relation between the line tension  $\gamma$  and the shear modulus  $\mu$  or compliance  $J_U$

$$\gamma = \frac{\mu b^2}{2} = \frac{b^2}{2 J_U} \quad (3.41)$$

(3.39) can be written as

$$\Delta = \frac{\Lambda l^2}{6} \quad (3.42)$$

then equation (3.37) becomes

$$\tan \phi = \frac{\Lambda l^2}{6} \cdot \frac{\omega \tau}{1 + \omega^2 \tau^2} \quad (3.43)$$

### 3.2.4.2 The effect of the variation of the pinned dislocation segment length

The expression of the restoring force (Eq. 3.35) shows that the restoring force is very sensitive to the length of the pinned dislocation loop due to the power of 2 in the  $l$  term. When the length increases, the restoring force decreases rapidly. The pinning points on the dislocation lines can be solute atoms, precipitates or impurities. The variation of the length of pinned dislocation segment may result from statistical jumps of the solute atoms, acting previously as pinning points on the dislocation loop, from one equilibrium state to another under thermal activation. The initial distance between the pinning points is assumed to be  $l_0$ . In a simplified model, Schaller [93] assumes that due to the thermally activated jumps, the length increases from  $l_0$  to  $l$  proportionally to the diffusion coefficient  $D$

$$l = l_0(1 + \alpha D) \quad (3.44)$$

with  $\alpha$  a coefficient of efficiency.

Accordingly, the restoring force weakens because the restoring coefficient  $K$  decreases when  $l$  increases

$$K = \frac{12\gamma}{l_0^2(1 + \alpha D)^2} \quad (3.45)$$

This modifies  $\tau$  and  $\Lambda$  in equation (3.40) and (3.39)

$$\tau = \frac{B}{12\gamma} [l_0(1 + \alpha D)]^2 \quad (3.46)$$



$$\Delta = \frac{\Lambda b^2}{12J_U \gamma} l_0 (1 + \alpha D)^2 \quad (3.47)$$

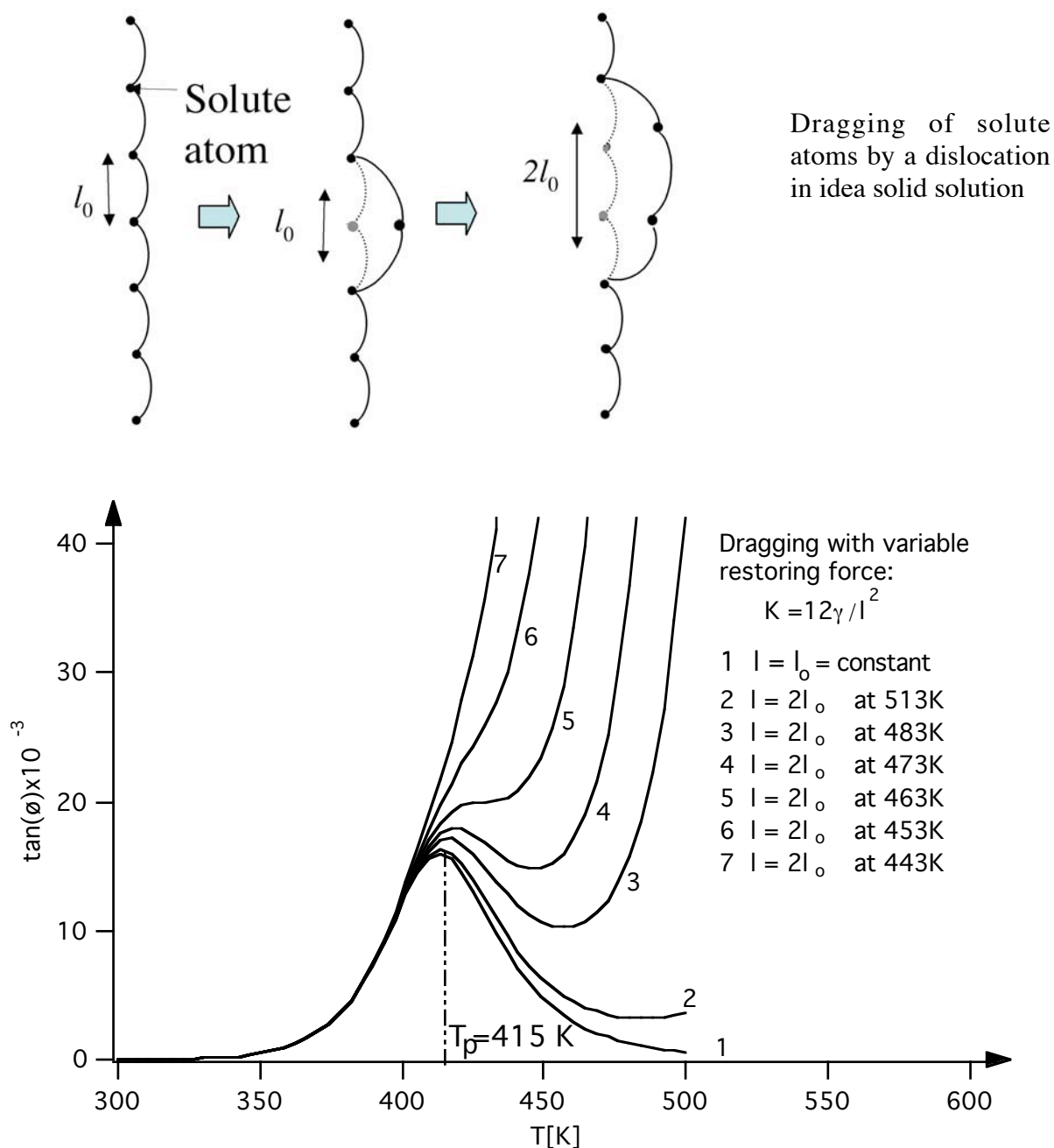


**Fig. 3.8:** Mechanical loss spectra due to the dragging of solute atoms by a dislocation in idea solid solution. Curve 1 corresponds to the constant restoring force. Whereas curves 2 to 7 are associated to the decrease in restoring force resulted from the increase in temperature.

These modified parameters  $\tau$  and  $\Delta$  gives rise to a modification of the internal friction spectrum. In other words, the configuration of the spectrum such as the peak appearance and the exponential increase changes with restoring force, which depends on the efficiency of the pinning points and the atom diffusivity [93]. Fig 3.8 presents different configurations of curves resulting from weakening the restoring force ( $K$ ), due to the jump of one atom at different temperatures. In this case, the peak can be measured with respect to the background. In some cases, this model still has difficulty to reach the agreement with the experimental results. In order to give a more realistic value of internal friction, Granato and Lücke's assure that pinning points are distributed randomly along the dislocation line. Moreover, the dislocation loop lengths between the pinning points obey an exponential distribution

$$N(l)dl = \frac{\Lambda}{l_N^2} \exp\left(-\frac{l}{l_N}\right) dl \quad (3.48)$$

where  $l_N$  is the average distance between the pinning points.

### 3.2.4.3 Dislocation motion in solid solution: pinning-depinning

Now let's consider dislocation motion in a field of point defects distributed on the dislocation glide plane. In Schaller's model, the length of the dislocation loop between pinning points can be increased by thermally activated jumps of the solute atoms. If the pinning points are not mobile, under the effect of a cyclic shear stress, the segments of dislocation loop bow reversibly. When the applied cyclic stress is greater than the critical stress for breakaway, dislocation segment breaks away first from one point defect (a pinning point). Then the whole segment is torn away from the rest of the pinning points on the segment, leading to higher vibrating amplitude of the dislocation line (Fig. 3.9(a)). Moreover, after the breakaway from the previous pinning points, the dislocation segment moves further in its glide plane and is pinned by the next point defects (Fig. 3.9 (b)). In this way, the dislocation segment migrates in the point defect cloud distributed in its glide plane by pinning - depinning.

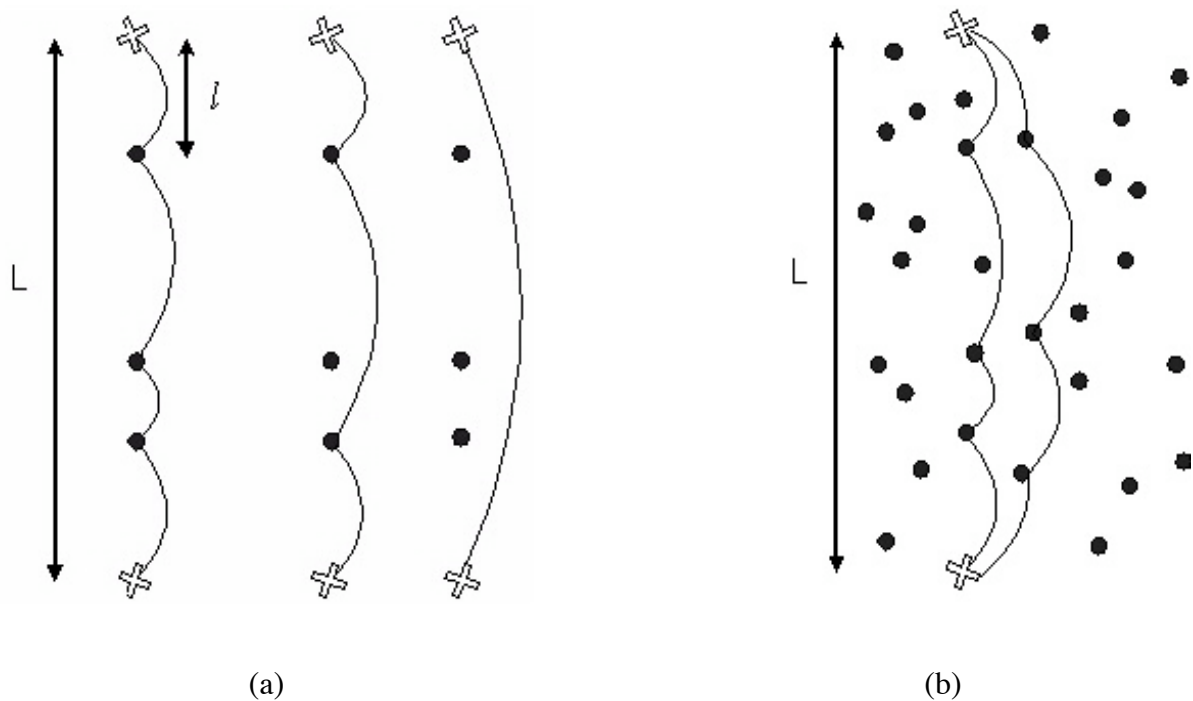


**Fig. 3.9:** Schematic illustration of the mechanism of (a) the breakaway of a dislocation segment of length  $L$  and (b) the motion by pinning - depinning of the dislocation segment through immobile point defects distributed in the dislocation glide plane.

#### 3.2.4.4 Hysteretic dislocation damping background in solid solution

Schaller's model and Koehler theory [94], which take into account only the short-range dislocation-point defects interaction, can describe and explain the peak of internal friction spectrum (relaxation peak) with respect to the background. However, they encounter difficulties in interpreting the damping background. In fact, in addition to the short-range interaction, a long-range interaction between dislocations and point defects also takes place in a solid solution. In short-range dislocation-point defects interaction, the point defects, acting as short-range obstacles, which can be overcome under the effect of the applied stress and thermal energy activation, interact with dislocation core. In long-range interaction, the point defects are situated in the bulk, on the two sides of the glide plane of the dislocation, as well as on the glide plane of dislocations but far away from the dislocation lines. These point defects generate relatively weak long-range elastic fields, resulting from their various elastic effects such as size effect, modulus effect and anisotropic effect [95]. Such type of point

defect obstacles can be overcome by an applied stress athermally, leading to an athermal hysteretic damping background in solid solution. According to this theory, Gremaud [95] developed a model, which allows one to predict a complex multi-component behaviour of the nonlinear internal friction in details, especially to analyse all the characteristic behaviour of the athermal hysteretic damping background as well as the peaking and pinning effect during irradiation, associated to dislocation-point defects interaction in solid solution.

Gremaud's theory, offering a rather precise method to study the internal friction due to dislocation-point defects interaction, involves complicated calculations. In order to simplify the calculations, an approximate model was proposed by Benoit [92], based on the fact that in the low frequency range, the damping is frequency independent. It was assumed that the friction exerted on the dislocation loop consists of two components: a viscous friction  $B\dot{u}$  and a frequency independent friction term  $Cu$ . Then the motion equation of the dislocation loop can be written as

$$i(\omega B + C)u + Ku = \sigma b \quad (3.49)$$

and the mechanical loss is given by

$$\tan \phi = \frac{\Lambda b^2}{KJ_U} \cdot \frac{\left(\frac{\omega B + C}{K}\right)}{1 + \left(\frac{\omega B + C}{K}\right)^2} \quad (3.50)$$

### 3.3 Forced torsion pendulum

Forced torsion pendulum was developed for analysing anelasticity with a sub-resonant method, which allows one to perform the measurements of internal friction and shear modulus (in arbitrary units) either over a wide temperature range by keeping frequency constant or as a function of frequency at a constant temperature. Fig.3.10 shows a forced torsion pendulum Guzla. The Schematic diagram of a forced torsion pendulum is displayed in Fig. 3.11. In this method, the specimen vibrates at a sub - resonant frequency, which is much lower than the

resonant frequency of the system. The plate shape specimen with dimensions  $1 \times 4 \times 50$  mm (effective length is 40 mm) is fixed at two ends by two grips. The lower grip is connected to a short rod, which is subsequently fixed at the bottom of a tube, which houses the pendulum. The upper grip is connected to a long extension rod, which is suspended either by three tungsten wires, or by a tungsten wire in tension. Through these tungsten wires, the weight of the upper grip and the extension rod is counterbalanced by a counterweight (pieces of metal), avoiding axial stress, which could lead to an axial creep of the specimen during heating.

The electrical excitation is performed by a magneto-electric system consisting of two Helmholtz coils and permanent magnet attached to the extension rod. The response strain is measured by a laser beam displacement recorded by a photo cell. More precisely, when a generator, which is incorporated in a commercial frequency response analyser (Schlumberger 1250FRA) (Fig. 3.12), produces a sinusoidal electrical signal (an electrical current) with a given frequency  $\omega$  and then this signal is magnified and sent to the Helmholtz coils, a magnetic force is generated and applied to the permanent magnet. As a consequence, a periodic torsion stress

$$\sigma = \sigma_0 \sin \omega t \quad (3.5)$$

is applied to the specimen, where  $\sigma_0$  is the amplitude of the stress,  $t$  the time. The response strain  $\varepsilon$

$$\varepsilon = \varepsilon_0 \sin(\omega t - \phi) \quad (3.6)$$

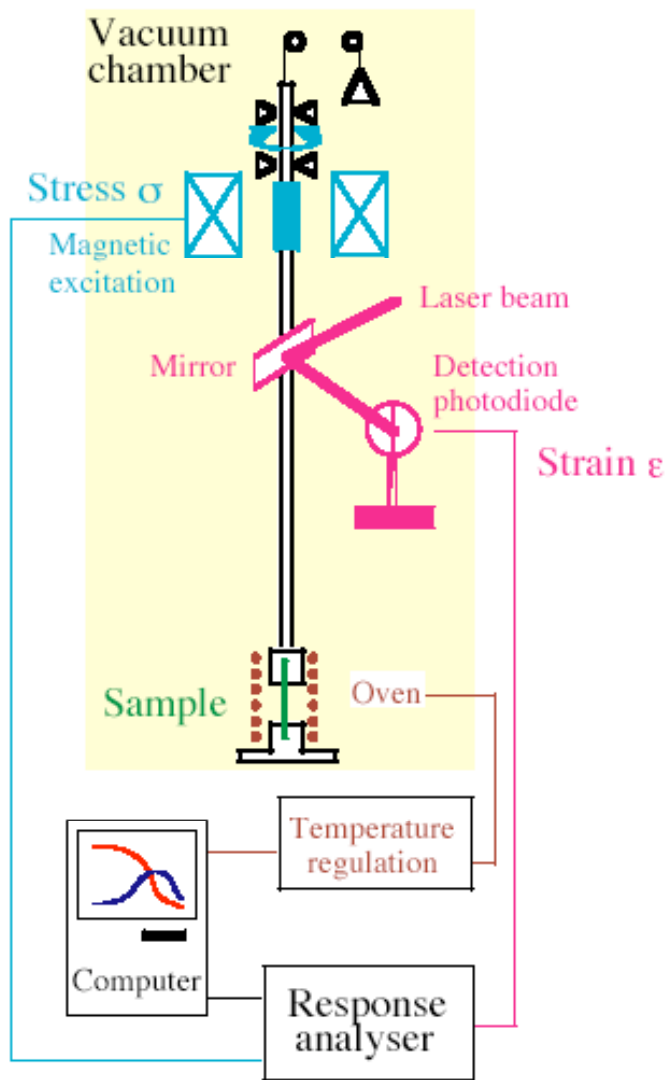
is obtained from the photocell. The frequency response analyser (Schlumberger 1250FRA) measures the phase lag  $\phi$  and the amplitude ratio of these two signals. Thus the internal friction  $IF$  and the shear modulus  $G$  are obtained as

$$IF = \tan(\phi) \quad (3.51)$$

and



**Fig. 3.10:** View of forced torsion pendulum  
Guzla.



**Forced pendulum**

Apply a cyclic stress  $\sigma = \sigma_0 \sin(\omega t)$   
 Measure the strain  $\epsilon = \epsilon_0 \sin(\omega t - \phi)$

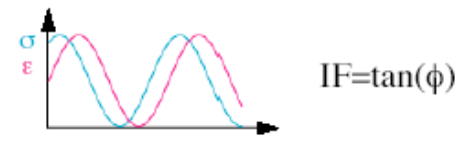


**Fig. 3.11:** Schematic diagram of forced torsion pendulum.



*Fig. 3.12: Electronic part of the Guzla forced torsion pendulum.*

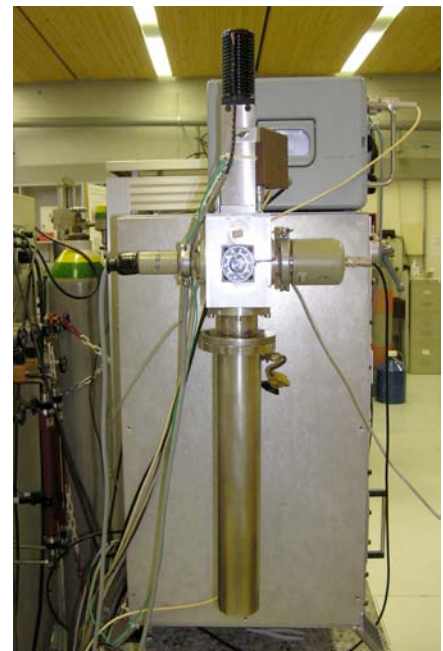
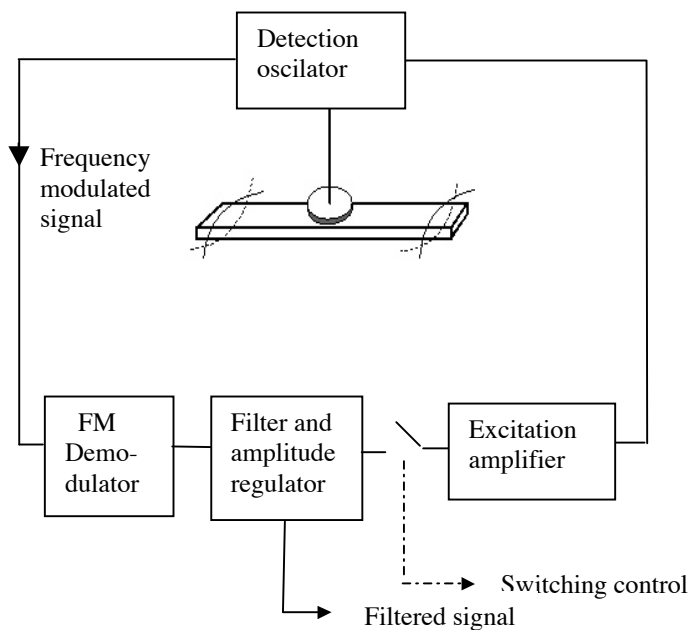
$$G = \frac{\sigma_0}{\epsilon_0} \quad (3.52)$$

During the measurement, the temperature of the specimen is controlled by a thermal system, which consists of a furnace surrounding the specimen, and a Eurotherm PID controller, permitting to vary the temperature of the specimen in a range of 70-800K. The whole system is installed on an anti-vibration frame, in order to prevent it from external mechanical vibration. The measurements are performed after pumping down to about  $10^{-5}$  mbar and then introducing 5 mbar pure He as a heat exchange gas. At the temperature lower than room temperature, liquid nitrogen is employed as refrigerant.

### 3.4 Free-free vibrating bar apparatus

The free-free vibrating bar apparatus (Fig. 3.13), named “Xylophone”, was used in this work to measure the sample’s internal friction and the resonant frequency from which the

Young's modulus of the sample can be deduced. A plate shape specimen with dimensions of  $1 \times 4 \times 40$  mm is held at two vibration nodes and excited by an electro-static force generated between the "excitation-detection" electrode and the vibrating specimen (Fig.3.13 (a)). The capacitance formed by the electrode and the specimen varies with the vibration of the specimen. The frequency modulated signal can be transferred by a FM demodulator into an output voltage proportional to the instantaneous deformation of the vibrating specimen by electronic part (Fig.3.14). This signal serves as excitation signal, which is applied between the "excitation-detection" electrode and the specimen. Consequently, the specimen is excited and vibrates at its resonant frequency



(a) Schematic diagram of free-free vibrating bar.

(b) Xylophone

**Fig. 3.13:** Free-free vibrating bar apparatus Xylophone II.





**Fig. 3.14:** *Electronic part of the Xylophone II vibrating bar apparatus.*

When switching off the excitation, the free-free vibrating bar becomes a free-decay mode. The internal friction of the vibrating specimen is measured by the logarithmic decrement:

$$Q^{-1} = \frac{1}{n\pi} \ln \frac{A_i}{A_{i+n}} \quad (3.53)$$

where  $A_i$  and  $A_{i+n}$  are the chosen amplitudes,  $n$  is the number of periods required to decrease the amplitude from  $A_i$  to  $A_{i+n}$ . The Young's modulus of the specimen can be calculated from the resonant frequency  $f$  of the vibrating specimen by

$$E = \frac{\rho \cdot l^4}{1.061 \cdot a^2} f^2 \text{ (Pa)} \quad (3.54)$$

where  $\rho$  is the density,  $a$  the thickness and  $l$  the length of the specimen.



## Chapter 4

# Experimental results and interpretations: Al alloys - or Mg - 25%SAFFIL - CNTs composites

---

### 4.1 Study of WFA (Al-4% Cu-1% Mg-0.5% Ag) -25%SAFFIL-CNTs composites

#### 4.1.1 Experimental results

##### 4.1.1.1 Mechanical properties

Table 4.1 shows that Young's modulus as measured by free-free bar apparatus for WFA-25%SAFFIL and for WFA-25%SAFFIL-CNTs are 65.5 GPa and 83.5 GPa, respectively. One can see that the addition of CNTs increases the Young's modulus by 27.5%. The specific modulus for both CNT-reinforced and CNT-free composites is the same. It is higher than that of steel. However, it was observed that both materials are brittle with a low tensile strength.

Material	Density ( $\times 10^3 \text{ kg/m}^3$ )	Young's modulus E (GPa)	Specific modulus
WFA-25%SAFFIL	2.2	65.5	29.8
WFA-25%SAFFIL-CNTs	2.8	83.5	29.8
Steel	7.9	210	26.6

**Table 4.1:** Density, Young's modulus and specific modulus of different materials: WFA-25% SAFFIL-CNTs, WFA-25% SAFFIL and steel.

### 4.1.1.2 Elastic shear modulus spectra

Elastic shear modulus was measured as a function of temperature during thermal cycling for WFA-25%SAFFIL-CNTs and WFA-25%SAFFIL (Fig. 4.1). The spectra of both composites show that the presence of CNTs results in an increase in the elastic shear modulus. The elastic shear modulus spectra during thermal cycling present a hysteresis in both composites. However, the hysteresis is more evident in WFA-25%SAFFIL-CNTs than in WFA-25%SAFFIL. In addition, the elastic shear modulus spectrum is higher during heating than during cooling in WFA-25%SAFFIL-CNTs, while this is opposite in the case of WFA-25%SAFFIL.

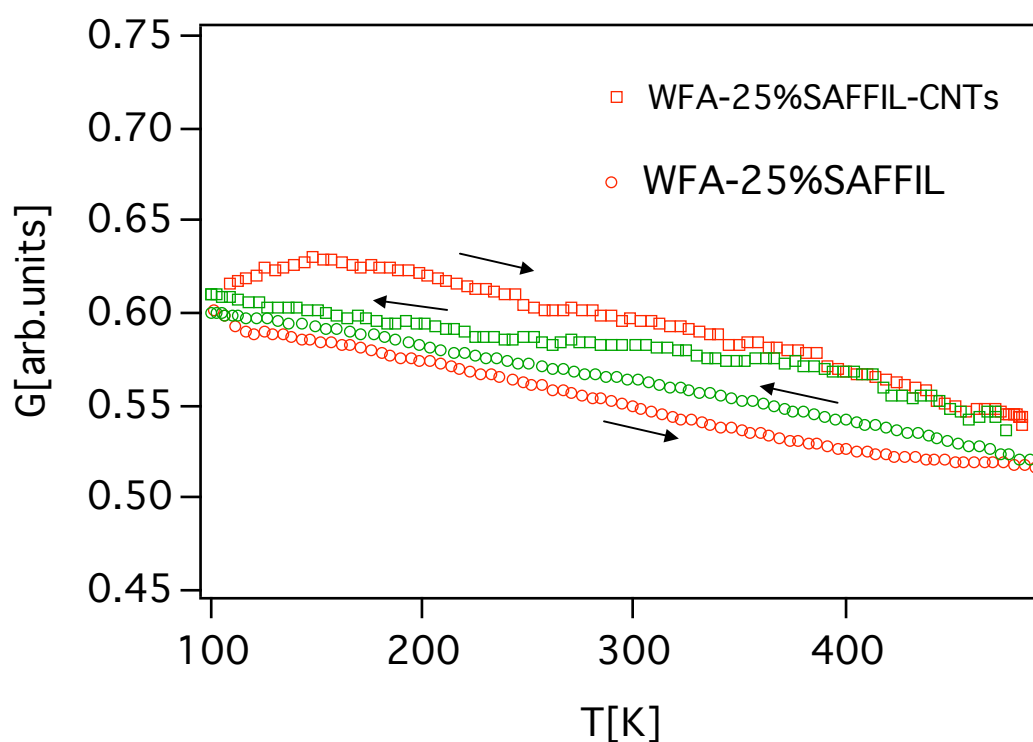


**Fig. 4.1:** Shear modulus spectra measured in WFA-25%SAFFIL-CNTs and in WFA-25%SAFFIL at frequency  $f = 0.5\text{Hz}$ , temperature change rate  $\dot{T} = 2\text{K/min}$  and strain amplitude  $\varepsilon = 10^{-5}$ .

The results show that CNTs increase Young's Modulus and shear modulus in WFA-25%SAFFIL-CNTs composite. This suggests that the bonding between WFA matrix and

CNTs is efficient so that the load can be transferred from the matrix to carbon nanotubes and to the SAFFIL fibres. CNTs can serve as reinforcements in metal matrix composites.

### 4.1.1.3 Internal friction behaviour

#### I Mechanical loss spectra during thermal cycling

Fig. 4.2 shows the mechanical loss spectra for WFA-25%SAFFIL-CNTs and for WFA-25%SAFFIL composites during thermal cycling. The measurements were performed at temperature variation rate of 2 K/min and oscillation frequency of 0.5 Hz. A maximum is observed in the mechanical loss spectra during cooling between 350 K and 100 K in both materials. The mechanical loss maximum is slightly higher for WFA-25%SAFFIL-CNTs than

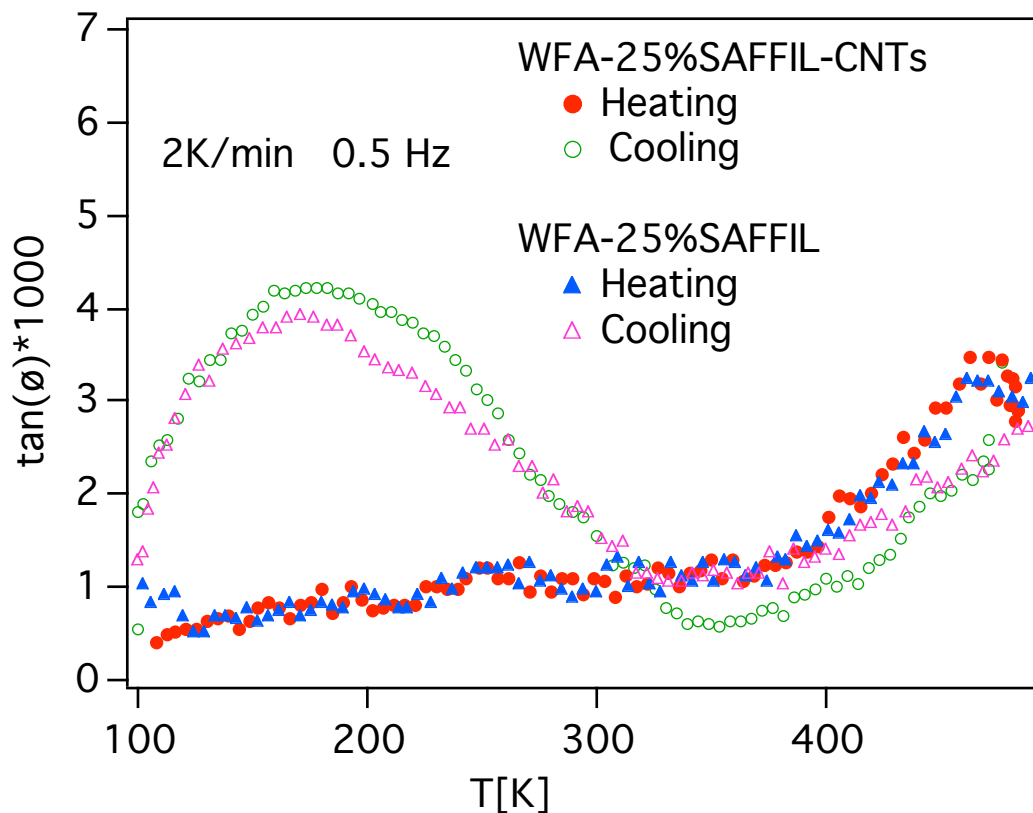


**Fig. 4.2:** Mechanical loss spectra measured for WFA-25%SAFFIL-CNTs and for WFA-25%SAFFIL at frequency  $f = 0.5\text{Hz}$ , temperature change rate  $\dot{T} = 2\text{K/min}$  and strain amplitude  $\varepsilon = 10^{-5}$ .

for WFA-25%SAFFIL. Moreover, one can note a shift of the spectrum towards higher temperature in WFA-25%SAFFIL-CNTs between 270 K and 160 K with respect to that in WFA-25%SAFFIL. In higher temperature range between 490 K and 325 K, the mechanical loss is lower in the case when CNTs are present. Between 320 K and 270 K, the two curves measured in two materials overlap. During heating, mechanical loss exhibits an increasing background. This increasing background is almost the same in both materials.

## II Effect of temperature variation rate

Mechanical loss spectra were also measured during thermal cycling with different temperature variation rates ( $\dot{T}$ ) for both WFA-25%SAFFIL-CNTs and WFA-25%SAFFIL. Fig. 4.3 displays the mechanical loss as a function of temperature for WFA-25%SAFFIL-CNTs (a) and for WFA-25%SAFFIL (b) during cooling. These mechanical loss spectra were measured with oscillation frequency of 0.5 Hz and different cooling rates ( $\dot{T}$ ). In the extreme case of 0 K/min, the points were extracted from the spectrum shown in Fig. 4.4, corresponding to the isothermal equilibrium values achieved after annealing. This spectrum was obtained during the measurement with oscillation frequency of 0.5 Hz and cooling rate of 3 K/min interrupted by isothermal annealings for 1 h at different temperatures. When the temperature is held constant, the mechanical loss decreases to stabilize at an isothermal equilibrium value. Because the mechanical loss increases immediately once the cooling starts again, the isothermal equilibrium does not represent a microstructural modification. However, the fact that the mechanical loss increases during cooling, with respect to the equilibrium value, indicates that an additional response in mechanical loss occurs when temperature changes. Actually, this transient mechanical loss depends on the temperature variation rate ( $\dot{T}$ ) (Fig. 4.3). It is observed that when cooling rate ( $\dot{T}$ ) increases, in both materials the transient mechanical loss increases rapidly, especially in the temperature range between 350 K and 100 K.

It is found that during cooling between 270 K and 160 K, with the same temperature variation rate the mechanical loss is slightly higher when CNTs are present, i.e. the curvatures of the spectra for WFA-25%SAFFIL-CNTs are larger than that for WFA-25%SAFFIL. This difference between the mechanical loss spectrum for WFA-25%SAFFIL-CNTs and that for

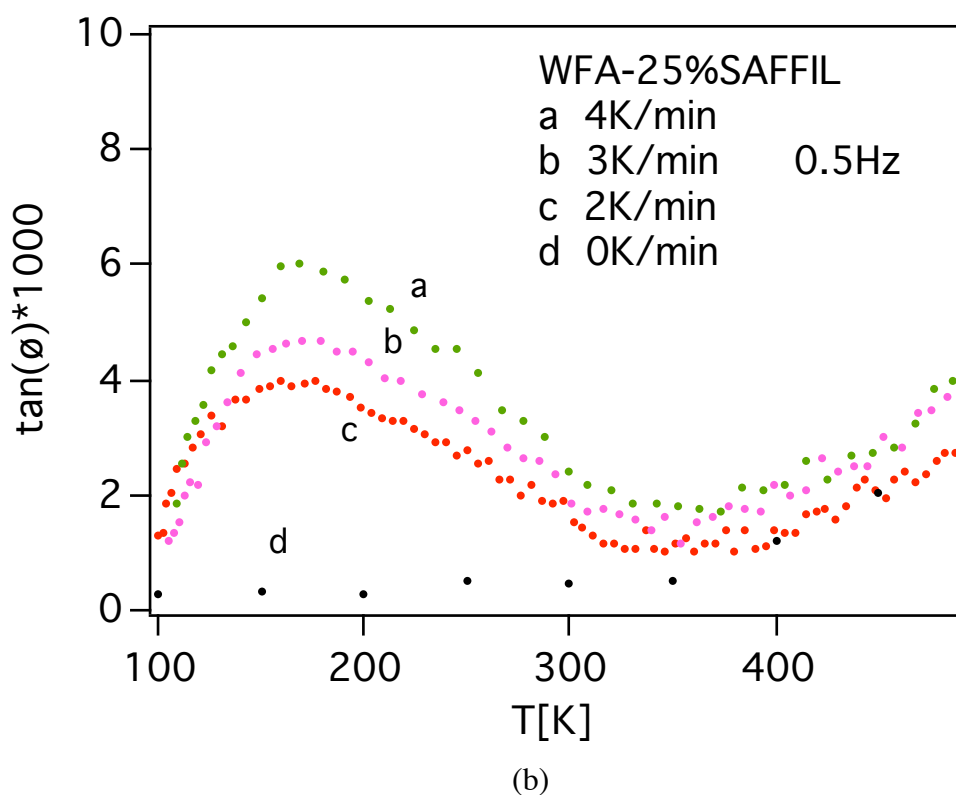
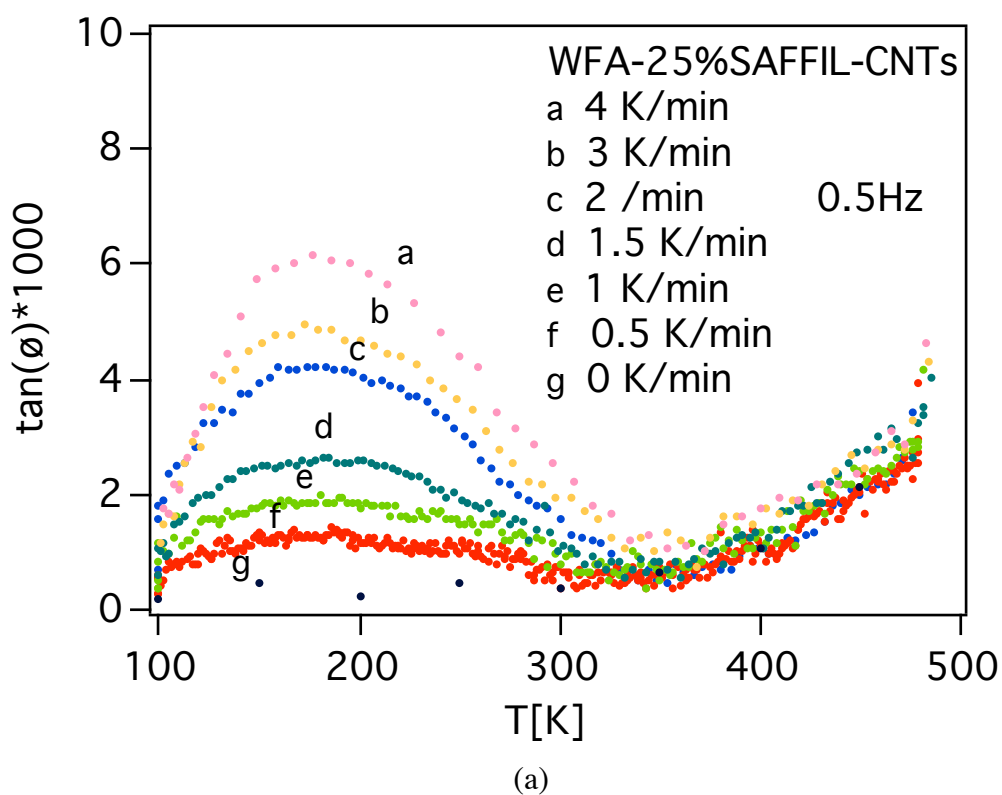


**Fig. 4.3:** Mechanical loss spectra measured for WFA-25%SAFFIL-CNTs (a) and for WFA-25%SAFFIL (b) at different cooling rates,  $f = 0.5\text{Hz}$ ,  $\varepsilon = 10^{-5}$ .

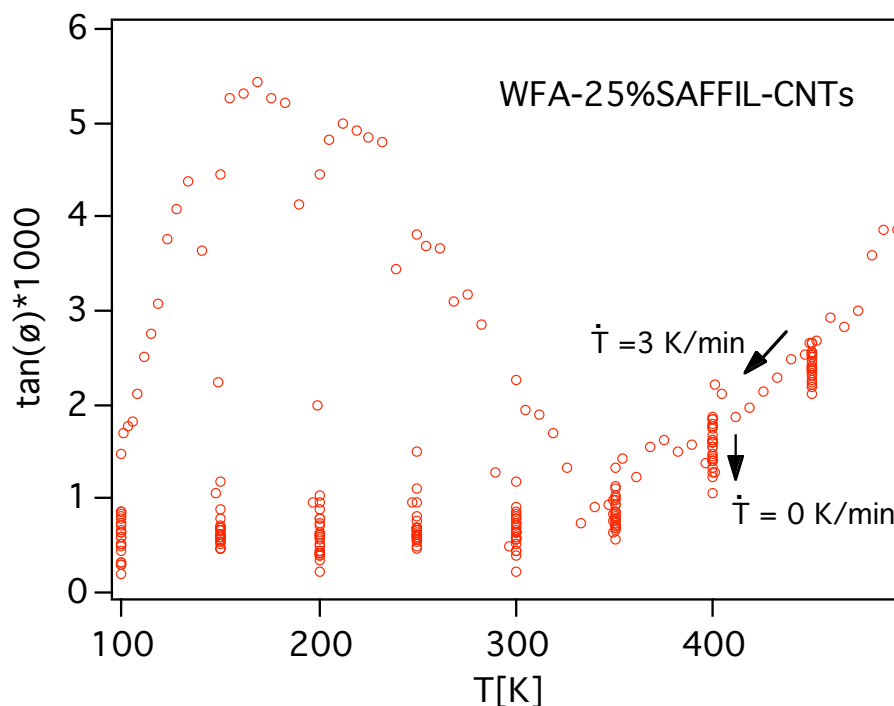


**Fig. 4.4:** Mechanical loss measured for WFA-25%SAFFIL-CNTs. Cooling ( $\dot{T} = 3 \text{ K/min}$ ) is interrupted by isothermal annealing at 450K, 400 K, 350 K 300 K, 250 K, 200 K, 150 K and 100 K for 1 hour.  $f = 0.5 \text{ Hz}$ ,  $\varepsilon = 10^{-5}$ .

WFA-25%SAFFIL is clearly observed in Fig. 4.2, where the mechanical loss spectra were obtained with cooling rate of 2 K/min and oscillation frequency of 0.5 Hz.

### III Effect of frequency

Oscillation frequency also has an effect on the mechanical loss of these composites. Fig. 4.5 displays the function of mechanical loss varying with oscillation frequency in WFA-25%SAFFIL-CNTs (Fig. 4.5 a) and in WFA-25%SAFFIL (Fig. 4.5 b). The spectra were measured under experimental condition of cooling rate of 3K/min. The mechanical loss maximum height increases in both materials when the oscillation frequency decreases. However, with the addition of CNTs, the mechanical loss maximum increases much more rapidly in WFA-25%SAFFIL-CNTs than in WFA-25%SAFFIL. In addition, for temperature higher than 350 K and frequency lower than 0.05 Hz, one observes that mechanical loss increases when frequency decreases in WFA-25%SAFFIL-CNTs, but not in WFA-25%SAFFIL.



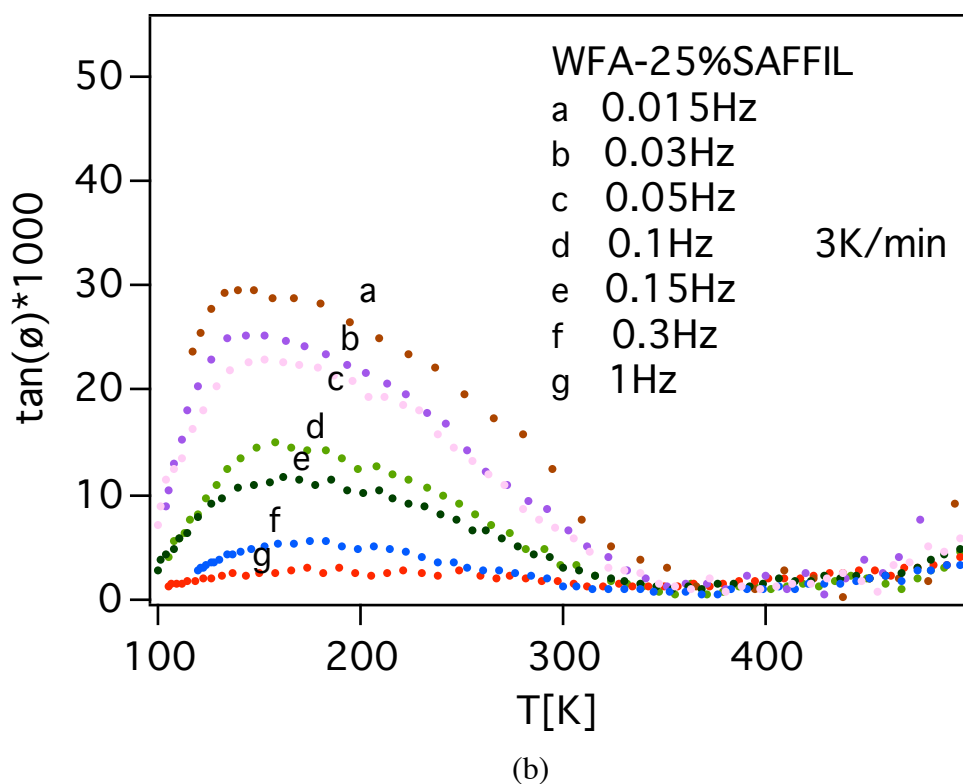
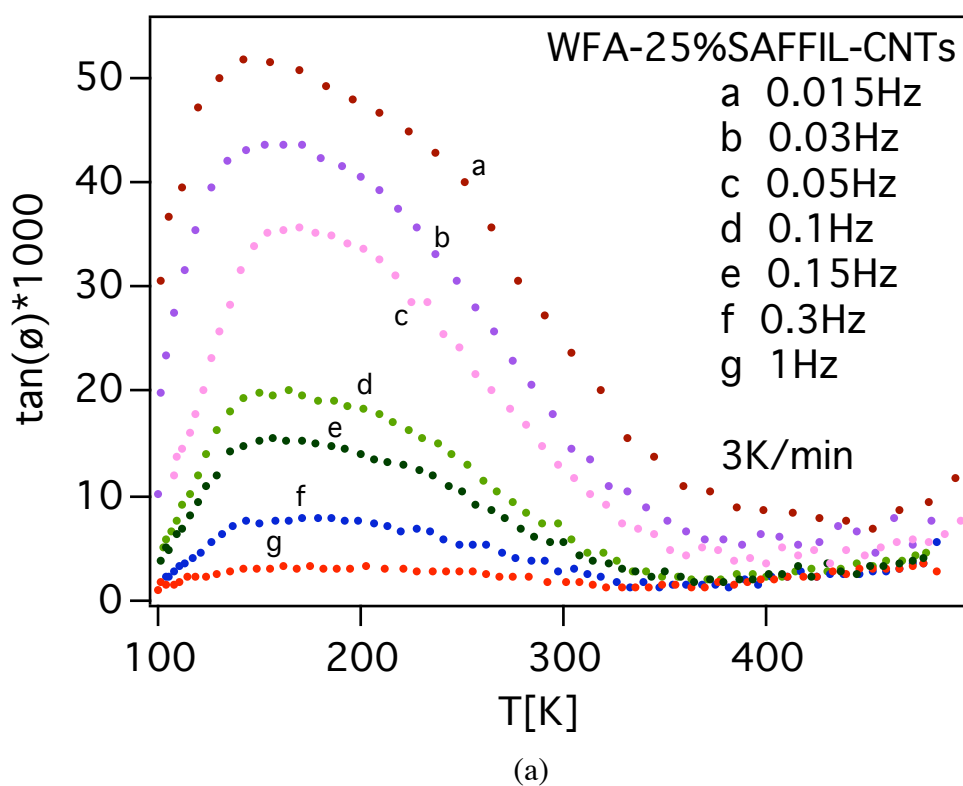


**Fig. 4.5:** Mechanical loss spectra measured in WFA-25%SAFFIL-CNTs (a) and in WFA-25%SAFFIL (b) at cooling rate 3K/min and different frequencies.

#### IV Dependence of mechanical loss on $\dot{T}/\omega$

As it has been shown above, mechanical loss in both materials all varies with temperature, exhibiting a maximum in the spectrum during cooling. The mechanical loss maximum height depends on the temperature variation rate and the oscillation frequency. Mechanical loss measured at 200 K versus ratio  $\dot{T}/\omega$  is plotted for both materials in Fig. 4.6. It is found from these two curves that the dependence of mechanical loss on the ratio  $\dot{T}/\omega$  for both materials is nonlinear. For small values of  $\dot{T}/\omega$ , both curves exhibit non-linearity. However, for larger values of  $\dot{T}/\omega$ , both curves can be considered linear. Moreover, the height of the curve in the case with CNTs increases with  $\dot{T}/\omega$  much more rapidly than in the case without CNTs.

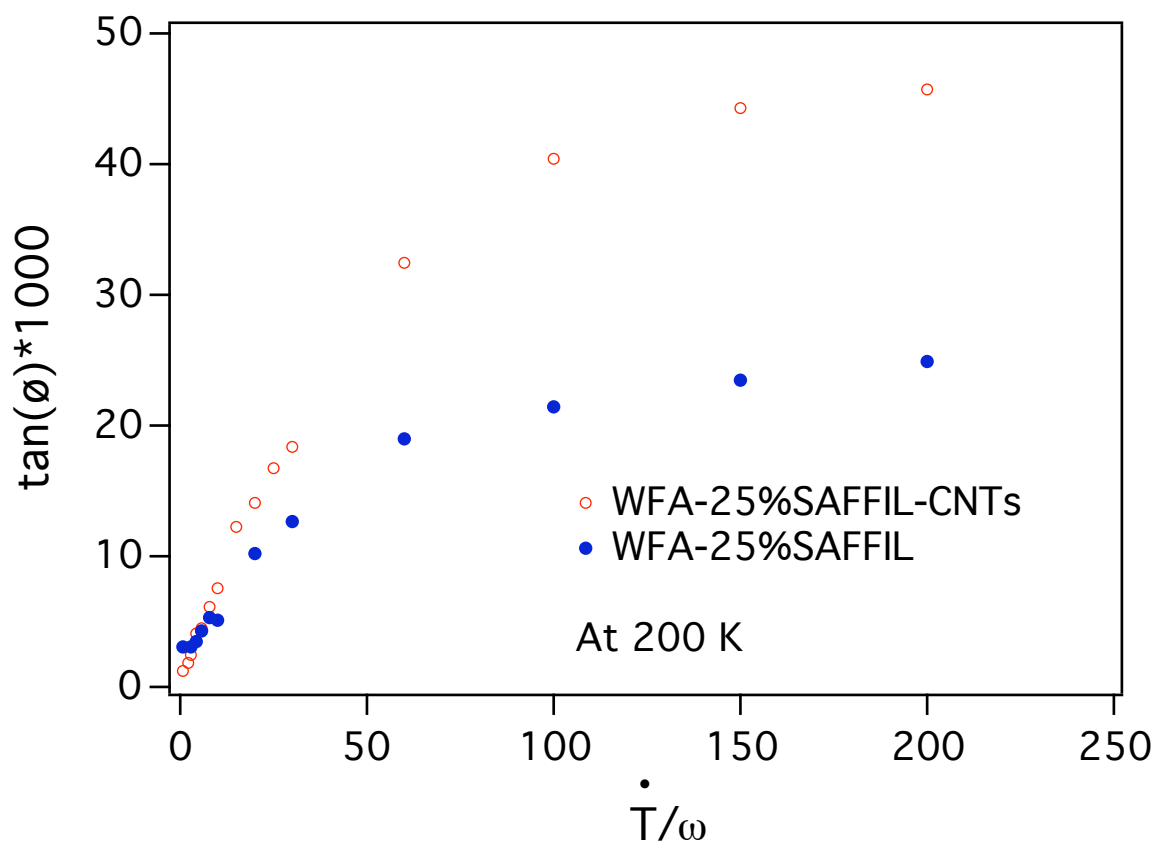


**Fig. 4.6:** Mechanical loss as a function of  $\dot{T}/\omega$  for WFA-25%SAFFIL-CNTs and for WFA-25%SAFFIL.

## 4.1.2 Interpretation of internal friction behaviour

### 4.1.2.1 Theoretical model

Non-linearity of the dependence of mechanical loss on  $\dot{T}/\omega$  has been observed in Mg-based composites by Mayencourt and Schaller [96]. In order to interpret the obtained experimental results, the authors have developed a theoretical model based on dislocation motion near the reinforcement-matrix interfaces. In their model, dislocation motion is assumed to be controlled by a solid friction mechanism in the matrix. According to this model, dislocations can glide only when the sum of mechanical and thermal stresses, which are generated at the fibre-matrix interface due to the mismatch of thermal expansion coefficients between two different phases, exceeds the critical stress for breakaway. These dislocations can not move back even when the total stress is lower than the critical stress. This model leads to an approximation of the transient mechanical loss due to the motion of dislocations associated to temperature variation rate and the oscillation frequency:

$$\tan(\phi) = 2 \frac{\Lambda b^2}{J_{el} K} CE\Delta\alpha \frac{\dot{T}}{\omega\sigma_0} \frac{1 - \frac{\pi}{2} CE\Delta\alpha \frac{\dot{T}}{\omega\sigma_0}}{1 + \frac{\pi}{2} CE\Delta\alpha \frac{\dot{T}}{\omega\sigma_0}}$$

if  $\frac{\dot{T}}{\omega\sigma_0} < \frac{2}{3\pi} \frac{1}{CE\Delta\alpha}$  (4.1)

$$\tan(\phi) = \frac{1}{4} \frac{\Lambda b^2}{J_{el} K} \left( CE\Delta\alpha \frac{\dot{T}}{\omega\sigma_0} + \frac{2}{\pi} \right)$$

$$\text{if } \frac{2}{3\pi} \frac{1}{CE\Delta\alpha} < \frac{\dot{T}}{\omega\sigma_0} < \frac{2}{\pi} \frac{1}{CE\Delta\alpha} \quad (4.2)$$

where  $\Lambda$  is dislocation density,  $b$  the Burgers vector,  $J_{el}$  the elastic compliance,  $K$  the coefficient of restoring force,  $E$  Young's modulus,  $C$  a geometrical factor which takes into account the stress profile at the interface and the fibre concentration,  $\Delta\alpha$  the thermal expansion coefficient mismatch,  $\dot{T}$  the temperature variation rate,  $\sigma_0$  the applied stress maximum,  $\omega$  the oscillation frequency. From equation (4.1), one can deduce a linear equation when taking the limit of equation (4.1) for small values of  $\dot{T}/(\omega\sigma_0)$ . This model was employed to analyse the experimental results obtained for Mg-based composites. A theoretical curve calculated from this model was used to fit the mechanical loss points measured during cooling at a certain temperature (e.g., at 410 K in the case of Mg<sub>2</sub>Si/Mg composite) [96]. It has been shown that by adjusting the constants  $K$  and  $C$ , the theoretical curve fits the experimental points perfectly. This means that the experimental results obtained for Mg-based composites can be well interpreted by the model [96]. In other words, dislocation gliding controlled by solid friction was identified as the stress relaxation mechanism in Mg-based composites.

#### 4.1.2.2 Interpretation of internal friction behaviour in WFA-25%SAFFIL-CNTs

##### I General discussion

In both WFA-25%SAFFIL-CNTs and WFA-25%SAFFIL composites, one has seen a maximum in the mechanical loss spectrum measured during cooling (Fig.4.2). Actually, a similar maximum has been reported in some other metal matrix composites [96, 97]. In those references, the mechanical loss maximum is attributed to the evolution of the dislocation microstructure during thermal cycling, because of the large thermal stresses generated near the interfaces between fibres and matrix due to the large mismatch of thermal expansion coefficients between the fibre reinforcement and the matrix. In Mg-based composites such as Mg-Al<sub>2</sub>O<sub>3</sub> [96], the dislocation motion was interpreted as controlled by solid friction.

In order to interpret the mechanical loss maximum and identify the thermal stress relaxation mechanism in WFA-25%SAFFIL-CNTs and WFA-25%SAFFIL, the model of Mayencourt [96] has been used. It is found that the experimental results obtained in WFA-25%SAFFIL-CNTs and WFA-25%SAFFIL and the calculated curves from the solid friction model have a good correspondence (Fig. 4.7). This suggests that the model of stress relaxation by dislocation motion controlled by a solid friction mechanism such as pinning-depinning by point defects also holds true in WFA-25%SAFFIL-CNTs and WFA-25%SAFFIL. More precisely, during cooling when the temperature is at about 350 K (Fig. 4.2), thermal stresses exceed the yield stress of the matrix, and dislocations are pushed away from the SAFFIL fibre-matrix interfaces. Subsequently, the dislocations continue to glide in the matrix until they meet another stronger pinning centre. Upon further cooling, more and

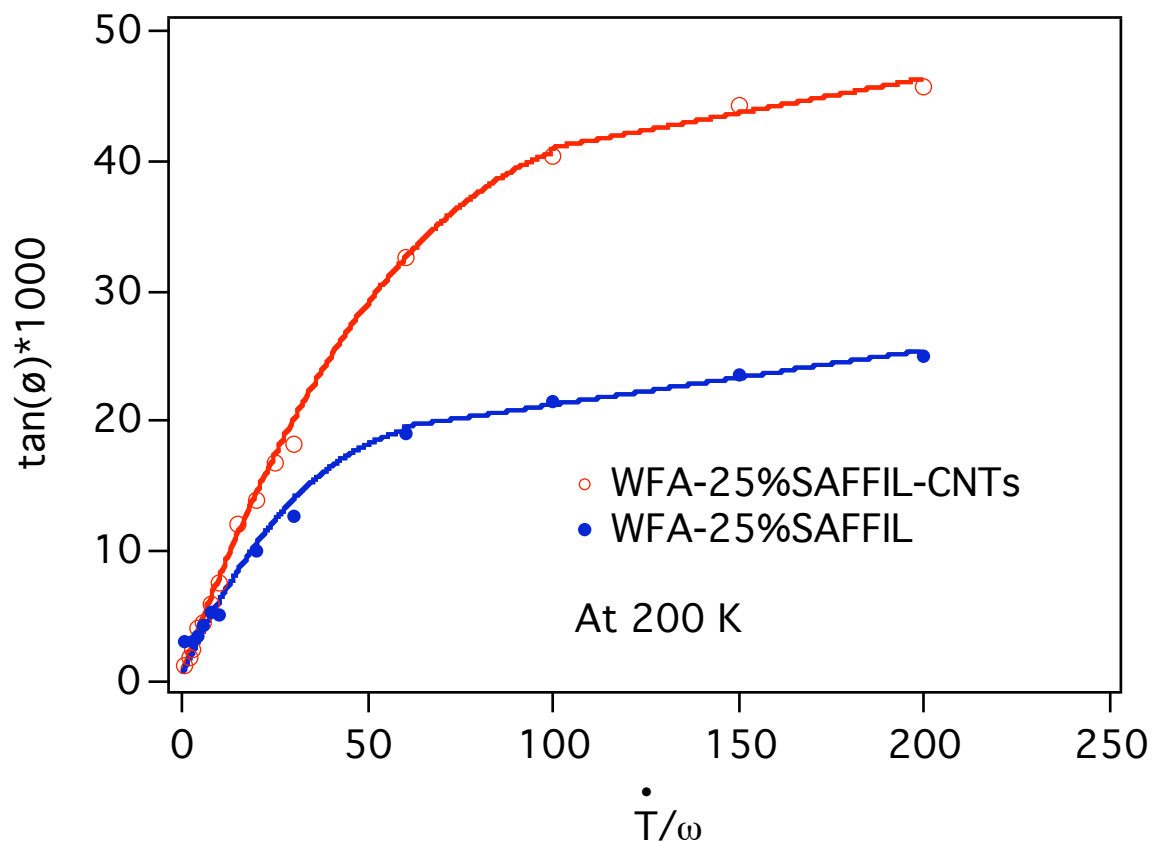


**Fig. 4.7:** Mechanical loss as a function of  $\dot{T}/\omega$  measured at 200 K and the curves calculated from the solid friction model for WFA-25%SAFFIL-CNTs and for WFA-25%SAFFIL.

more dislocations are generated under the effect of thermal stresses and glide away from the interfaces. The dislocation motion results in an increase in mechanical loss. For lower temperature ( $T < 160$  K), dislocation breakaway would become more difficult. In other words, the dislocation mobility decreases with temperature and consequently the mechanical loss decreases, forming the maximum shape in the mechanical loss spectrum. During heating, dislocation mobility increases with temperature. The dislocations, which were pinned by pinning centres such as solute atoms during previous cooling, are activated and move back to the interfaces. On the way back to the interfaces, dislocations meet the same obstacles. However, as temperature increases, the critical stress for depinning decreases and dislocation mobility increases continuously with temperature. The dislocation motion gives rise to a continuously increasing mechanical loss as a function of temperature (Fig. 4.2).

In Fig. 4.3 it is observed that the mechanical loss maximum increases when the temperature variation rate ( $\dot{T}$ ) increases. Moreover, with the same temperature variation rate, the mechanical loss maximum is slightly higher in the case of CNT additions. On the other hand, the mechanical loss maximum increases more rapidly when oscillation frequency decreases in the case of CNT doped specimen (Fig. 4.5). The mechanical loss as a function of  $\dot{T}/\omega$  at 200 K (Fig. 4.7) can be divided into two sections: a non-linear section with small values of  $\dot{T}/\omega$  and a linear section with large values of  $\dot{T}/\omega$ . The theoretical curves (solid curves) calculated from the model of Mayencourt [96] fit the experimental results well. The non-linear sections of the theoretical curves are calculated from equation (4.1) with values of  $\lambda b^2/J_{el}K = 1.92 \times 10^{-1}$  and  $CE\Delta\alpha/\sigma_0 = 2.08 \times 10^{-3}$  for WFA-25%SAFFIL-CNTs, and with values of  $\lambda b^2/J_{el}K = 8.99 \times 10^{-2}$  and  $CE\Delta\alpha/\sigma_0 = 3.56 \times 10^{-3}$  for WFA-25%SAFFIL. The linear portions of the curves are obtained from equation (4.2) with  $\lambda b^2/J_{el}K = 2.23 \times 10^{-1}$  and  $CE\Delta\alpha/\sigma_0 = 9.53 \times 10^{-4}$  for WFA-25%SAFFIL-CNTs and with  $\lambda b^2/J_{el}K = 1.06 \times 10^{-1}$  and  $CE\Delta\alpha/\sigma_0 = 1.57 \times 10^{-3}$  for WFA-25%SAFFIL. In order to compare these “fitting - coefficients” more clearly, these values are listed in Table 4.2.

By comparing the coefficients in table 4.2, one finds that in WFA-25%SAFFIL-CNTs the values of coefficients of  $\lambda b^2/J_{el}K$  for two sections (non-linear and linear) are higher

than those for the corresponding sections in WFA-25%SAFFIL, respectively. This means that the density of mobile dislocations,  $\Lambda$ , is higher when CNTs are present. On the contrary, the values of coefficients of  $CE\Delta\alpha/\sigma_0$  for WFA-25%SAFFIL-CNTs are smaller than those for WFA-25%SAFFIL. This may be interpreted by considering that the parameter  $C$ , which is associated with the interface strength, is smaller in WFA-25%SAFFIL-CNTs. CNTs would be then responsible for a softening of the fibre-matrix interface. A softer interface would be positive in toughness improvement, and particularly in improving resistance to thermal fatigue, because crack propagation will be blunted in the soft region. On the other hand, a strong interface may be responsible for crack propagation in the reinforcements, which leads to irreversible damage accumulation.

Material	$\Lambda b^2 / J_{el} K$		$CE\Delta\alpha / \sigma_0$	
	Nonlinear Section (4.1)	Linear Section (4.2)	Nonlinear section (4.1)	Linear Section (4.2)
WFA-25%SAFFIL-CNTs	$1.92 \times 10^{-1}$	$2.23 \times 10^{-1}$	$2.08 \times 10^{-3}$	$9.53 \times 10^{-4}$
WFA-25%SAFFIL	$8.99 \times 10^{-2}$	$1.06 \times 10^{-1}$	$3.56 \times 10^{-3}$	$1.57 \times 10^{-3}$

**Table 4.2:** Values of coefficient  $\Lambda b^2 / J_{el} K$  and  $CE\Delta\alpha / \sigma_0$  in equations (4.1) and (4.2) for WFA-25%SAFFIL-CNTs and for WFA-25%SAFFIL.

## II Interpretation of the effect of CNTs on the mechanical loss spectrum

In Fig. 4.2 it is shown that due to the addition of CNTs, the mechanical loss as measured upon cooling in WFA-25%SAFFIL-CNTs is lower than in WFA-25%SAFFIL between 490 K and 325 K, but it is higher in the temperature range between 270 K and 160 K.

The lower value of mechanical loss in WFA-25%SAFFIL-CNTs between 490 K and 325 K could be due to CNTs, which behave as extra dislocation pinning centres. This additional pinning of dislocations reduces the dislocation loop length and consequently the mechanical loss. However, when temperature decreases to about 325 K, the sum of thermal and mechanical stress overcomes the critical stress for dislocation breakaway and the mechanical loss increases rapidly. On the other hand, CNTs can be considered as points of

stress concentration and then activate the nucleation of dislocations. As a result, the dislocation density increases more rapidly upon cooling in WFA-25%SAFFIL-CNTs and so does the mechanical loss, leading to a larger maximum height in the mechanical loss spectrum. The maximum can be described by developing a simple model.

## 1. Theoretical modelling

The tiny tips of the carbon nanotubes can be considered as stress concentrators or stress amplifiers, which can act as agents for the nucleation of dislocations. Because of the tiny curvature radius of the tips, the thermal stresses at the tube tips are higher than those at the SAFFIL fibre interfaces. During cooling, the thermal stresses in the matrix near the tube tips are tenser and increase more rapidly than those in the other regions of the matrix. Elastic limit will be reached sooner in the matrix close by the CNT and consequently the nucleation of dislocations occurs sooner near the tips of the nanotubes than at the SAFFIL fibre-matrix flat interface. Fig. 4.8 shows the model of the dislocation nucleation at the tip of the nanotubes, which decorate the surface of SAFFIL fibres. It also presents the nucleation of dislocation from the interface between SAFFIL fibres and matrix, as well as the propagation of the dislocations originated from the nanotube tips and the SAFFIL-matrix interface.

When the dislocations propagate in the matrix, they encounter other CNTs, which are dispersed in the matrix during the infiltration of the preform. Together with solute atoms, these CNTs behave as obstacles and can pin the dislocation loops. During cooling, with the increasing thermal stresses, the dislocation loops propagate further away from the tips and the SAFFIL-matrix interface. As already mentioned, this dislocation motion would be controlled by a solid friction force.

Since the nanotube tips located at the SAFFIL-matrix interface can generate dislocations sooner, the same number of dislocations can be emitted from the interfaces, but earlier in WFA-25%SAFFIL-CNTs than in WFA-25%SAFFIL. As a result, the mechanical loss increases sooner and more rapidly in the case with the addition of CNTs (Fig. 4.2).

On the other hand, the more rapid enhancement in mechanical loss spectrum measured in WFA-25%SAFFIL-CNTs may be due to a higher density of dislocations in the composite with CNTs. However, as CNTs, which are located far away from the interface, can be



considered as obstacles to dislocations, the mobility of the dislocations may be lower, than in the corresponding CNT-free material. Simulating the maximum of the mechanical loss spectrum exemplifies this.

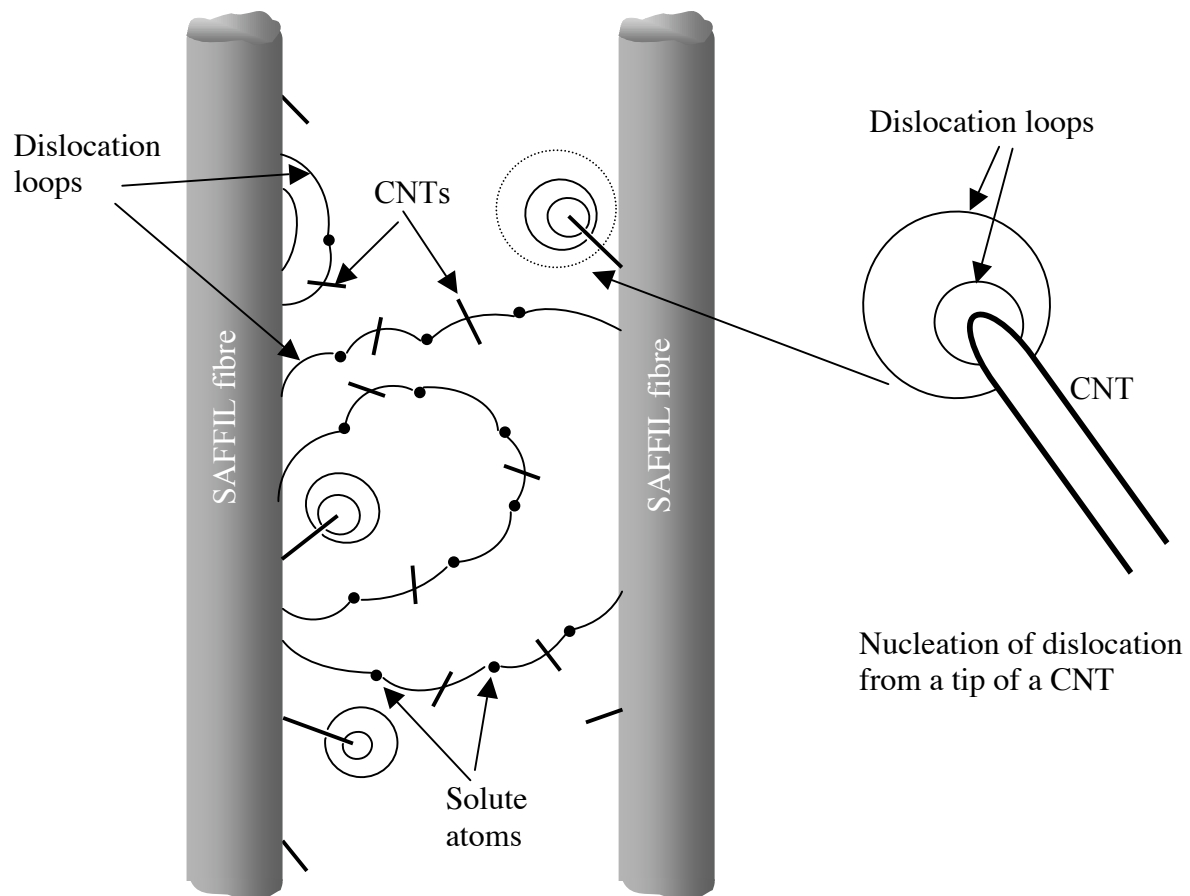


**Fig. 4.8:** Model of nucleation of dislocations from nanotube tips located in the SAFFIL-matrix interface and directly from the SAFFIL-matrix interface, as well as the propagation of these dislocations in the matrix.

## 2. Simulation of the mechanical loss maximum

From the model of Mayencourt [96], when  $\dot{T}/\omega$  is constant, equations (4.1) and (4.2) become an expression of mechanical loss as a function of temperature. The maximum of the mechanical loss is proportional to the ratio of  $\Lambda/K$ . The density of mobile dislocations,

$\Lambda(T)$ , and the coefficient of restoring force,  $K(T)$ , are considered as a function of temperature. Thus

$$\tan(\phi)_{\max} \propto \frac{\Lambda(T)}{K(T)} \quad (4.3)$$

Because the dislocation production is a function of thermal dilatation, which is proportional to temperature, one can assume that the density of dislocation is a linear function of temperature:

$$\Lambda(T) = \Lambda_0(T_e - T) \quad (4.4)$$

where  $\Lambda_0$  is a constant,  $T_e$  the temperature of equilibrium. From Fig. 4.2, one can see that the temperature of equilibrium  $T_e$  is equal to 350 K in both WFA-25%SAFFIL-CNTs and WFA-25%SAFFIL composites. In order to account for the different efficiency to nucleate dislocations in the two composites, one can modify the above equation into a power law with coefficient  $\chi$ :

$$\Lambda(T) = \Lambda_0(T_e - T)^\chi \quad (4.5)$$

As the coefficient of restoring force  $K$  may depend on the binding energy  $H$  between pinning points and dislocations, we can assume that  $K$  satisfies the Arrhenius law (equation 3.18):

$$K = K_0 \cdot e^{H/kT} \quad (4.6)$$

where  $K_0$  is a constant. Therefore by combining equations (4.5) and (4.6), the mechanical loss can be written as

$$\tan \phi \approx C_1 \Lambda_0 (T_e - T)^\chi e^{-\frac{H}{kT}} + C_2 \quad (4.7)$$

where  $C_1$  and  $C_2$  are constants. When choosing  $C_1 = 6.5 \times 10^{-5}$  as well as changing  $\chi$  and  $H$ , the mechanical loss maximum observed in Fig. 4.2 can be simulated by equation (4.7). Fig. 4.9 shows two mechanical loss maxima between 100 K and 350 K corresponding to the two composites, with and without CNTs, respectively. The corresponding values of the parameters of  $\chi$  and  $H$  are given in table 4.3.

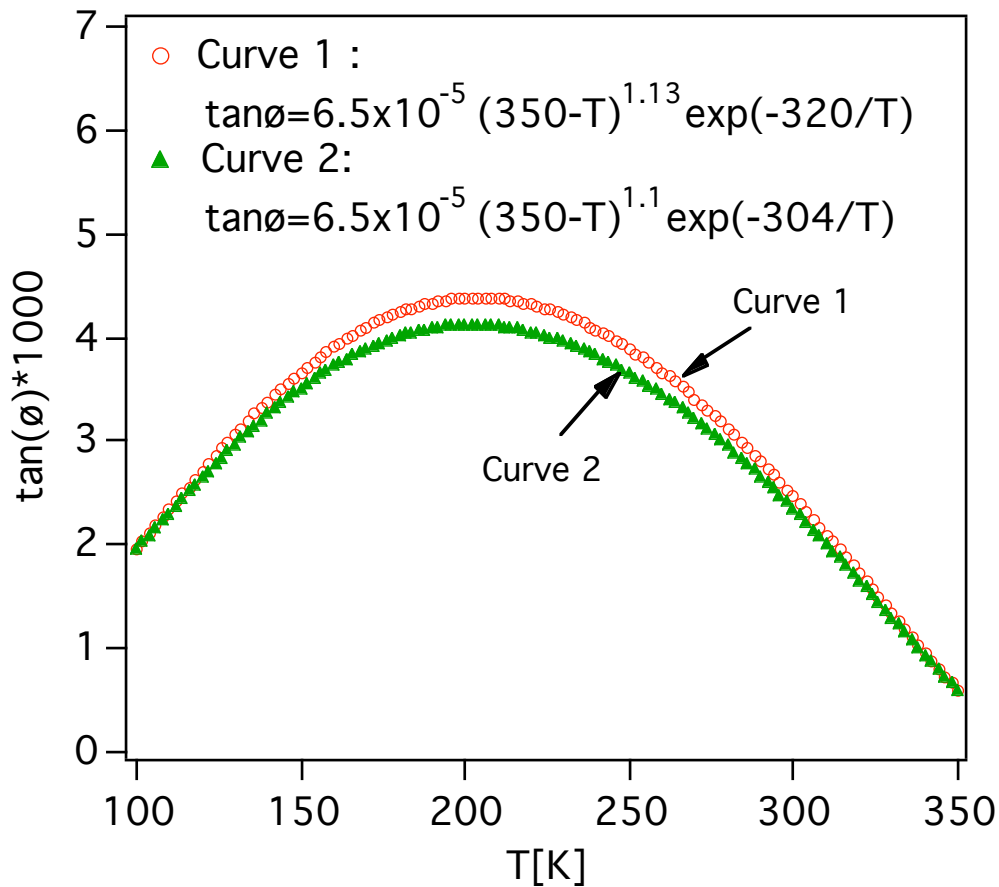


**Fig. 4.9** Simulation of mechanical loss maximum in WFA-25%SAFFIL-CNTs (curve 1) and WFA-25%SAFFIL (curve 2).

	$\chi$	$H$ (eV)	$H/k$ (K)
Graph 1	1.13	0.02752	320
Graph 2	1.10	0.02614	304

**Table 4.3:** Values of parameters of  $\chi$  and  $H$  chosen for simulating graphs shown in Fig. 4.9.

In Fig. 4.9 and table 4.3, it is found that with larger values of both  $\chi$  and  $H$ , the spectrum (curve 1 with CNTs) exhibits a higher maximum. This difference between curve 1 and curve 2 has a good agreement with the observation in the spectra measured in WFA-25%SAFFIL-CNTs and WFA-25%SAFFIL (Fig. 4.2). Equation (4.5) shows that larger value of  $\chi$  presents higher dislocation density. Thus the larger height and the shift of the mechanical loss maximum can be attributed to the additional enhancement of dislocation density. In WFA-25%SAFFIL-CNTs, CNTs are responsible for a higher damping, which would be due to an additional increase in the dislocation density during cooling.

On the other hand, the larger value of  $H$  (activation enthalpy) in the case of CNT doping means a higher barrier then larger difficulty for dislocation loops to breakaway. This causes a decrease in dislocation mobility at low temperature, because CNTs are extra pinning points on the dislocation loops.

## 4.2 Study of Mg-25%SAFFIL-CNTs composites

### 4.2.1 Mechanical loss and shear modulus spectra for two Mg-based composites

Mechanical loss and shear modulus ( $G$ , in arbitrary units) were measured in Mg-25%SAFFIL-MWCNTs (Fig. 4.10 a). Mg-25%SAFFIL-MWCNTs were processed by infiltration of a preform of 25 %vol. SAFFIL fibers, coated with MWCNTs by CVD (Fig. 2.10), with molten Mg. For the sake of comparison, a Mg-25%SAFFIL composite was processed by infiltration of a preform of 25 % vol. SAFFIL fibers under the same conditions as those for processing Mg-25%SAFFIL-WMCNTs. The mechanical loss and shear modulus of Mg-25%SAFFIL are plotted as a function of temperature in Fig. 4.10 b.

In Fig.4.10 Mg-25%SAFFIL and Mg-25%SAFFIL-MWCNTs exhibit similar internal friction spectra as a function of temperature, obtained with experimental conditions of  $\dot{T} = 2$  K/min and  $f = 1$  Hz. The mechanical loss depends weakly on temperature, as already reported

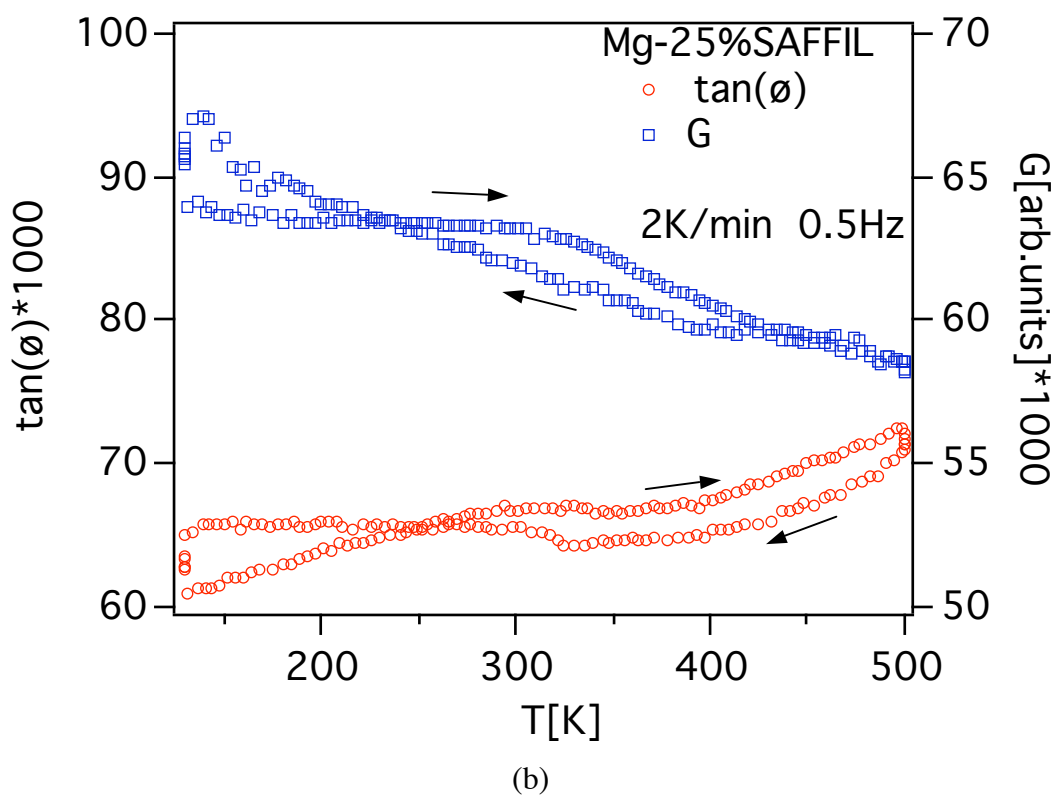
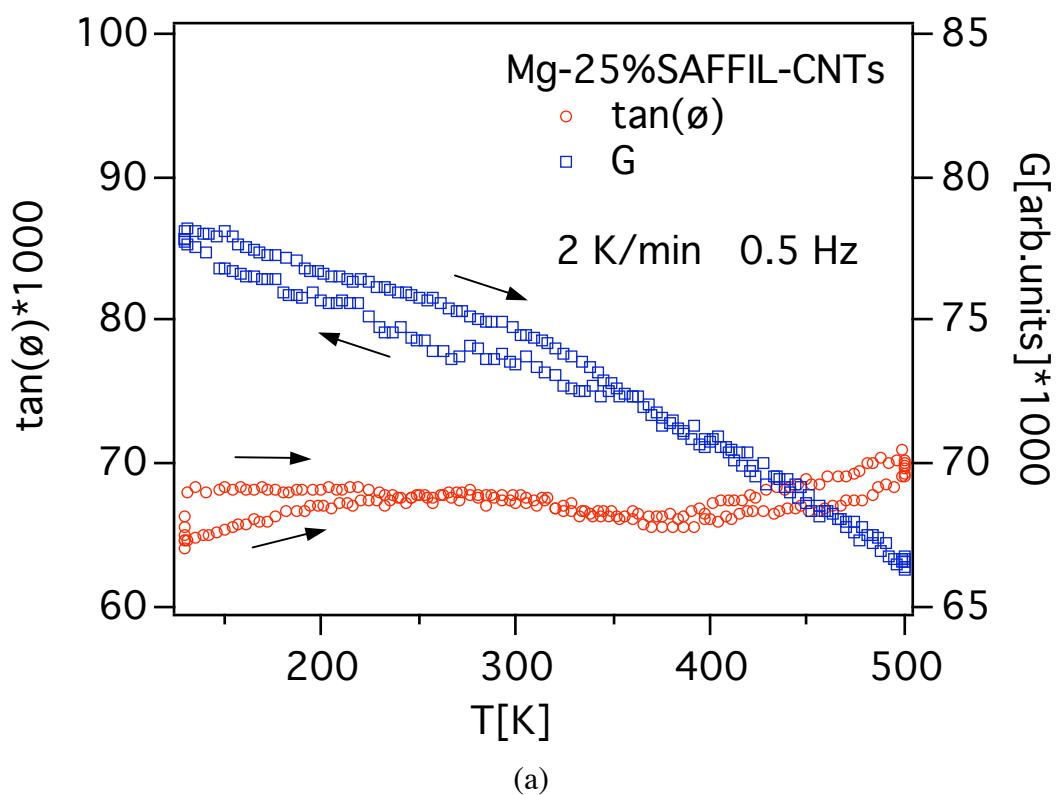


**Fig. 4.10:** Mechanical loss and shear modulus vs. temperature for Mg-25%SAFFIL-CNTs

(a), Mg-25%SAFFIL (b).  $\dot{T} = 2\text{K/min}$ ,  $f = 0.5\text{ Hz}$ ,  $\varepsilon = 10^{-5}$ .

by others [98]. Fig. 4.10 also shows a thermal hysteresis between the mechanical loss spectrum measured upon cooling and heating in both composites. A similar thermal hysteresis is observed in the shear modulus spectrum. The mechanical loss spectra obtained during cooling and during heating cross at the same temperature of 250 K in both composites. Upon heating a broad maximum of mechanical loss is observed at about 300 K. Corresponding to this maximum, a change of slope is observed in the shear modulus curve. The two composites exhibit a decreasing shear modulus with increasing the temperature and a hysteresis between cooling and heating.

In addition to these similarities, the internal friction spectra exhibit differences between the two composites (Fig. 4.11). It is observed that CNTs enhance the average level of the mechanical loss in the temperature range of measurements. More precisely, the mechanical loss is higher in the case with CNTs for  $T < 450$  K during cooling and for  $T < 350$  K during heating. As interpreted for Al-alloys matrices (§ 4.1), the increase in mechanical loss could be due to the effect of CNTs, which would favor dislocation motion around the

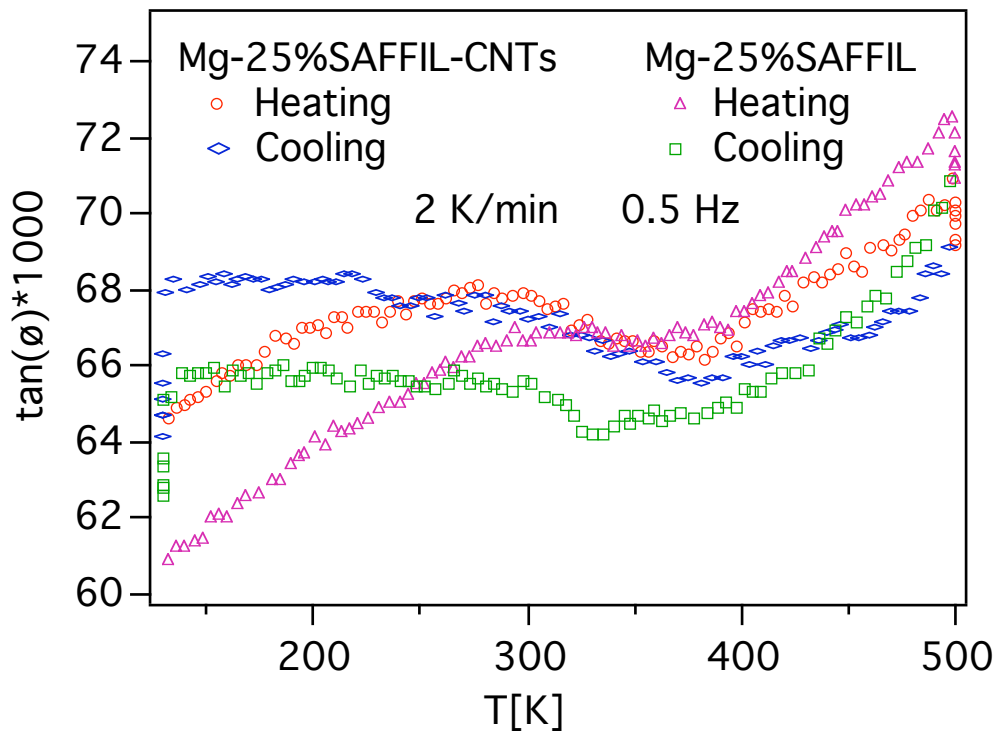


**Fig. 4.11:** Comparison between mechanical loss spectra measured in Mg-25%SAFFIL and

Mg-25%SAFFIL-CNTs.  $\dot{T} = 2\text{K/min}$ ,  $f = 0.5\text{ Hz}$ ,  $\varepsilon = 10^{-5}$ .

interfaces in Mg-25%SAFFIL-MWCNTs, so that the mechanical loss is higher when the temperature is lower than a certain value.

By comparing the mechanical loss spectra obtained in four composites: Mg-25%SAFFIL-MWCNTs, Mg-25%SAFFIL, WFA-25%SAFFIL-MWCNTs and Mg-25%SAFFIL, it is easy to find that the most striking difference is the mechanical loss maximum observed upon cooling in the two Al-matrix composites, which is absent in two Mg-matrix composites. In the case of Al-matrix, the maximum in mechanical loss was interpreted as due to the competition between the creation of mobile dislocations, the density of which is increasing upon cooling, and their mobility, which is decreasing with temperature. Here in the case of Mg-matrix, the absence of the maximum could be interpreted as if the dislocation mobility is still high at temperature as low as 100 K.

On the other hand, other researchers [98] found that the mechanical loss in Mg-25%SAFFIL composite was much lower than in other Mg-based composites such as SiC/Mg. They attributed the pronounced decrease in mechanical loss in Mg-25%SAFFIL to the large amount of impurities in the matrix. These impurities were considered as solute atoms, which were dissolved from the SAFFIL fibers into the magnesium matrix during the interfacial reaction between SAFFIL and matrix, due to the long contact time, when the composite was processed by infiltration. Thus the absence of the maximum in two Mg-based composites studied here may be explained as due to the large amount of solute atoms, which pin dislocations in Mg matrix. As a result, the mobility of the dislocations is low with respect to pure Mg in the whole measurement temperature range.

## 4.2.2 Relaxation mechanism of thermal stresses in Mg-25%SAFFIL-CNTs

Despite the absence of a damping maximum, as observed in WFA-25%SAFFIL-CNTs and WAF-25%SAFFIL, a  $\dot{T}$  effect can be observed in Mg-25%SAFFIL-CNTs at 240–130 K (Fig. 4.12). The effect of oscillation frequency ( $\omega$ ) on damping is more pronounced (Fig.

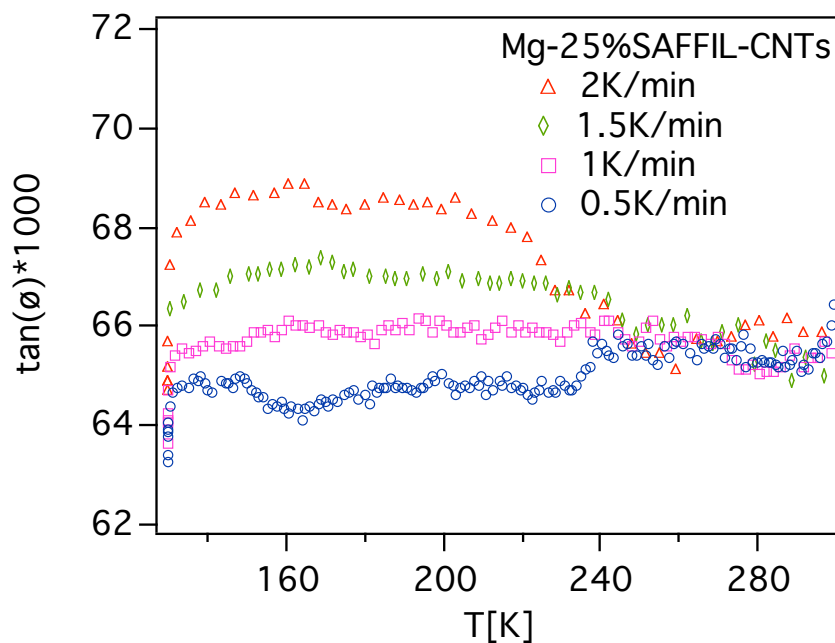


**Fig. 4.12:** Mechanical loss spectra measured between 300 K and 130 K during cooling in Mg-25%SAFFIL-CNTs, with  $f = 1$  Hz and different temperature rates: 2K/min, 1.5K/min, 1K/min and 0.5K/min, and,  $\varepsilon = 10^{-5}$ .

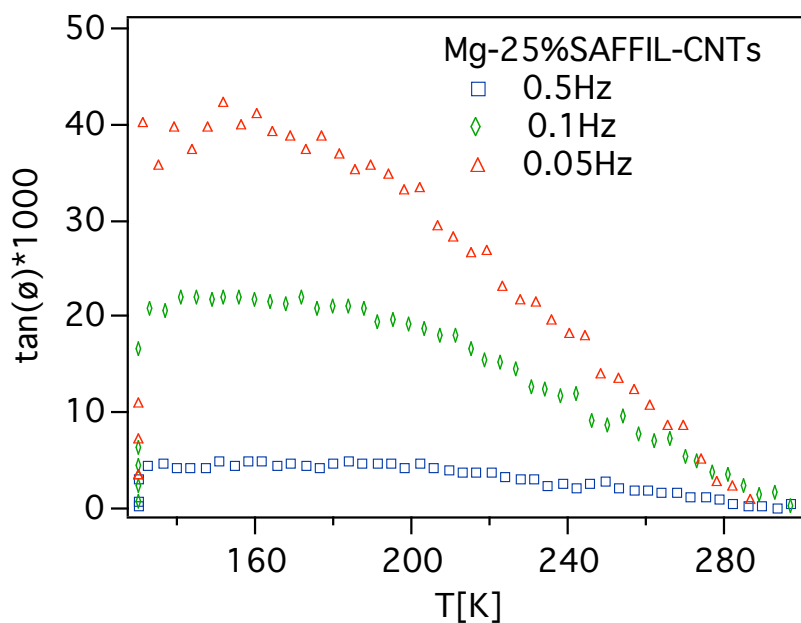


**Fig. 4.13:** Mechanical loss spectra measured between 300 K and 130 K during cooling in Mg-25%SAFFIL-CNTs with  $T = 2$  K/min and different oscillation frequencies: 0.5 Hz, 0.1 Hz and 0.05 Hz, and  $\varepsilon = 10^{-5}$ .



4.13). The mechanical loss increases strongly with decreasing the oscillation frequency. Fig. 4.14 shows the dependence of mechanical loss on  $\dot{T}/\omega$  (cycles), which was measured at 180 K.

In Fig. 4.14, one notes that the curve can be divided into two domains: non-linear and linear corresponding to small and large values of  $\dot{T}/\omega$ , respectively. When choosing correct values for the coefficients  $\Lambda b^2/J_{el}K$  and  $CE\Delta\alpha/\sigma_0$ , which are listed in table 4.4, equations (4.1) and (4.2) can fit the experimental points quite well (the solid curve in Fig. 4.14). The non-linear behavior would mean that the relaxation mechanism of interface thermal stresses may also be achieved by dislocation motion controlled by solid friction.

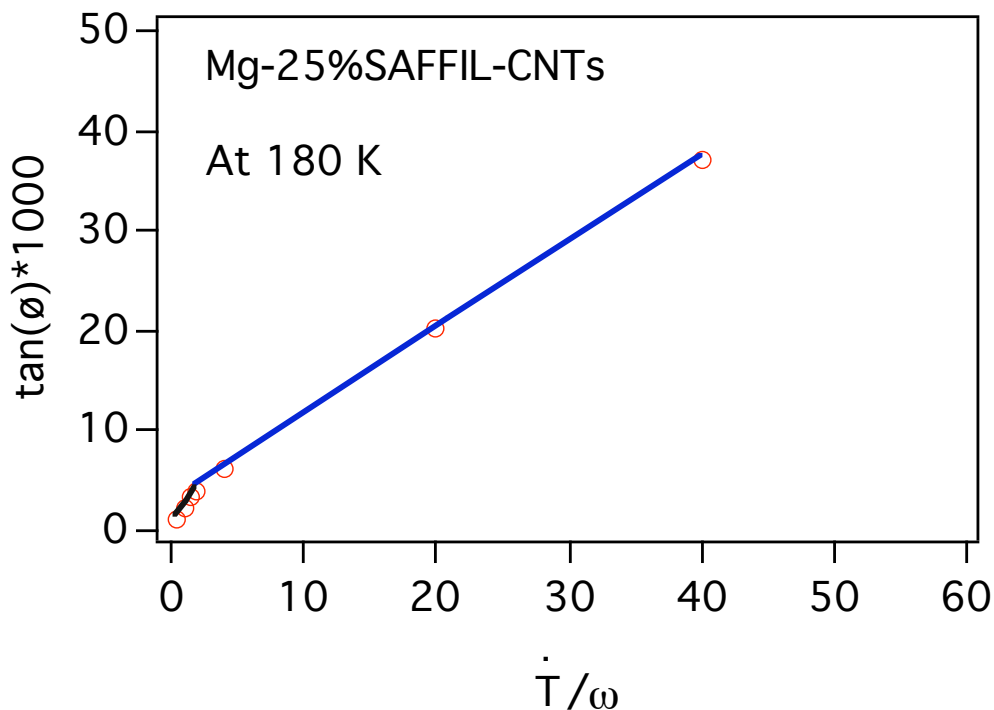


**Fig. 4.14:** Dependence of mechanical loss on  $\dot{T}/\omega$  measured at 180 K in Mg-25%SAFFIL-CNTs.

Table 4.4 shows the coefficients of  $\Lambda b^2/J_{el}K$  and  $CE\Delta\alpha/\sigma_0$  in equations (4.1) and (4.2) for Al alloys (WFA) and Mg reinforced with  $Al_2O_3$  SAFFIL fibers, which are

coated with carbon nanotubes. One finds that the coefficients of  $\Lambda b^2 / J_{el} K$  are smaller, while the coefficients of  $CE\Delta\alpha / \sigma_0$  are larger in Mg-25%SAFFIL-CNTs than in the case of Al-matrix. As the mobile dislocation density in Mg matrix is certainly not smaller than in Al matrix (dislocation damping in Mg is high), the smaller value of  $\Lambda b^2 / J_{el} K$  would be due to the higher elastic compliance  $J_{el}$ . As it concerns the coefficient  $CE\Delta\alpha / \sigma_0$ , the Young's modulus E is smaller for Mg and  $\Delta\alpha$  is of the same order of magnitude for an Al or Mg matrix. As a consequence the high value of  $CE\Delta\alpha / \sigma_0$  in Mg-25%SAFFIL-CNTs would mean that the interfacial strength is better in this system.

Material	$\Lambda b^2 / J_{el} K$		$CE\Delta\alpha / \sigma_0$	
	Nonlinear	Linear	Nonlinear	Linear
	Section (4.1)	Section (4.2)	section (4.1)	Section (4.2)
WFA-25%SAFFIL-CNTs	$1.92 \times 10^{-1}$	$2.23 \times 10^{-1}$	$2.08 \times 10^{-3}$	$9.53 \times 10^{-4}$
Mg-25%SAFFIL-CNTs	$2.68 \times 10^{-2}$	$1.52 \times 10^{-2}$	$5.28 \times 10^{-2}$	$2.27 \times 10^{-1}$

**Table 4.4:** Values of coefficients of  $\Lambda b^2 / J_{el} K$  and  $CE\Delta\alpha / \sigma_0$  in equations (4.1) and (4.2) for WFA-25%SAFFIL-CNTs and for Mg-25%SAFFIL-CNTs.

### 4.2.3 Comparison of shear modulus

Fig. 4.15 displays the shear modulus spectra in both Mg-25%SAFFIL-CNTs and Mg-25%SAFFIL. An enhancement of shear modulus is notable in Mg-25%SAFFIL-CNTs due to the presence of CNTs. This increase is about 17 % at 500K. As the level of damping was not decreased by the CNTs (see Fig. 4.10), this would mean that the CNTs improve the interfacial strength, confirming the above mentioned result as it concerns the parameter  $CE\Delta\alpha / \sigma_0$ : the CNTs improve the interface properties in Mg-Al<sub>2</sub>O<sub>3</sub> composites.

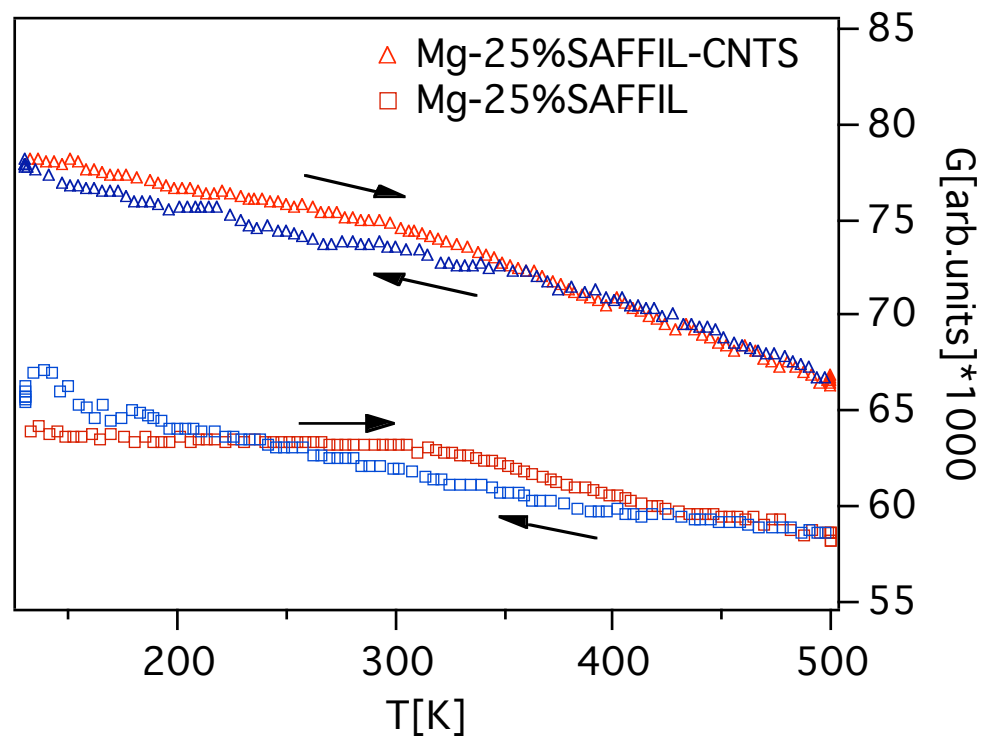


*Fig. 4.15: Shear modulus spectra measured in Mg-25%SAFFIL-CNTs and Mg-25%SAFFIL.*

$$\dot{T} = 2K/min, f = 0.5 \text{ Hz}, \varepsilon = 10^{-5}.$$

### 4.3 Conclusion

WFA-25%SAFFIL-CNTs and Mg-25%SAFFIL-CNTs composites were processed by gas pressure infiltration. Both SAFFIL fibers and carbon nanotubes were found to be well embedded in the matrix. The Young's and shear modulus of the composites were increased by coating the SAFFIL fibers with CNTs. A large maximum has been observed in the mechanical loss spectrum of WFA-25%SAFFIL-CNTs upon cooling. This maximum appears to be shifted towards higher temperature (between 270 K and 180 K) with respect to the maximum obtained in WFA-25%SAFFIL without CNTs. A model has been developed to interpret the effects of CNTs as follow: the CNTs located at the SAFFIL-matrix interface are assumed to favor dislocation nucleation, while the CNTs far away from the interface can pin the dislocations. The transient damping has been plotted as a function of  $\dot{T}/\omega$ . A non-linear function has been obtained this way, which was accounted for by the model of Mayencourt [96]. From this model it is concluded that the relaxation of the interface thermal stresses is achieved by hysteretic motion of dislocations in the matrix. A high level of the transient

damping as observed in WFA-25%SAFFIL-CNTs (Fig. 4.7) accounts for a high density of mobile dislocations. In Mg-25%SAFFIL-CNTs too, the average damping has been increased due to the addition of CNTs (Fig. 4.11). The geometrical factor  $CE\Delta\alpha/\sigma_0$  associated to the interfacial stress profile indicates that CNTs should be responsible for interface softening in WFA-25%SAFFIL-CNTs (Table 4.2) and interface strengthening in Mg-25%SAFFIL-CNTs (Table 4.4), with respect to the un-doped specimens.

# Chapter 5

## Mg-MWCNTs composites: experimental results and interpretations

---

### 5.1 General features of mechanical loss and shear modulus spectra

Magnesium reinforced with 1% or 2% multi-wall carbon nanotubes composites, which were processed by sintering, were characterized by tensile tests and mechanical spectroscopy. Fig. 5.1 shows a typical tensile test curve obtained in Mg-2%CNTs. The curve is characteristic for a metallic material, with elastic and plastic domains.

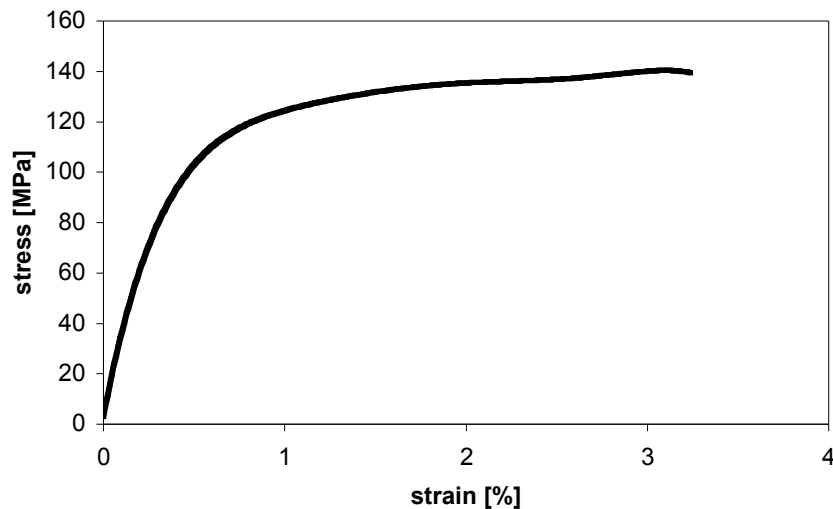


*Fig. 5.1: Stress-strain behavior of Mg-2wt.%CNT composites measured in tensile tests.*

yield strength	tensile strength	strain after fracture
89 MPa,	140 MPa	~ 3 %

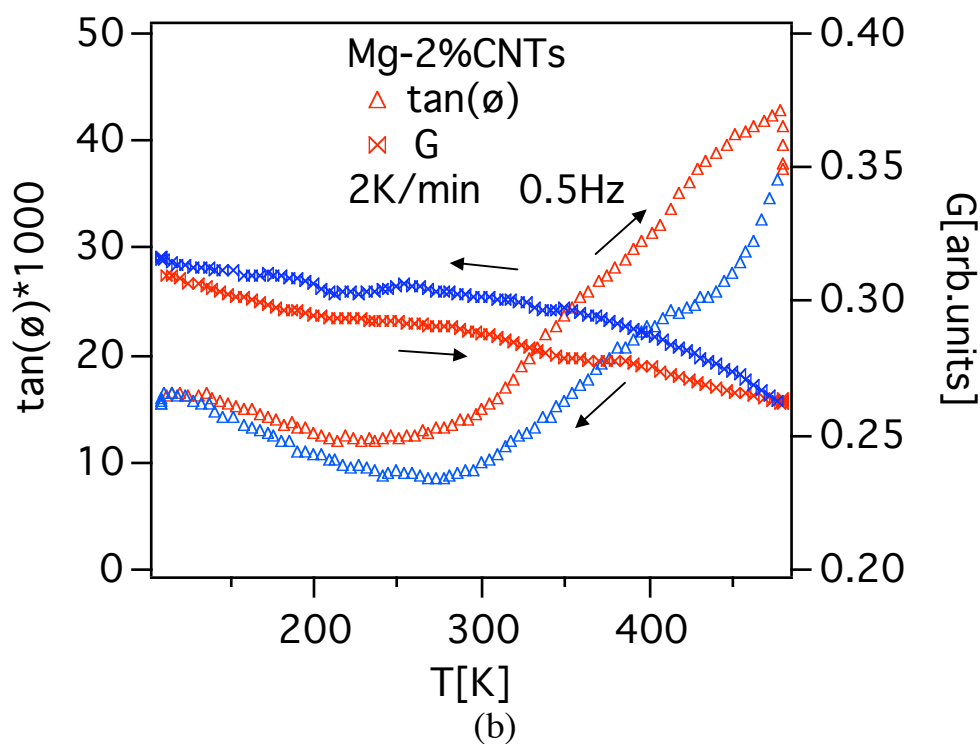
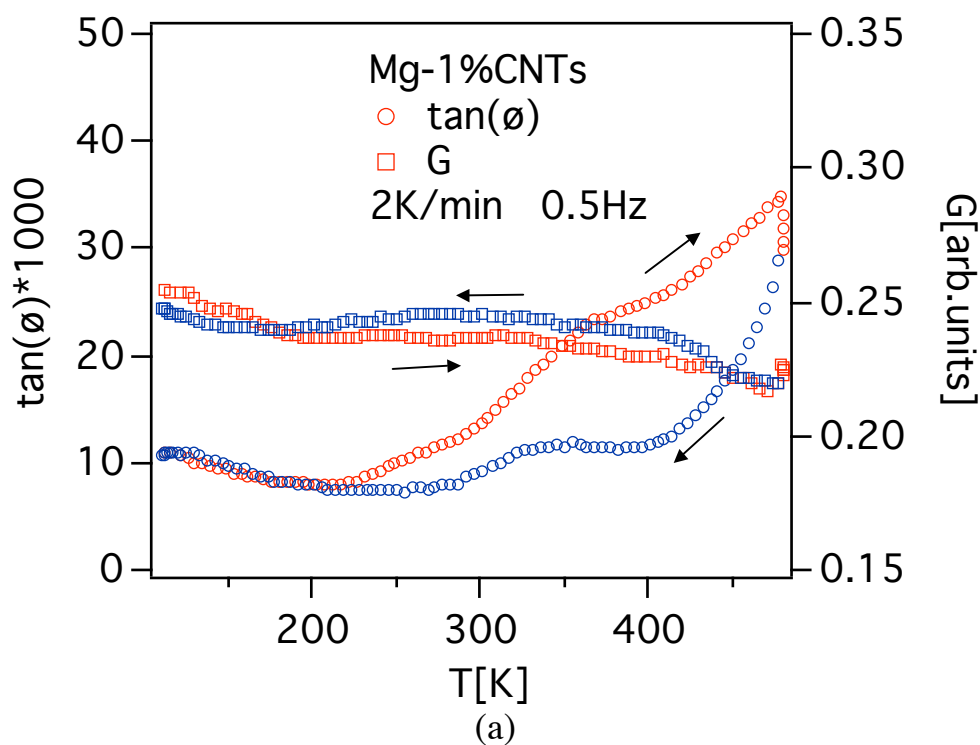


**Fig. 5.2:** Mechanical loss and shear modulus as a function of temperature measured: (a) in Mg-1%CNTs and (b) in Mg-2%CNTs,  $\dot{T} = 2 \text{ K/min}$ ,  $f = 0.5 \text{ Hz}$ ,  $\varepsilon = 10^{-5}$ .

The tensile curve accounts for a sound material with ultimate tensile stress of 149 MPa and elongation of 3 %. This allows one to conclude that the processing route was good

Fig. 5.2 a and b display the mechanical loss as well as the shear modulus (arbitrary units) as a function of temperature in Mg-1%CNTs and Mg-2%CNTs composites, respectively. The spectra were obtained during the first thermal cycle for each material. Temperature variation rate of 2 K/min, oscillation frequency of 0.5 Hz and strain amplitude of  $\varepsilon = 10^{-5}$  were employed during the measurements. In both composites, a peak is notable in the mechanical loss spectra between 300 K and 400 K. Annealing at 480 K for 10 minutes leads to a decrease in the mechanical loss and an increase in the shear modulus. Upon cooling the mechanical loss peak is better resolved with respect to the exponential background, especially in the case of 1 % CNTs (Fig. 5.2 a), where the mechanical loss decreases more significantly after annealing. Comparison of the shear modulus of the two composites shows that Mg-2 % CNTs possesses a higher shear modulus. Indeed a larger quantity of carbon nanotubes could lead to a higher shear modulus.

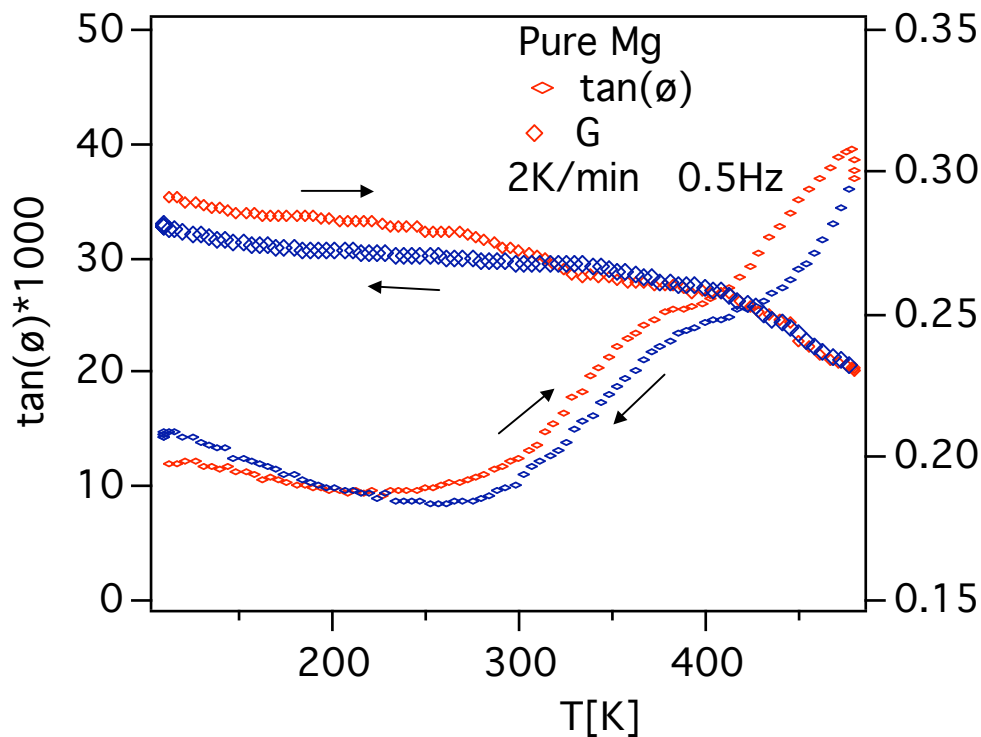


**Fig. 5.3:** Mechanical loss and shear modulus as a function of temperature measured in pure

$$\text{Mg, } \dot{T} = 2 \text{ K/min, } f = 0.5 \text{ Hz, } \varepsilon = 10^{-5}.$$

For comparison a plate of un-reinforced magnesium was processed by sintering commercial pure magnesium powders (99.8 %). Mechanical loss spectrum of this pure Mg specimen is presented in Fig. 5.3. The spectrum is similar to the ones measured in the two Mg reinforced with CNTs composites (Fig. 5.2 a, b). Pure Mg also exhibits a mechanical loss peak and a hysteresis between heating and cooling in both mechanical loss and shear modulus spectra. However, the hysteresis is much smaller, compared to that in the Mg-CNTs composites. Fig. 5.4 shows the mechanical loss spectra measured in the three materials, while the effect of CNTs on the shear modulus can be observed in Fig. 5.5. It is noted that 2 % CNTs increase the shear modulus by about 14 % at 480 K with respect to pure Mg. The shear modulus in Mg-1%CNTs is even lower than that in pure Mg, probably due to processing problems.

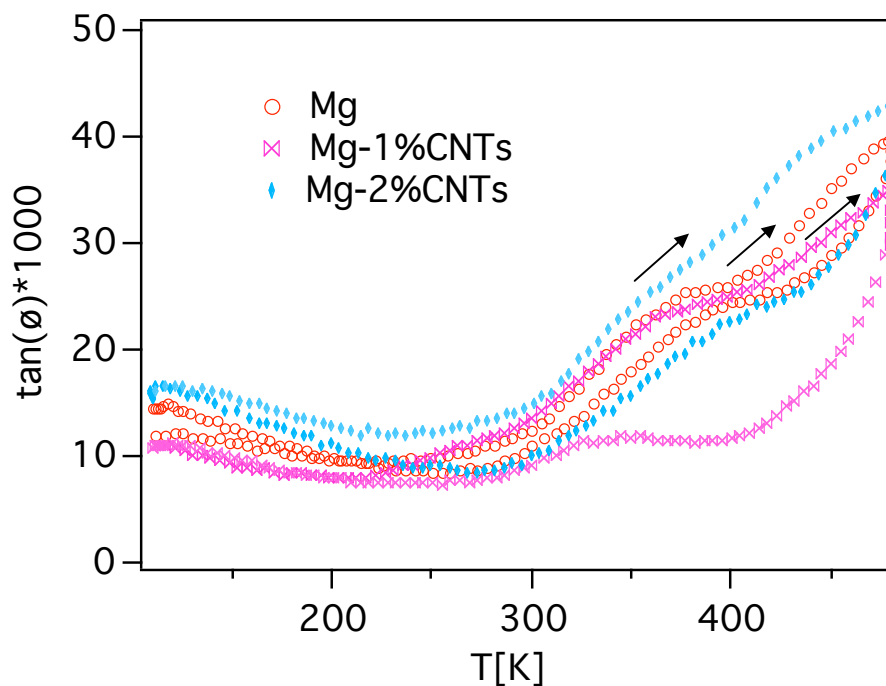


**Fig. 5.4:** Mechanical loss as a function of temperature measured in pure Mg, Mg-1%CNTs and Mg-2%CNTs.  $\dot{T} = 2 \text{ K/min}$ ,  $f = 0.5 \text{ Hz}$ ,  $\varepsilon = 10^{-5}$ .

The hysteresis observed in the mechanical loss spectra during the first thermal cycle can be explained as follows. Upon first heating, the dislocations are relatively free leading to a high level of mechanical loss. Annealing at 480 K favours the impurity migration towards



the dislocations. Then the density of pinning centres on the dislocation loops increases reducing the dislocation mobility and consequently the mechanical loss. A lower mechanical loss and higher shear modulus are measured during the subsequent cooling.

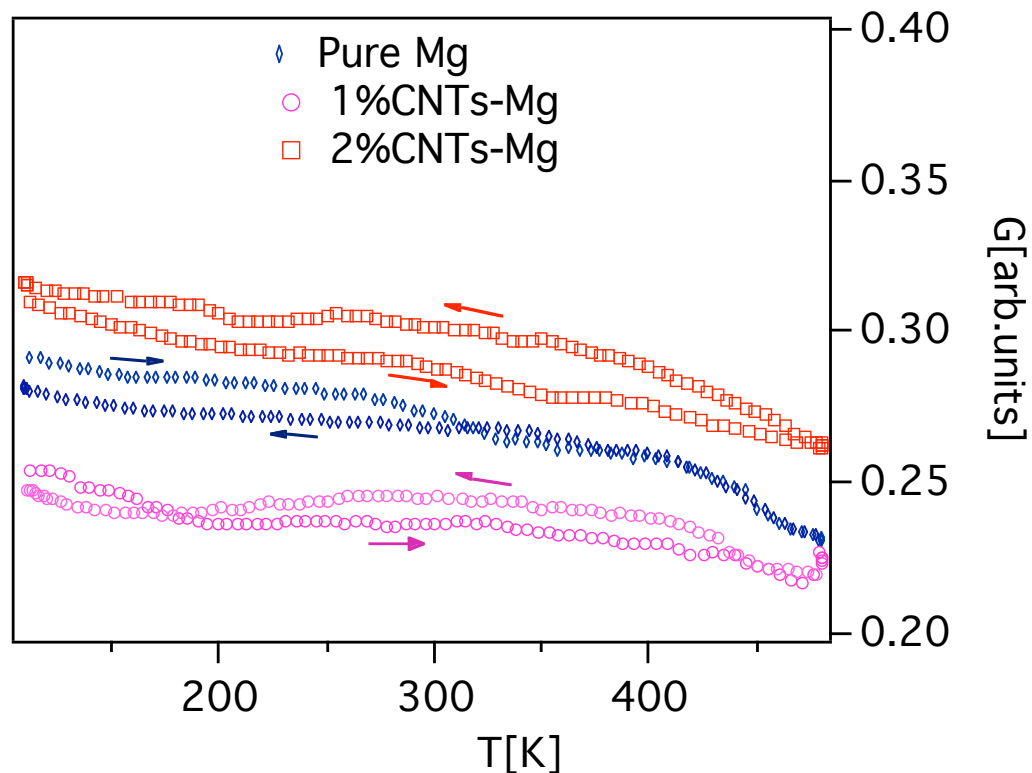


**Fig. 5.5:** Shear modulus as a function of temperature measured in pure Mg, Mg-1%CNTs and Mg-2%CNTs,  $\dot{T} = 2 \text{ K/min}$ ,  $f = 0.5 \text{ Hz}$ ,  $\varepsilon = 10^{-5}$ .

## 5.2 Effect of thermal cycles with different temperature variation rates

Mechanical loss and shear modulus spectra obtained in Mg reinforced with 1 % CNTs and 2 % CNTs composites as well as in pure Mg have been displayed in Figs 5.2 to 5.5. The results are as received under the same experimental conditions. In order to study the response to thermal cycling, more thermal cycles with the same or different  $\dot{T}$  have been performed in both Mg-2%CNTs and Mg-1%CNTs composites.

### 5.2.1 Mg-2%CNTs

Two continuous thermal cycles with the same experimental conditions have been performed in Mg-2%CNTs composites. Fig. 5.6 shows the mechanical loss and shear modulus spectra obtained with  $\dot{T} = 2$  K/min and  $f = 0.5$  Hz.

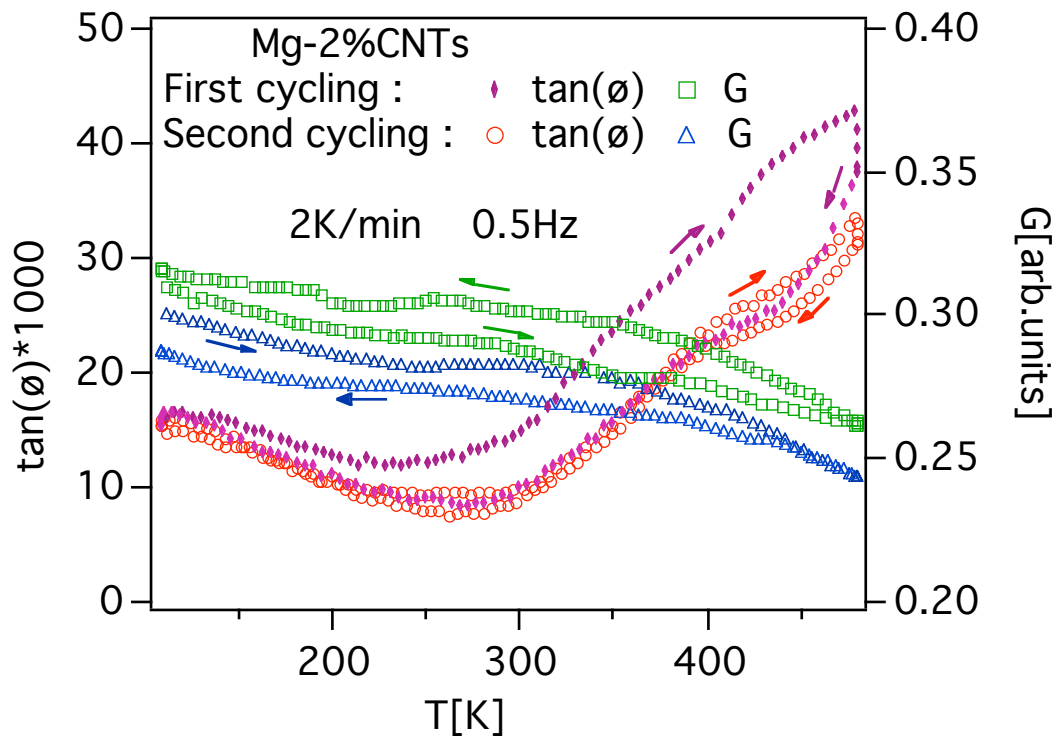


**Fig. 5.6:** Mechanical loss and shear modulus as a function of temperature measured in Mg-2%CNTs during two continuous thermal cyclings.  $\dot{T} = 2$  K/min,  $f = 0.5$  Hz,  $\varepsilon = 10^{-5}$ .

The large thermal hysteresis observed in the mechanical loss spectrum during the first thermal cycle diminishes significantly during the second thermal cycle. Almost the same level of mechanical loss spectrum is observed upon cooling and upon heating during the second cycle. Corresponding to the absence of the large hysteresis in the mechanical loss spectrum during the second thermal cycle, the relative height of the shear modulus curve is inverted. In the first cycling, the shear modulus spectrum is higher upon cooling than upon heating, while it is an opposite case during the second cycling. Moreover, the shear modulus during second cycling is lower (Fig. 5.6).

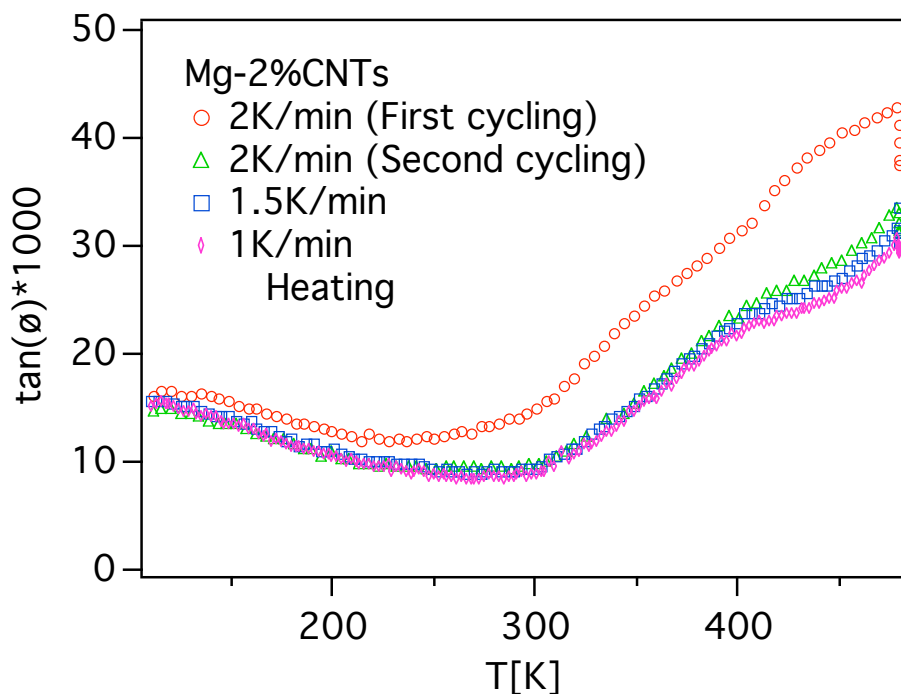


**Fig. 5.7:** Mechanical loss as a function of temperature measured in Mg-2%CNTs upon heating during different thermal cycles.  $\dot{T} = 2 \text{ K/min}, 1.5 \text{ K/min}, 1 \text{ K/min}, f = 0.5 \text{ Hz}, \varepsilon = 10^{-5}$ .

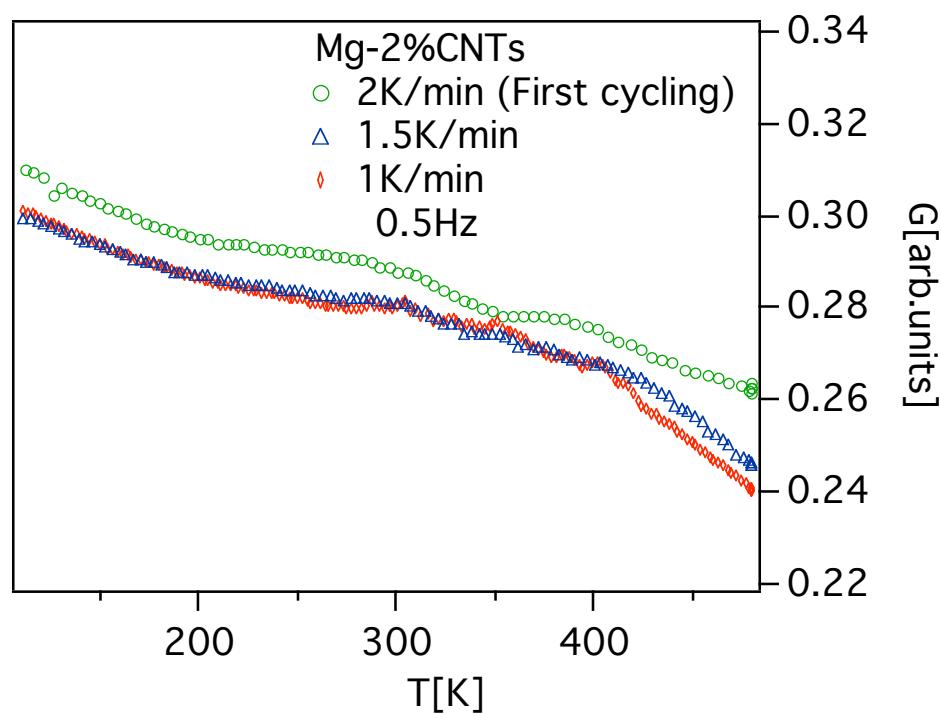


**Fig. 5.8:** Shear modulus as a function of temperature measured in Mg-2%CNTs during heating.  $\dot{T} = 2 \text{ K/min}, 1.5 \text{ K/min}, 1 \text{ K/min}, f = 0.5 \text{ Hz}, \varepsilon = 10^{-5}$ .

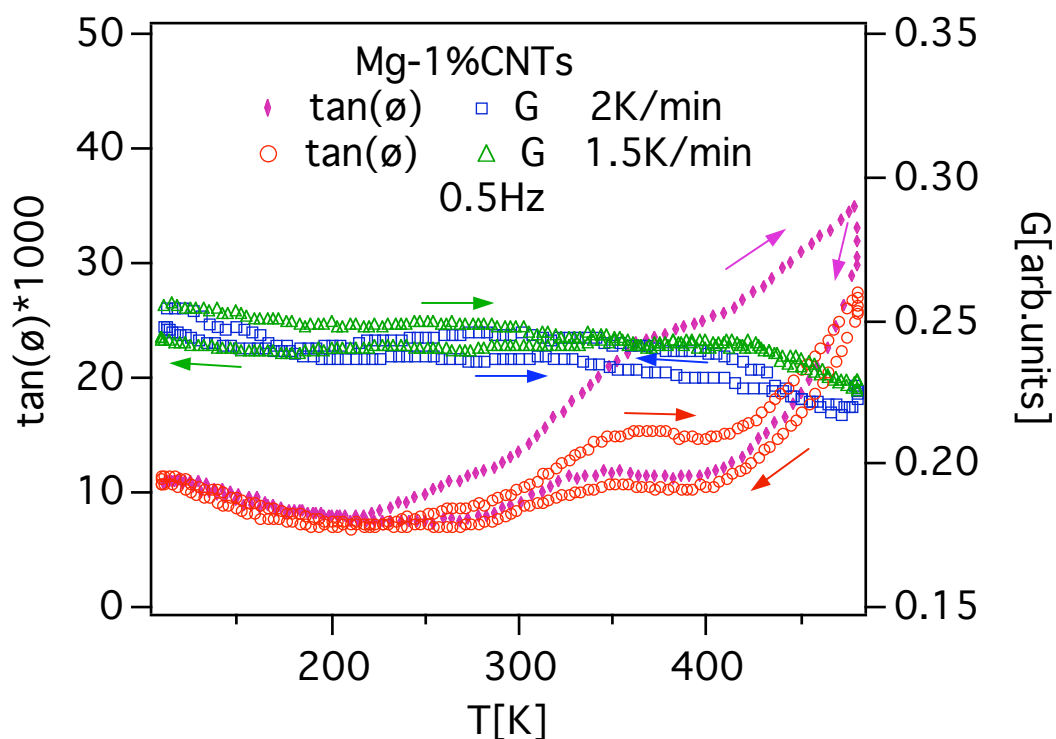
Mechanical loss spectra were also measured under different temperature variation rates. Fig. 5.7 presents the mechanical loss curves obtained upon heating during four thermal cycles with frequency of 0.5 Hz and temperature variation rate of 2 K/min, 1.5 K/min or 1 K/min, respectively. It is observed that after the first cycling, the spectrum becomes approximately stable, with a slight decrease at high temperature with increasing the number of cycling or decreasing the  $\dot{T}$ .

The evolution of shear modulus between different thermal cycles at different heating rate is shown in Fig. 5.8. It is observed that the shear modulus decreases at high temperature when increases the number of cycles (or when  $\dot{T}$  decreases). The spectra displayed in Fig. 5.6, 5.7 and 5.8 show that after the first heating, both mechanical loss and shear modulus are stable and depend weakly on  $\dot{T}$  ( $\dot{T}$  effect is weak in these composites).

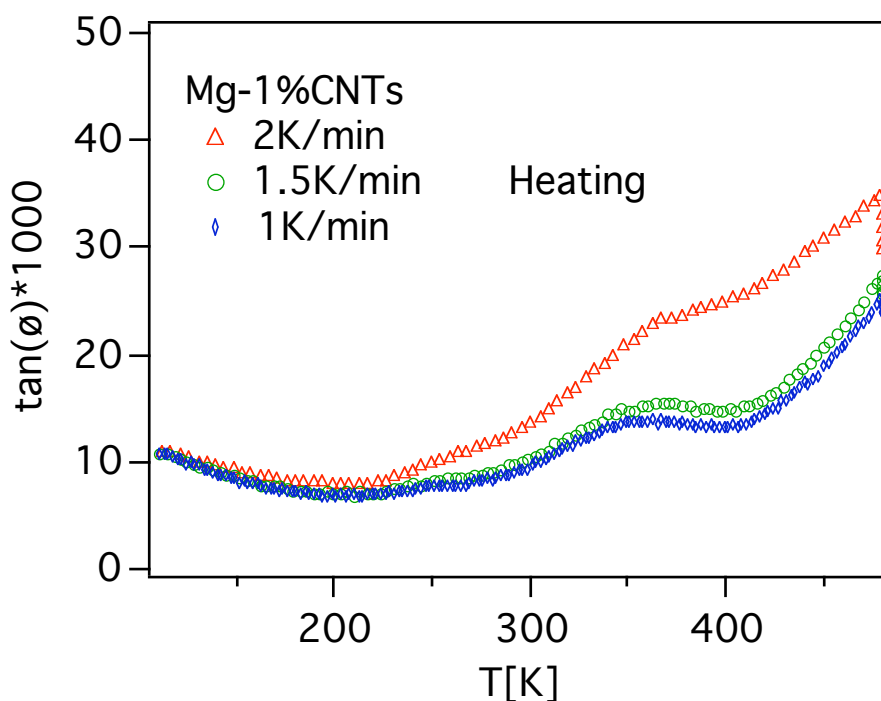
## 5.2.2 Mg-1% CNTs

Fig. 5.9 shows the mechanical loss and shear modulus behaviour of Mg-1% CNTs when subjected to thermal cycling with  $f = 0.5$  Hz and  $\dot{T} = 2$  K/min or 1.5 K/min. By comparison with the case of 2% CNTs, similar variations in the mechanical loss or in the shear modulus are observed. The evolution of mechanical loss and shear modulus spectra upon heating during three thermal cycles is displayed in Fig. 5.10 and Fig. 5.11, respectively.

Fig. 5.10 shows that the evolution of mechanical loss spectrum with the number of thermal cycles in Mg-1% CNTs resembles the case of 2 % CNTs (Fig. 5.7): after the first thermal cycle, mechanical loss has almost the same value in the low temperature range but slight decrease at high temperature upon heating during the subsequent cycles. The shear modulus measured upon the second heating is slightly higher than that in the subsequent thermal cycle over the whole measurement temperature range.



**Fig. 5.9:** Mechanical loss and shear modulus as a function of temperature measured in Mg-1%CNTs during two continuous thermal cyclings.  $\dot{T} = 2 \text{ K/min}$ ,  $1.5 \text{ K/min}$ ,  $f = 0.5 \text{ Hz}$ ,  $\varepsilon = 10^{-5}$ .



**Fig. 5.10:** Mechanical loss as a function of temperature measured in Mg-1%CNTs during heating.  $\dot{T} = 2 \text{ K/min}$ ,  $1.5 \text{ K/min}$ ,  $1 \text{ K/min}$ ,  $f = 0.5 \text{ Hz}$ ,  $\varepsilon = 10^{-5}$ .

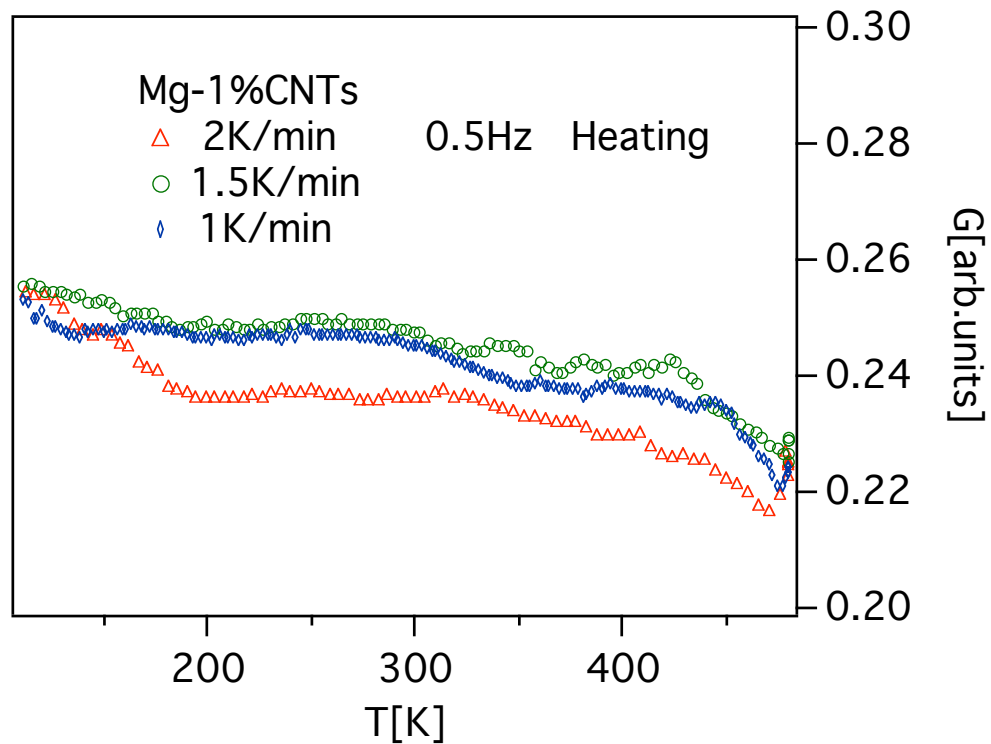


**Fig. 5.11:** Shear modulus as a function of temperature measured in Mg-1%CNTs.  $\dot{T} = 2$  K/min, 1.5 K/min, 1 K/min,  $f = 0.5$  Hz.

### 5.2.3 Summary

As presented in §5.2.1 and § 5.2.2, in two Mg-CNTs composites, both mechanical loss and shear modulus become relatively stable after the first heating. In the subsequent heatings, in Mg-2%CNTs, the mechanical loss spectra overlaps in a large temperature range, with a slight decrease at high temperature when increasing the number of cycles. This decrease in mechanical loss accompanies a slight decrease in the shear modulus.

The peak observed in damping spectra in three materials is not well resolved with respect to the exponential background. Thus activation enthalpy will be calculated using the master curve method.

### 5.3 Activation enthalpy

Isothermal measurements were performed in Mg-2%CNTs. Fig. 5.12 shows the mechanical loss and the shear modulus as a function of frequency in a logarithmic scale, obtained at 390 K (near the peak temperature of 413 K): mechanical loss decreases and shear modulus increases with increasing frequency.

Similar isothermal measurements were performed at different temperatures. The corresponding mechanical loss spectra are shown in Fig. 5.13. Mechanical loss increases and a shift of the curves towards higher frequency is observed with increasing the temperature of measurements. This indicates that the relaxation mechanism is thermally activated. The activation enthalpy can be derived from these isothermal measurements.

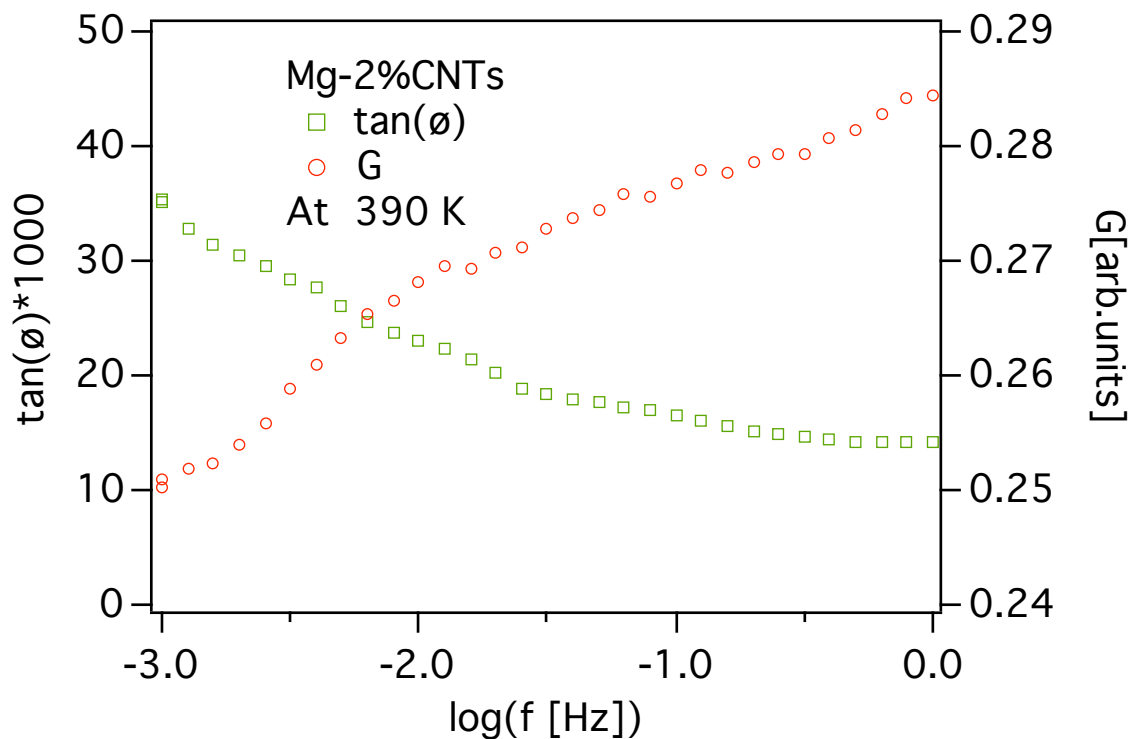


**Fig. 5.12:** Isothermal measurement of mechanical loss and shear modulus as a function of frequency (in logarithmic scale) performed at 390 K.

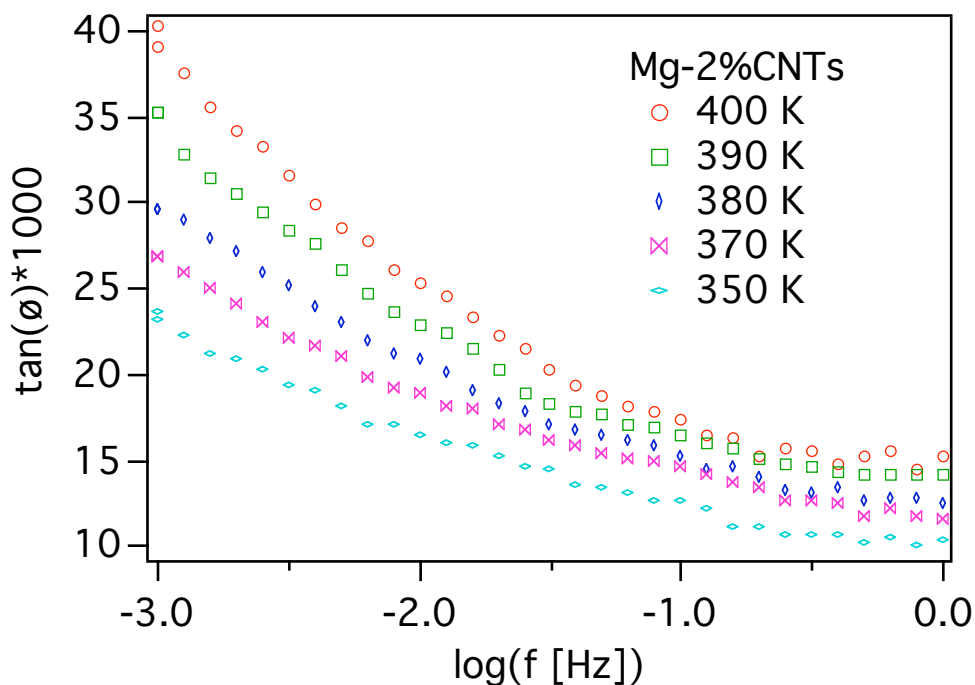


**Fig. 5.13:** Isothermal measurements of mechanical loss as a function of frequency (in logarithmic scale) performed at 400 K, 390 K, 380 K, 370 K and 350 K.

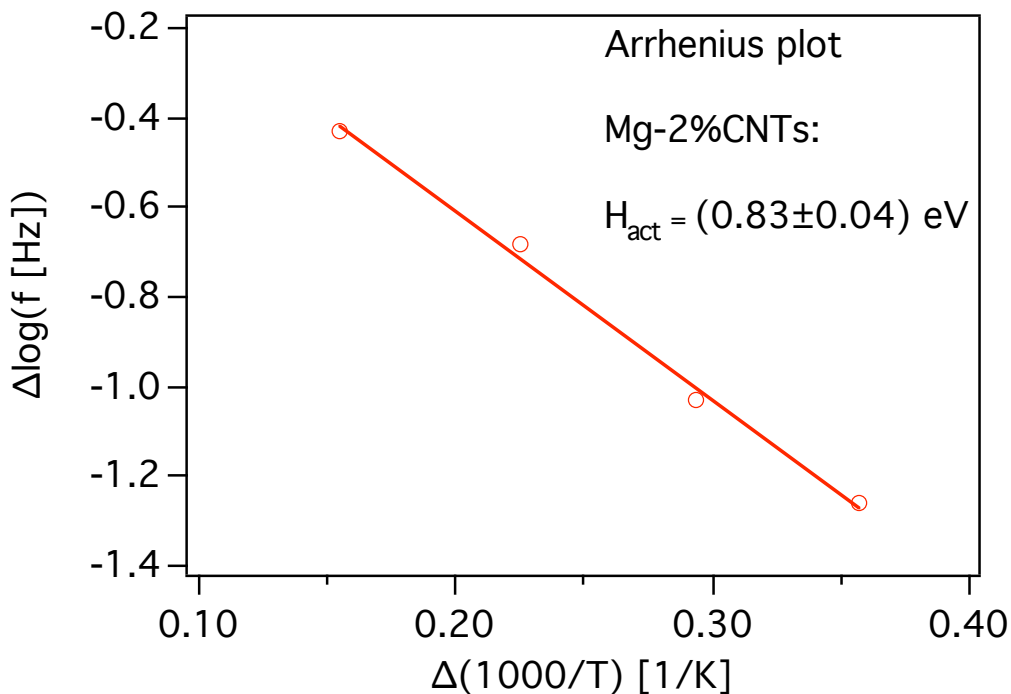


**Fig. 5.14:** Arrhenius plot. Shifts were made in the entire mechanical loss spectra with respect to the spectrum measured at 400 K.



In the framework of the master curve method, shifting should be made along the  $\Delta \log(f)$ -axis, in Fig. 5.13, till two isothermal spectra measured at different temperatures superimpose. Plotting the shifts of frequency,  $\Delta \log(f)$ , as a function of the variation of the inverse of temperatures,  $\Delta(1/T)$ , gives a straight line (Arrhenius plot, see Fig. 5.14.) The slope of the straight line yields the activation enthalpy as 0.83 eV.

However, the limit relaxation time  $\tau_0$  cannot be derived directly by this method from Fig. 5.14. It can be calculated using the Arrhenius law at the peak position. Then

$$\omega\tau = \tau_0 \cdot e^{H_{act}/kT_p} = 1 \quad (5.1)$$

In Fig. 5.7, one observes a stable peak in the spectra obtained upon heating during different cycles after the first one. The peak temperature,  $T_p$ , is 413 K. By inserting  $T_p$ , the measurement frequency ( $f = 0.5\text{Hz}$ ) and the activation enthalpy obtained from Fig 5.14 into equation (5.1), a limit relaxation time of  $\tau_0 = 2.3 \times 10^{-11}$  s can be calculated. This is reasonable for dislocation relaxation.

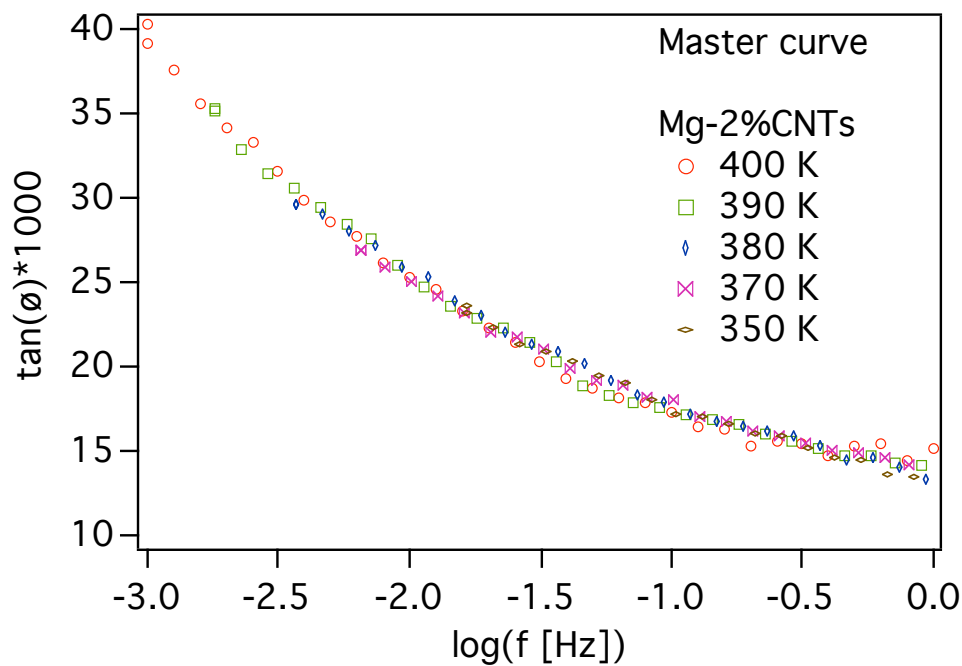


**Fig. 5.15:** Master curve obtained in Mg-2%CNTs.

A master curve (Fig. 5.15) can be obtained by coinciding the spectra in Fig 5.13 along the log (f)-axis. Together with the associated activation enthalpy, the master curve contains the same information as all the spectra shown in Fig. 5.13.

## 5.4 Theoretical modelling

The studied CNT-reinforced Mg composites and pure Mg show a similar mechanical loss spectrum composed of a relaxation peak and an exponential background (Fig. 5.2 and 5.3). The shape of these spectra resembles the graphs (Fig. 3.8) calculated from Schaller's model [93]. Thus the mechanical loss in these Mg based materials could be due to dislocations, which drag solute atoms in the solid solution. The solute atom mobility depends on temperature via the diffusion coefficient

$$D = D_0 e^{-E_{act}/kT} \quad (5.2)$$

where  $D_0$  is a constant,  $E_{cat}$  activation energy. Around the peak temperature, all the solute atoms do not move cooperatively and then the length of the dislocation loops (Equation (3.43)) depends on temperature:

$$l = l_0 (1 + \lambda e^{-E_{act}/kT}) \quad (5.3)$$

where  $\lambda = \alpha D_0$ . For taking into account the efficiency of diffusion to increase the dislocation loop length, one replaces  $E_{act}$  with  $\nu E_{act}$ , where  $\nu$  is a fitting coefficient. Then

$$l = l_0 (1 + \lambda e^{-\nu E_{act}/kT}) \quad (5.4)$$

Apparently, the relaxation peak observed experimentally is asymmetrical and broader than a Debye peak. As described in §3.2.1.2 II, this can be attributed to a continuous distribution in the relaxation time  $\tau$ . Let the pre-exponential factor  $\tau_0$  be constant, equal to the calculated value,  $2.26 \times 10^{-11}$  s, but the activation enthalpy varying with a variable  $\xi$

continuously. Using the string model and combining equations (3.37) and (3.42), the mechanical loss can be expressed as

$$\tan \phi = \frac{\Lambda l_0^2}{6} \cdot (1 + \lambda e^{-vE_{act}/kT})^2 \cdot \int_{\xi_1}^{\xi_2} \frac{\omega \tau_0 \cdot e^{\xi E_{act}/kT}}{1 + \omega^2 \tau_0^2 \cdot e^{2\xi E_{act}/kT}} d\xi \quad (5.5)$$

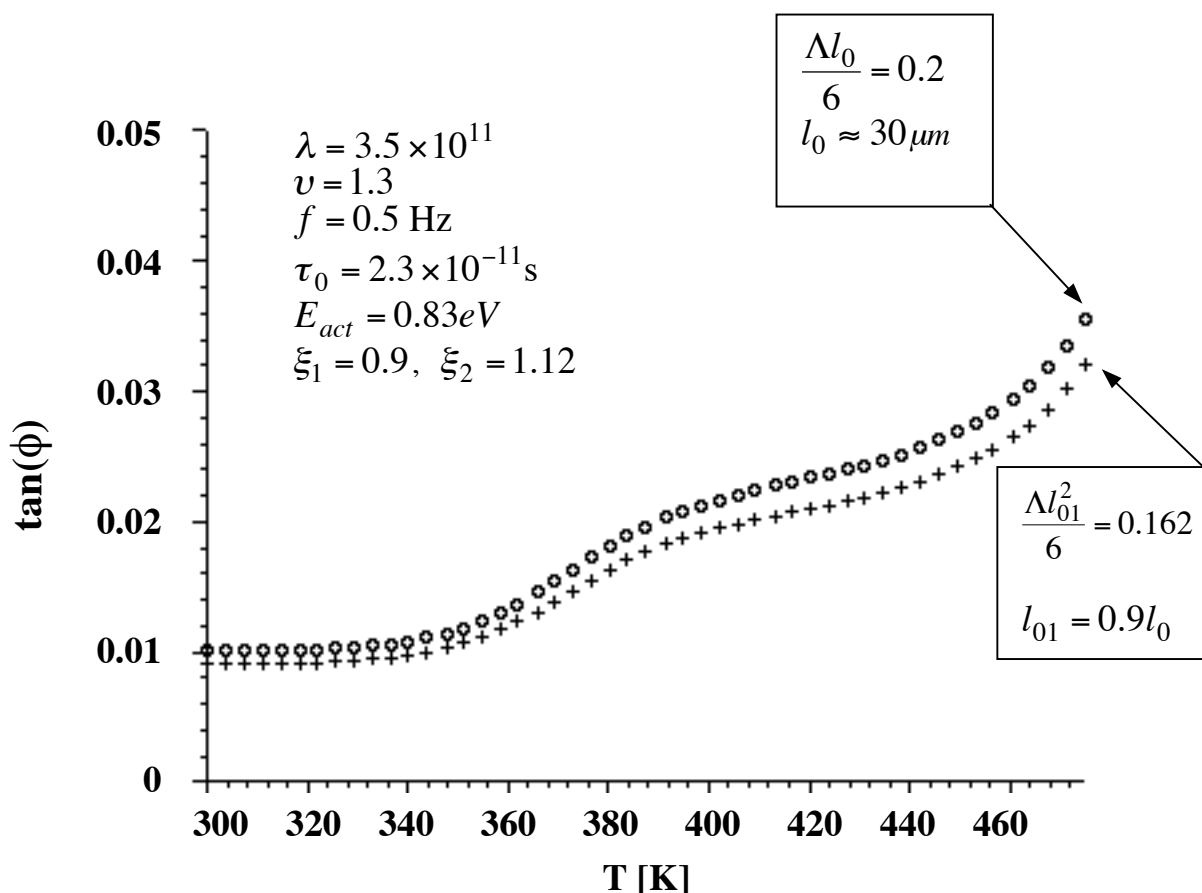


**Fig. 5.16:** Mechanical loss as a function of temperature between 300 K and 480 K calculated from the model of dragging of solute atoms by dislocations. Two curves correspond to dislocation mean length  $l_0 \approx 30 \mu\text{m}$  and  $l_{01} = 0.9 l_0$ , respectively. The shorter length is due to pinning of dislocation by solute atoms after annealing.

In addition, one should take into account the mechanical loss background. Thus, by adding a term for this background,  $\tan(\phi)_{bgd}$ , equation (5.5) can be rewritten as

$$\tan(\phi) = \tan(\phi)_{bgd} + \frac{\Lambda l_0^2}{6} \cdot (1 + \lambda e^{-\nu E_{act}/kT})^2 \cdot \int_{\xi_1}^{\xi_2} \frac{\omega \tau_0 \cdot e^{\xi E_{act}/kT}}{1 + \omega^2 \tau_0^2 \cdot e^{2\xi E_{act}/kT}} d\xi \quad (5.6)$$

From the experimental results shown in Fig. 5.2 b, one finds that the background is equal to 0.01. By choosing proper values of  $\Lambda l_0^2/6$ ,  $\lambda$ ,  $\nu$ ,  $\xi_1$ , and  $\xi_2$ , the curves were plotted from the equation (5.6) as shown in Fig. 5.16. The theoretical spectra in figure 5.16 are very close by the experimental curves (Fig 5.3 and 5.6, second thermal cycle). This shows that the model is correct. High temperature mechanical loss in Mg is due to dragging of the solute atoms by dislocations. Reinforcing Mg by carbon nanotubes, which cannot move like the other solute atoms at high temperature, would be positive to improve creep resistance of Mg-based alloys.

## 5.5 Conclusion

Mg matrix reinforced with 1% CNTs or 2% CNTs composites have been processed by sintering. The damping of these composites remains high, comparable to that of pure Mg, and the  $\dot{T}$  effect is negligible. These are due to the low percentages of carbon nanotubes and their tiny size, respectively. A large hysteresis is observed during the first thermal cycle. However, it diminishes during the subsequent cycles. This has been attributed to the migration of impurities such as solute atoms, which subsequently pin dislocations in the matrix, during the first annealing at 480 K. Both Mg-1%CNTs and Mg-2%CNTs as well as pure Mg all exhibit a relaxation peak in the damping spectrum. The peak is not well-resolved from the exponentially increasing background. The peak has been simulated by theoretical modelling. It is found that the non-well-resolved peak is due to the restoring force weakening, which is interpreted as due to the thermally activated statistic jumps of solute atoms. Comparing to pure Mg, the shear modulus increases in Mg-2%CNTs, but decreases in Mg-1%CNTs. Lower interface strength may be responsible for this significant decrease in the case of 1% CNTs.

# Chapter 6

## General discussions

---

### 6.1 Microstructures of the developed bulk CNTs - based composites

The aim of this work was to develop processing routes for reinforcing light metal matrix with carbon nanotubes, as well as to study the mechanical properties of these new MMCs. Aluminium alloys, Al-4%Cu-1%Mg-0.5%Ag (WFA), and pure magnesium were employed as matrices, while catalytic multi-wall carbon nanotubes (MWCNTs) synthesized by CVD were expected to play a role of modifiers of the SAFFIL-matrix interface and/or reinforcements in the composites. WFA-25%SAFFIL-CNTs and Mg-25%SAFFIL-CNTs were processed by infiltration, whereas two Mg-CNTs composites with different proportion of carbon nanotubes, 1%CNTs or 2%CNTs, were fabricated by sintering.

All of the four studied composites show a fine microstructure. The two Mg-CNT composites are characterized by a locally homogeneous distribution of the carbon nanotubes in Mg and the nanotubes remain in a good form (not damaged). In WFA-25%SAFFIL-CNTs and Mg-25%SAFFIL-CNTs, SAFFIL fibres disperse homogeneously in the matrix throughout the whole composites, while carbon nanotubes are not visible. The carbon nanotubes in these two composites could be completely embedded in the matrix. Therefore it is not easy to find them in a random fracture surface. On the contrary, carbon nanotubes could stay between the Mg grains in the Mg-CNTs composites, only partially embedded inside the grains, because the diffusion between the Mg grains is limited during sintering due to the oxide layer of the

Mg grains. Thus when breaking the specimens by bending, the fractures tend to take place along the grain boundaries. Consequently, a lot of carbon nanotubes are observable by Scanning Electron Microscopy along the fracture surface.

## 6.2 The impacts of CNTs on the elastic and anelastic properties of the CNTs-based composites

### 6.2.1 Impacts of CNTs on Young's modulus and shear modulus

Except for Mg-1%CNTs, all other three studied CNT-based composites have shown a significant increase in Young's and shear modulus, compared to the corresponding CNT-free materials, respectively (Table 6.1). This means that catalytic multi-wall carbon nanotubes can act as reinforcements in light metallic matrix such as Al alloys or pure Mg, with or without a second phase of reinforcements such as Al<sub>2</sub>O<sub>3</sub> SAFFIL fibres. The methods employed in this work, infiltration and powder metallurgy, are then efficient for processing Al or Mg matrix reinforced with SAFFIL fibres, coated with CNTs by CVD, or Mg reinforced with CNTs composites, meaning that a strong and effective interface bonding between CNTs and the matrix has been established so that the loads can be transferred from the matrix to the carbon nanotubes.

Material	Density ( $\times 10^3 \text{ kg/m}^3$ )	Young's modulus E (GPa)	Specific modulus	$(G_{\text{CNT}}-G)/G$ (%) (in arbitrary unit)
WFA-25%SAFFIL+CNTs	2.8	83.5	29.8	3.5 at 480 K
WFA-25%SAFFIL	2.2	65.5	29.8	
Mg-25%SAFFIL+CNTs	2.2	76.4	34.7	17 at 500 K
Mg-25%SAFFIL	2.1	56.7	27.0	
Mg-2%CNTs	1.7	38.6	22.7	15 at 480 K
Mg-2%CNTs coated	1.7	38.3	22.5	
Mg	1.7	35.3	20.8	
Steel	7.9	210	26.6	

**Table 6.1:** Density, Young's modulus, specific modulus and increase in shear modulus due to CNTs in different materials.

The enhancement in elastic modulus indicates that growing CNTs on the surface of SAFFIL fibres and heat treatment of CNTs can help to achieve an efficient CNT-matrix interface bonding. In the former, SAFFIL fibres could act as a structure holding the nanotubes, which were dispersed throughout the whole preform during their growth in the CVD reactor. In this case, the space between individual nanotubes is larger than in the case without the support of SAFFIL fibres. Thus during infiltration of such a preform of SAFFIL fibres coated with CNTs, the molten metal could go through the inter space between the nanotubes and more contact between their surface and the molten metal was created. Consequently, the CNTs are embedded in the matrix successfully and homogeneously. It overcomes the drawback caused by the poor wettability of the nanotubes by Al alloys or Mg as well as by the intermolecular Van-der-Waals interactions between the nanotube, thus resulting in the formation of aggregates. As a matter of fact, this drawback appeared as CNTs were gathering together in the centre of the composite with uncompleted infiltration of the CNTs. In the second way, heat treatment oxidizes the surface of the nanotubes. This is helpful for building a stronger interface between CNTs and Mg. However, in Mg-1%CNTs, the Young's and shear modulus were found to be lower than that of pure Mg. This may be attributed to the remaining porosity along the interfaces. Also, in addition to the modification of the CNT surfaces, hot isostatic pressing was utilized as a second step in processing Mg-2%CNTs for eliminating pores and providing better interfaces in the Mg-CNTs composites. The lower density of WFA-25%SAFFIL (Table 6.1), comparing with WFA-25%SAFFIL-CNTs, may be due to more interface porosity, which forms in this composite during the processing. This means that multi-wall carbon nanotubes could be helpful for establishing a better interface between SAFFIL fibres and the matrix (WFA), with less porosity. On the other hand, the less good interface quality in WFA-25%SAFFIL could be partially responsible for the lower Young's modulus. The methods of infiltration and powder metallurgy could be used with profit in processing and scaling up the products.

## 6.2.2 Impacts of CNTs on damping capacity

After having an over look at the mechanical loss spectra of the four developed CNTs-based composites, one finds that carbon nanotubes have evident impacts on the damping capacity of the composites. For example, CNTs can enhance the mechanical loss of the composites in a certain temperature range during cooling: between 270 K and 160 K in WFA-

25%SAFFIL-CNTs (Fig. 4.2), between 450 K and 130 K in Mg-25%SAFFIL-CNTs (Fig. 4.11) and between 230 K and 110 K in Mg-2%CNTs (Fig. 5.4). In the two CNTs-based composites produced by infiltration, this enhancement has been attributed to the increase in the density of mobile dislocations due to the additional dislocation nucleation from the nanotube tips, located in the interface between SAFFIL fibres and matrix. The CNTs far away from the interface are also considered to behave as obstacles and pin dislocations. Thus the mobility of the dislocations is decreased. The model developed based on these hypotheses can explain the damping phenomena, which deviate from the cases without CNTs as analysed in chapter 4. In this model, the interfaces between nanotube walls and matrix are not taken into account as a dislocation source. Actually, some dislocations might be emitted from these interfaces and give a contribution to the dislocation density as well. However, this contribution would be negligible in both WFA-25%SAFFIL-CNTs and Mg-25%SAFFIL-CNTs composites, whereas it would be significant for the improvement of damping in Mg-2%CNTs between 230 K and 110 K during cooling, with respect to the damping spectrum in pure Mg.

Particularly, a large increased transient damping (Fig. 4.6 or Fig. 4.7) is induced in WFA-25%SAFFIL-CNTs composite due to CNTs. Although this is not analyzed in Mg-25%SAFFIL-CNTs, it could be expected that CNTs would result in a larger transient damping in Mg-25%SAFFIL-CNTs, compared to Mg-25%SAFFIL. The increase in transient damping indicates a softening in the interface between the WFA or Mg matrix and the SAFFIL fibres. Carbon nanotubes should be responsible for this interface softening then a resistance of fatigue.

### 6.2.3 Reinforcement size effect

The use of nano-sized reinforcements in MMCs aimed at reducing the thermal stresses, which are built at the ceramic-matrix interface due to the difference in the thermal expansion coefficients. In the case of classical reinforcements like short or long fibres ( $\text{Al}_2\text{O}_3$ , SiC or C) the thermal stresses can be relaxed by two ways: interface cracking or dislocation emission. Interface cracking is not good, because it leads to damage accumulation until fracture of the specimen. Emission of dislocations in the matrix, which has to be ductile in the



interface region, is a relaxation mechanism leading to a better behaviour with respect to thermal fatigue, especially if after first thermal cycles the dislocation network is stable.

In the present work, micro-sized reinforcements were the alumina SAFFIL short fibres, which have a diameter of about 3  $\mu\text{m}$  and length of about 100  $\mu\text{m}$ . During thermal cycling these reinforcements generate thermal stresses, which are responsible for a large transient maximum in damping observed upon cooling (Fig. 4.2): the so-called  $\dot{T}$  effect, which is the signature of the interface stress relaxation in MMCs by dislocation motion.

In the case of magnesium reinforced with carbon nanotubes, no  $\dot{T}$  effect has been observed at low temperature. This behaviour can be interpreted in two ways: fibre-matrix (nanotube-Mg) bonding is bad or thermal stresses are weak because of the reduced size of the reinforcements. First we can admit that the bonding between the CNTs and the magnesium matrix is rather good, because the CNTs are responsible for an increase in the elastic modulus of Mg: about 9% in the Young's modulus and 15 % in the shear modulus at 480 K for 2 % MWCNTs. As a consequence, we can consider the MWCNTs as reinforcements of the Mg matrix. Also as they do not give rise to a noticeable  $\dot{T}$  effect, they can be considered as no thermal stress generators. It is not unreasonable to admit that reducing the size of the reinforcing objects (particles or fibres) by a factor of ten or hundred will reduce the thermal stresses by this factor. Naturally for improving the modulus like in the case of SAFFIL fibres additions (here 25 vol % of fibres) the volumetric fraction of the CNTs has to be strongly increased. By taking into account the rule of mixtures and a configuration of the CNTs in parallel and in series, one can predict a Young's modulus of about 200 GPa for 50 vol% of CNTs in a Mg matrix. Naturally to achieve this challenge, one needs CNTs with a Young's modulus of about 800 GPa and also to improve the processing route to disperse successfully 50 % of CNTs in the metallic matrix. In this case, the resulting MMC will have a modulus as high as steel without the drawback to be very sensitive to thermal fatigue because of the high thermal stresses built at the interfaces.

### 6.3 Propositions for further research

The results obtained in WFA-25%SAFFIL-CNTs, Mg-25%SAFFIL-CNTs and Mg-2%CNTs have demonstrated that a substantial improvement in Young's modulus has been attained through small amounts of carbon nanotubes as reinforcing phase in the MMCs. In order to increase Young's modulus more, it would be better to replace the catalyst MWCNTs by other types of carbon nanotubes such as arc-discharged grown MWCNTs and catalyst/arc-discharged grown single wall or catalytic double wall nanotubes, which have a much higher Young's modulus. As scaling up arc-discharged grown nanotubes still encounters difficulties, using those nanotubes as reinforcing phase can be limited in processing small sized composites. On the other hand, Young's modulus can be enhanced by increasing the proportion of CNTs in the composites as proposed here above.

Wettability remains an obstacle in developing CNTs reinforced metal matrix composites. In this work the coated CNTs have been also applied and the Young's modulus is increased in Mg-2%CNTs coated by about 8.5%, compared to pure Mg. However, no useful amount of these coated carbon nanotubes was available for developing larger amount of composites. Therefore, scaling up the modified nanotubes would be an important step to improve mechanical properties of the MMCs with CNTs as the reinforcing phase. Using coated CNTs to replace the plain ones would be significant attempts.

Increasing the diffusion between pure magnesium grains would be a way to embed CNTs in Mg better so as to improve the CNTs-Mg interface bonding by powder metallurgy. In order to achieve this goal, pure Mg powders with thinner oxide surface layer would be helpful and experimental conditions should be modified. On the other hand, as the favourite size of the matrix is similar or smaller than that of reinforcement for better densification of a composite, smaller size of Mg grains is proposed.

# Conclusion

---

Metal matrix composites (MMCs) with carbon nanotubes (CNTs) as reinforcements have been developed. It has been shown that carbon nanotubes have positive impacts on these composites. Coating  $\text{Al}_2\text{O}_3$  SAFFIL fibres with CNTs before infiltration by the molten metal can substantially enhance the Young's and shear modulus. In the case of Al alloy (WFA)-25%SAFFIL-CNTs the Young's modulus was increased by 27.5 % and the shear modulus at 480 K by about 3.5 %, respectively. In the other case of Mg-25%SAFFIL-CNTs, an enhancement of 35 % in Young's modulus and of 17 % in shear modulus at 500 K was achieved. In Mg-2wt%CNTs processed by powder metallurgy, the Young's and shear modulus were increased by 9.3 % and 15 % (at 480 K), respectively.

It has then been shown that catalytic multi-wall carbon nanotubes act as modifiers of the interfaces between the SAFFIL fibres and Al alloys or Mg matrix. A better reaction of these interfaces to thermal stresses has been observed by detection of an additional damping. The nanotube tips situated in the SAFFIL-matrix interfaces act as local stress amplifiers enhancing dislocation emission and then relaxing thermal stresses sooner. A model has been developed to describe the mechanism of dislocation nucleation from the tips. The mechanical loss maximum during cooling in WFA-25%SAFFIL-CNTs and WFA-25%SAFFIL was theoretically simulated. The relatively higher values in dislocation density and activation enthalpy in WFA-25%SAFFIL-CNTs prove the hypothesis: dislocation nucleation by the nanotube tips located in the SAFFIL-matrix and additional pinning dislocation loops by

nanotubes located far away from the interface. In both WFA-25%SAFFIL-CNTs and Mg-25%SAFFIL-CNTs, the dependence of mechanical loss on the ratio  $\dot{T}/\omega$  is non-linear and it accounts then for the relaxation of thermal stresses by hysteretic dislocation motion (solid friction mechanism).

In Mg-1%CNTs and Mg-2%CNTs, the large hysteresis observed between damping spectra obtained upon heating and cooling during the first thermal cycle can be explained as due to the pinning of dislocations by impurities, which migrate towards the dislocation loops during annealing at 480 K. The damping spectra upon heating during the subsequent cycles remain approximately at the same level in each composite, with a slight decrease at high temperature. A relaxation peak superimposed on an exponential background has been observed in the mechanical loss spectra. Theoretical simulation shows that the relaxation peak is strongly bound to the exponential background, because the restoring force, which acts on the dislocation loop, weakens due to the thermally activated statistic jumps of the pinning solute atoms.

This work has shown the feasibility of processing bulk metal matrix composites using carbon nanotubes as interface modifiers and/or reinforcing phase.

# Bibliography

1. Mel M. Schwartz, *Composite Materials*, Volume **1**, (1997).
2. A. Evans, C.S. Marchi, A. Mortensen, *Metal matrix composites in industry, An introduction and a survey*, Kluwer Academic Publishers, Dordrecht/Boston/London, (2003).
3. S.Iijima, *Helical microtubules of graphitic carbon*, Nature, **354**, 56 (1991).
4. M. Cadek, B. Le Foulgoc, J. N. Coleman, V. Barron and W. J. Blau, *Mechanical and thermal properties of carbon nanotube reinforced polymer composites*, <http://dielc.kaist.ac.kr/nt02/abstracts/p167.shtml>
5. R. H. Baughman, A. A. Zakhidov, W. A. D. Heer, *Carbon Nanotubes--the Route toward Applications*, Science, **297**, 787 (2002).
6. M. Cadek, J. N. Coleman, V. Barron, K. Hedicke, W. J. Blau, *Morphological and mechanical properties of carbon-nanotube-reinforced semicrystalline and amorphous polymer composites*, Appl. Phys. Lett., **81**, 5123 (2002).
7. J. Sandler, M. S. P. Shaffer, T. Prasse, W. Bauhofer, K. Schulte, A. H. Windle, *Development of a dispersion process for carbon nanotubes in an epoxy matrix and the resulting electrical properties*, Polymer, **40**, 5967 (1999).
8. M. S. P. Shaffer, A. H. Windle, *Fabrication and Characterization of Carbon Nanotube/Poly (vinyl alcohol) Composites*, Adv. Mater, **11**, 937 (1999).
9. J. N. Coleman, K. P. Ryan, M. S. Lipson, A. Drury, M. Cadek, M. i. h. Panhuis, R. P. Wool, W. J. Blau, XVI. International winterschool/ Euroconference, Kirchberg/Tirol, Austria, **633**, 557 (2002).
10. D. Qian, E. C. Dickey, R. Andrews, T. Rantell, *Load transfer and deformation mechanisms in carbon nanotube-polystyrene composites*, Appl. Phys. Lett., **76**, 2868 (2000).
11. R.Z. Ma, J. Wu, B.Q. Wu, J. Liang, D. H. Wu, *Processing and properties of carbon nanotube-nano-SiC ceramic*, Journal of Materials Science, **33** (21), 5243 (1998)
12. X. Chen, J. Xia, J. Peng, W. Li, S. Xie, *Carbon-nanotube metal-matrix composites prepared by electroless plating*, Composites Science and Technology, **60**(2),301 (2000).

13. C. L. Xu, B. Q. Wei, R. Z. Ma, J. Liang, X. K. Ma, D. H. Wu, *Fabrication of aluminum-carbon nanotube composites and their electrical properties*. Carbon, **37**(5), 855 (1999).
14. H. W. Kroto, J. R. Heath, S. C. O'Brian, R. F. Curl, R. E. Smalley, *C-60-Buckminsterfullerene*, Nature **381**, 162 (1985).
15. Erik T. Thostenson, Zhifeng Ren, Tsu-Wei Chou, *Advances in the science and technology of carbon nanotubes and their composites: a review*, Composites Science and Technology, **61** 1899 (2001).
16. MS. Dresselhaus, G. Dresselhaus, PC. Eklund, *Science of fullerenes and carbon nanotubes*, San Diego:Academic Press, (1996 )
17. S. G. Louie, *Electronic Properties, Junctions, and Defects of Carbon Nanotubes*, *Top. Appl. Phys.*, **80**, 113 (2001)
18. W. Liang, M. Bockrath, D. Bozovic, J. H. Hafner, M. Tinkham, H. Park, *Fabry – Perot interference in a nanotube electron waveguide*, Nature, **411**, 665 (2001)
19. S. Frank, P. Poncharal, Z. L. Wang, W. A. de Heer, *Carbon nanotube quantum resistors*, Science, **280**, 1744 (1998).
20. PG. Collins, P. Avouris, *Nanotubes for electronics*, Scientific American, **283**(6), 62 (2000).
21. A. G. Rinzler, J. H. Hafner, P. Nikolaev, L. Lou, S. G. Kim, D. Tománek, P. Nordlander, D. T. Colbert, R. E. Smalley, *Unraveling nanotubes - field-emission from an atomic wire* Science, **269**, 1550 (1995).
22. J. - M. Bonard, T. Stöckli, F. Meier, W. A. de Heer, A. Chatelain, J.-P. Salvetat, L. Forró, *Field-Emission-Induced Luminescence from Carbon Nanotubes*, Phys. Rev. Lett., **81**, 1441 (1998).
23. M. M. J. Treacy, T. W. Ebbesen, J. M. Gibson, *Exceptionally high Young's modulus observed for individual carbon nanotubes*, Nature, **381**, 678 (1996).
24. E. W. Wong, P. E. Sheehan, C. M. Lieber, *Nanobeam Mechanics: Elasticity, Strength, and Toughness of Nanorods and Nanotubes*, Science, **277**, 1971 (1997).
25. M. R. Falvo, G. J. Clary, R. M. Taylor, II, V. Chi, F. P. Brooks, Jr, S. Washburn, R. Superfine, *Bending and buckling of carbon nanotubes under large strain*, Nature, **389**, 582 (1997).
26. M. S. Dresselhaus, G.Dresselhaus, K. Sugihara, I. L. Spain, H. A. Goldberg, *Graphite Fibers and Filaments*.Springer Ser. In Mater. Sci. 5 (Springer, Berlin, Heidelberg 1988).
27. J. -P. Slavetat, A. J. Kulik, J.-M. Bornard, G. A. D. Briggs, T. Stöckli, K. Méténier, S.

- Bonnamy, F. Béguin, N. A. Burnham, L. Forró, *Elastic Modulus of Ordered and Disordered Multiwalled Carbon Nanotubes*, *Adv. Mater.*, **11** (2), 161 (1999).
28. BI. Yakobson, C.J. Brabec, J. Bernholc, *Nanomechanics of carbon tubes: instabilities beyond linear response*, *Physical Review Letters*, **76** (14), 2511 (1996).
29. BI. Yakobson, G. Samsonidze, G. G. Samsonidze, *Atomistic theory of mechanical relaxation in fullerene nanotubes*, *Carbon*, **38** (11-12), 1675 (2000).
30. S. J. Tans, A. R. M. Verschueren, C. Dekker, *Room-temperature transistor based on a single carbon nanotube*, *Nature*, **393**, 49 (1998).
31. W. A. de Heer, A. Châtelain, D. Ugarte, *A carbon nanotube field-emission electron source*, *Science*, **270**, 1179 (1995).
32. W. A. de Heer, J.-M. Bonard, Kai Fauth, A. Chatelain, L. Forró, D. Ugarte, *Electron field emitters based on carbon nanotube films*, *Adv. Mater.*, **9**, 87 (1997).
33. Y. Saito, S. Uemura, *Field emission from carbon nanotubes and its application to electron sources*, *Carbon*, **38**, 169 (2000).
34. J. H. Hafner, C. L. Cheung, C. M. Lieber, *Growth of nanotubes for probe microscopy tips*, *Nature*, **398**, 761 (1999).
35. H. Dai, J. H. Hafner, A. G. Rinzler, D. T. Colbert, R. E. Smalley, *Nanotubes as nanoprobe tips in scanning probe microscopy*, *Nature*, **384**, 147 (1998).
36. J. Li, A. M. Cassell, H. J. Dai, *Carbon nanotubes as AFM tips: Measuring DNA molecules at the liquid/solid interface*, *Surf. Interface Anal.* **28**, 8 (1999).
37. Ray H. Baughman, Anvar A. Zakhidov, Walt A. de Heer, *Carbon Nanotubes—the Route Toward Applications*, *Science*, **297**, 787 (2002).
38. Z. Jia, Z. Wang, C. Xu, J. Liang, B. Wei, Wu Dehai, S. Zhu, *Study on poly (methyl methacrylate) / carbon nanotube composites*, *Materials Science and Engineering A*, **271**(1-2), 395 (1999).
39. V. Lordi, N. Yao. *Molecular mechanics of binding in carbon-nanotube-polymer composites*, *Journal of Materials Research*, **15** (12), 2770 (2000).
40. H. D. Wagner, O. Lourie, Y. Feldman, R. Tenne, *Stress - induced fragmentation of multiwall carbon nanotubes in a polymer matrix*, *Applied Physics Letters*, **72** (2), 188 (1998).
41. O. Lourie, H. D. Wagner, *Transmission electron microscopy observations of fracture of single-wall carbon nanotubes under axial tension*, *Applied Physics Letters*, **73** (24), 3527 (1998).
42. O. Lourie, H. D. Wang. *Evidence of stress transfer and formation of fracture clusters in carbon nanotube - based composites*, *Composites Science and Technology*, **59** (6),

- 975 (1999).
43. C. A. Cooper, R. J. Young, M. Halsall, *Investigation into the deformation of carbon nanotubes and their composites through the use of Raman spectroscopy*, Composites Part A: Applied Science and Manufacturing, **32** (34), 401(2001).
  44. X. Gong, J. Liu, S. Baskaran, Roger D. Voise, JS. Young, Surfactant-Assisted Processing of Carbon Nanotube/Polymer Composites, Chemistry of Materials, **12** (4) 1049 (2000).
  45. E. Flahaut, A. Peigney, Ch. Laurent, Ch. Marlière, F. Chastel, A. Rousset, *Carbon nanotube-metal-oxide nanocomposites: microstructure, electrical conductivity and mechanical properties*, Acta Materialia, **48** (14), 3803 (2000).
  46. A. Peigney, Ch. Laurent, E. Flahaut, A. Rousset, *Carbon nanotubes in novel ceramic matrix nanocomposites*, Ceramics International, **26** (6), 677 (2000).
  47. A. Peigney, Ch. Laurent, O. Dumortier, A. Rousset, *Carbon nanotubes- Fe-alumina nanocomposites. Part I: influence of the Fe content on the synthesis of powders*, Journal of the European Ceramic Society, **18** (14),1995 (1998).
  48. Ch. Laurent, A. Peigney, O. Dumortier, A. Rousset. *Carbon nanotubes-Fe-alumina nanocomposites. Part II: microstructure and mechanical properties of the hot-pressed composites*, Journal of the European Ceramic Society, **18** (14): 2005( 1998).
  49. A. Peigney, Ch. Laurent, A. Rousset. *Synthesis and characterization of alumina matrix nanocomposites containing carbon nanotubes*, Key Engineering Materials, **132-136**:743 (1997).
  50. W. Krätschmer, L. D. Lamb, K. Fostiropoulos, D.R.Huffman, *Solid C60: a new form of carbon*, Nature, **347**, 354 (1990).
  51. T.W. Ebbesen, P. M. Ajayan, *Large - scale synthesis of carbon nanotubes*, Nature, **358**, 220 (1992).
  52. D. S. Bethune, C. H. Klang, M. S. de Vries, G. Gorman, R. Savoy, J. Vazquez & R. Beyers, *Cobalt - catalysed growth of carbon nanotubes with single- atomic-layer walls*, Nature, **363**, 605 (1993).
  53. C. Journet, P. Bernier, *Production of carbon nanotubes*, Appl. Phys. A **67**, 1 (1998).
  54. S.Iijima, T. Ichihashi, *Single-shell carbon nanotubes of 1-nm diameter*, Nature, **363**, 603 (1993).
  55. A.Thess, R. Lee, P. Nikolaev, H. Dai, P. Petit, J. Robert, C. Xu, Y. H. Lee, S. G. Kim, A. G. Rinzler, D. T. Colbert, G. E. Scuseria, D. Tománek, J .E. Fisher, Smalley, *Crystalline Ropes of Metallic Carbon Nanotubes*, Science, **273**, 483 (1996).



56. Hugh O. Pierson, *HANDBOOK OF CHEMICAL VAPOR DEPOSITION (CVD), Principle Technology and Applications*, Noyes Publications, Park ridge, New Jersey, U.S.A. (1992).
57. Anthony C. Jones, Paul O'Brien, *CVD of Compound Semiconductors, Precursor Synthesis, Development and Applications*, VCH, (1997).
58. M. José. Yacamán, M. Miki-Yoshida, L. Rendón, J. G. Santiesteban, *catalytic growth of carbon microtubules with fullerene structure*, Appl. Phys. Lett., **62**, 657 (1993).
59. V. Ivanov, J. B. Nagy, P. Lambin, A. Lucas, X.B. Zhang, X. F. Zhang, D. Bernaerts, G. V. Tendeloo, S. Amelinckx, J.V Landuyt, *The study of carbon nanotubes produced by catalytic method*, Chem. Phys. Lett., **223** (4), 329 (1994).
60. K. Hernadi, A. Fonseca, J. B. Nagy, J. Riga, A. Lucas and D. Bernaerts, *Catalytic synthesis and purification of carbon nanotubes*, Syn. Met., **77**, 31 (1996).
61. A. Fonseca, K. Hernadi, P. Piedigrosso, J. F. Colomer, K. Mukhopadhyay, R. Doome, S. Lazarescu, L.P. Biro, P. Lambin, P. A. Thiry, D. Bernaerts, J. B. Nagy, *Synthesis of single- and multi-wall carbon nanotubes over supported catalysts* Appl. Phys. A **67** (1), 11 (1998).
62. J. Kong, A. M. Cassell, Honhjie Dai, *Chemical vapor deposition of methane for single-walled carbon nanotubes*, Chem. Phys. Lett., **292**, 567 (1998).
63. K. Hernadi, A. Fonseca, P. Piedigrosso, M. Delvaux, J. B. Nagy, D. Bernaerts, J. Riga, *Carbon nanotubes production over Co/silica catalysts*, Catal. Lett., **48**, 229 (1997).
64. K. Hernadi, A. Fonseca, J. B. Nagy, D. Bernaerts, A. Fudala, A. A. Lucas, *Catalytic synthesis of carbon nanotubes using zeolite support*, Zeolites **17**, 416 (1996).
65. Q. Li. H. Yan, Y. Cheng, J. Zhang, Z. F. Liu, *A scalable CVD synthesis of high-purity single-walled carbon nanotubes with porous MgO as support material*, J. Mater. Chem. **12**, 1179, (2002).
66. C. Laurent, A. Peigney, A. Rousset, *Synthesis of carbon nanotube-Fe-Al<sub>2</sub>O<sub>3</sub> nanocomposite powders by selective reduction of different Al<sub>1.8</sub>Fe<sub>0.2</sub>O<sub>3</sub> solid solutions*, J. Mater. Chem., **8**, 1263 (1998)
67. K. Hernadi, A. Siska, L. Thiên-Nga, L. Forró, I. Kiricsi, *Reactivity of different kinds of carbon during oxidative purification of catalytically prepared carbon nanotubes*, Solid State Ion., **141**, 203 (2001).
68. J. W. Seo, E. Couteau, P. Umek, K. Hernadi, P. Marcoux, B. Lukic, Cs Mikó, M. Milas, R. Gaál, L. Forró, *Synthesis and manipulation of carbon nanotubes*, New Journal of Physics, **5**, 120.1-120.22 (2003).
69. W E Wong, P. E Shehan, C. M Lieber, *Nanobeam Mechanics: Elasticity, Strength, and*

- Toughness of Nanorods and Nanotubes*, Science, **277**, 1971(1997).
70. J. P. Salvetat, G. A. D. Briggs, J. M. Bonard, R. R. Basca, A. J. Kulik, T. Stöckli, N. A. Burnham, L. Forró, *Elastic and shear moduli of single-walled carbon nanotube ropes* Phys. Rev. Lett., **82**, 944 (1999).
  71. C. Pirlot, I. Willems, A. Fonseca, J. B. Nagy, J. Delhalle, *Preparation and Characterization of Carbon Nanotube/Polyacrylonitrile Composites*, Adv. Eng. Mater., **4**, 109 (2002).
  72. J. H. Fan, M. X. Wan, D. B. Zhu, B. H. Chang, Z. W. Pan, S. S. Xie, *Synthesis and properties of carbon nanotube-polypyrrole composites*, Synth. Met., **102**, 1266 (1999).
  73. X.Y. Gong, J. Lui, S. Baskaran, R. D. Voise, J. S. Young, *Surfactant-Assisted Processing of Carbon Nanotube/Polymer Composites*, Chem. Mater., **12**, 1049 (2000).
  74. L. S. Schadler, S. C. Giannaris, P. M. Ajayan, *Load transfer in carbon nanotube epoxy composites*, Appl. Phys. Lett., **73**, 3842 (1998).
  75. X. Chen, J. Xia, J. Peng, W. Li, S. Xie, *Carbon-nanotube metal-matrix composites prepared by electroless plating*, Composites Science and Technology, **60** (2), 301(2000)
  76. CL. Xu, BQ. Wei, RZ. Ma, J. Liang, XK. Ma, DH. Wu, *Fabrication of aluminium-carbon nanotube composites and their electrical properties*, Carbon, **37** (5), 855(1999)
  77. B. Valter, M.K.Ram, C. Nicolini, *Synthesis of Multiwalled Carbon Nanotubes and Poly(o-anisidine) Nanocomposite Material: Fabrication and Characterization of Its Langmuir-Schaefer Films*, Langmuir, **18**, 1535 (2002).
  78. J. Sun, L. Gao, W. Li, *Colloidal Processing of Carbon Nanotube/Alumina Composites*, Chem. Mater., **14**, 5169 (2002).
  79. R. Andrews, D. Jacques, D. Qian, T. Rantell, *Multiwall Carbon Nanotubes: Synthesis and Application*, Acc. Chem. Res. **35**, 1008 (2002).
  80. S. Cui, R. Canet, A. Derre, M. Couzi, P. Delhaes, *Characterization of multiwall carbon nanotubes and influence of surfactant in the nanocomposite processing*, Carbon, **41**, 797 (2003).
  81. K. Hernadi, E. Couteau, J. W. Seo, L. Forró, *Al(OH)<sub>3</sub>/Multiwalled Carbon Nanotube Composite: Homogeneous Coverage of Al(OH)<sub>3</sub> on Carbon Nanotube Surfaces*, Langmuir, **19**, 7026 (2003).
  82. K. Hernadi, E. Ljubovic, J. W. Seo and L. Forró, *Synthesis of MWNT-based composite materials with inorganic coating*, Acta. Mater., **51**, 1447 (2003).
  83. G. Dawson, *Powder Metallurgy: the process and its products*, EPMA European Powder Metallurgy Association, (1998).

84. E. Carreño-Morelli, T. Cutard, R. Schaller, C. Bonjour, *Processing and characterization of aluminium-based MMCs produced by gas pressure infiltration*, *Materials Science and Engineering*, **A251**, 48 (1998).
85. Ludwig Reimer: *Sacnning Electron Microscopy, Physics of Image Formation and Microanalysis* (Springer-Verlag, Berlin Heidelberg New York Tokyo) (1985).
86. A. S. Norwick, B. S. Berry, *Anelastic relaxation in Crystalline Solids*, Academic Press, New York and London, (1972).
87. G. Fantozzi, *Phenomenology and definitions*, in *Mechanical spectroscopy Q<sup>-1</sup> 2001 with applications to materials science*, edited by R. Schaller, G. Fantozzi, and G. Gremaud (2001).
88. A.Lakki, Ph.D. thesis, EPFL-Lausanne, (1994).
89. A.Lakki, R. Shaller, C. Carry, and W. Beroit, *High temperature anelastic and viscoplastic deformation of fine-grained MgO-doped Al<sub>2</sub>O<sub>3</sub>*, *Acta mater.* **46**, 689 (1998).
90. J. San. Juan, *Mechanical spectroscopy*, in *Mechanical Spectroscopy Q<sup>-1</sup> 2001*, edited by R. Schaller, G. Fantozzi, and Gremaud, 141-157 (2001).
91. A. V. Granato, K. Lücke, *J. Appl. Phys.* **27**, 789 (1956).
92. W. Benoit, *Dislocation: description and dynamics*, in *Mechanical Spectroscopy Q<sup>-1</sup> 2001*, edited by R. Schaller, G. Fantozzi, and Gremaud, 141-157 (2001).
93. R. Schaller, *Precipitation*, in *Mechanical Spectroscopy Q<sup>-1</sup> 2001 with applications to materials science*, edited by R. Schaller, G. Fantozzi, and Gremaud, 437-450 (2001).
94. J. S. Koehler, *Imperfections in Nearly Perfect Crystals*, (W. Shockley, et al. eds.), *Chapter 7. Wiley, New York (1952)*.
95. G. Gremaud, *Dislocation – point defect interaction*, in *Mechanical Spectroscopy Q<sup>-1</sup> 2001*, edited by R. Schaller, G. Fantozzi, and Gremaud, 178-246 (2001).
96. C. Mayencourt, R. Schaller, *A theoretical approach to the thermal transient mechanical loss in Mg matrix composites*, *Acta mater.* **46**, 17, 6103 (1998).
97. E. Carreño-Morelli, S. E. Urreta, R.Schaller, *Mechanical Spectroscopy of Thermal Stress Relaxation in Aluminium Alloys Reinforced with Short Alumina Fibres*, *Phys. Stat. Sol. (a)* **167**, 61 (1998).
98. C. Mayencourt, R. Schaller, *A high-damping magnesium matrix to limit fatigue in composites*, *Journal of Reinforced Plastics and Composites*, **18**. 18 (1999).



# Acknowledgements

A large number of individuals have contributed to this work. I would like to express my sincere gratitude to all of them.

I would like to particularly and gratefully acknowledge Dr. Robert Schaller for guiding this thesis. His inexhaustible enthusiasm for new ideas helped me to broaden my thinking. He was always available for efficient discussions. I appreciated very much his precise and very competent advice, which he gave me during these years.

It is my great pleasure to acknowledge prof. Willy Benoit for providing me this opportunity to work in his group, the Laboratoire de Génie Atomique which became Institut de Physique de la Matière Complexe, as well as for his ever-optimistic support and encouragement of this work.

I wish to express my special gratitude to prof. Laszló Forró for his constructive remarks through the whole thesis. He was always concerned the progress of this work and advised me professionally. I am very thankful of his advice.

I would like to thank the collaboration with Haute Ecole Valaisanne, Sion, Switzerland. I gratefully acknowledge prof. E. Carreño-Morelli for his contribution to this work, his generous help and the fruitful discussions.

I would also like to thank Dr. Edina Couteau for synthesizing carbon nanotubes.

I am pleased to owe my very special thanks to Dr. Nadine Baluc and Dr. Daniele Mari, who have inspired me with their tireless dedication to my study of material science.

I am indebted to Bernard Guisolan who has performed a lot of work in preparing infiltrated specimens. I would also like to thank Gérald Beney and Antonio

Gentile for sample cutting. I am grateful to Alessandro Ichino for keeping the electronics always working.

I also wish to recognize the Centre Interdépartemental de Microscopie Electronique at EPFL for providing the microscopy facilities. I especially acknowledge Committee of Technology and Innovation of Switzerland for the financial support.

I am grateful to numerous current and former colleagues for their precious friendship and help. I really enjoyed working with them.

Finally, I especially acknowledge the patience and support of my family, who has been the silent partner in this effort.

# Curriculum Vitae

## JIAN YANG

*Born in Guangxi, P. R. China*

### Education

2000 - 2004     Ph.D student at Institut de Physique de la Matière Complexe,  
Ecole Polytechnique Fédérale de Lausanne (EPFL), Switzerland

1987 - 1991     Bachelor of Science at physics department,  
Guangxi Normal University, China

### Work experience

1992 - 1997     Lecturer  
Yulin Teacher College, Guangxi, China





# Publications

1. E. Carreño-Morelli, **J. Yang**, R. Schaller, C. Bonjour, *Carbon nanotube reinforced metal matrix composites, Proc. Of EURO PM2003, European Conference on Powder Metallurgy, Valencia, Spain, October 20-22, 2003.*
2. **J. Yang** and R. Schaller, *Mechanical Spectroscopy of Mg Reinforced With Al<sub>2</sub>O<sub>3</sub> Short Fibres and C Nanotubes*, Materials Science and Engineering A, Vol. 370, issues 1-2, (2004).
3. E. Carreño-Morelli, **J. Yang**, E. Couteau, K. Hernadi, J. W. Seo, C. Bonjour, L. Forró, R. Schaller, *Carbon nanotube / magnesium composites*, Physica Status Solidi (a), vol. 201, issue 8, pp. R53, (2004).
4. E. Carreño-Morelli, **J. Yang**, E. Couteau, K. Hernadi, J. W. Seo, C. Bonjour, L. Forró, R. Schaller, *Tiny tubes boost for metal matrix composites*, Metal Powder Report, Vol. 59, issue 7, pp.40, (2004), reprinted from Proc. of EURO PM2003 and Physica Status Solidi (a).